National University of Singapore

Department of Physics

Thesis submitted in partial fulfillment of the requirements

for the degree of

Bachelor of Science (Honours)

2D Optical Trapping Potential for the Confinement of Heteronuclear Molecules

Author: Raymond Santoso

Supervisor: Associate Professor Kai Dieckmann

2013/2014

Abstract

Ground state alkali-metal dimers provide interesting experimental systems to study as the polarity of the molecule allows the presence of the long-range and anisotropic dipole-dipole interaction between the molecules. Such ultracold molecules have been produced and trapped within an optical trap formed by a high power laser beam. The trapping of these molecules however, is predicted to be severely limited by a chemical reaction loss induced by inelastic collisions between molecules. Such a loss could be reduced by a special trap geometry formed by a beam shaped into a periodic two-dimensional flat-top intensity pattern.

Several schemes are studied in this work to realize a flat-top intensity beam from the Gaussian beam intensity of a commercial laser. Taking into account the available spatial light modulators (SLM) devices which can be used to shape the beam, we review three beam shaping schemes and we perform numerical simulations for each scheme in order to determine their feasibility for an experimental realization of the optical trap.

Finally, we present our early experimental results where we adapt one of the simulated schemes experimentally. We present the characterizations of the laser system, the SLM device and a first production of a shaped flat-top beam in our lab.

Contents

Chapter 1

Introduction

1.1 Ultracold Molecules in an Optical Trap

The field of ultracold atoms and molecules has developed rapidly over the last two decades. In late 1990s, Bose-Einstein Condensation of alkali bosons [1] [2] and degenerate fermionic potassium atoms [3] have been achieved by trapping and cooling of a dilute gas of atoms. The system of a trapped ultracold gas is very popular due to the possibility of controlling various physical parameters of the system such as the temperature, dimensionality, potential landscape, and interactions between the particles. For these reasons, ultracold quantum gases have been used as a simulator to various other quantum systems, notably in condensed matter physics, where the control over the system is not as clean [4].

In this study, we are interested in ultracold alkali-metal dimer molecule systems, which is a molecule formed from two different-species alkali atoms. Such molecule is a polar molecule with a permanent dipole moment in its ground state. This system is interesting because of the presence of the long range dipole-dipole interaction, whose interaction energy decays as $1/r^3$ instead of $1/r^6$ decay of the van-der-Waals interaction in neutral atoms. Such a long-range interaction is useful in the study of interacting many-body systems, for example in a lattice configuration where the molecules are placed in periodically-spaced position mimicking a crystal. Here, the long-range and anisotropic dipole-dipole interaction could be implemented to aid the exploration of various quantum phases [5] or to set up a spin-like interaction which models the quantum magnetism [6]. In addition, the cold molecules can also be used to study chemical reactions at low temperatures where the interactions and the states of the molecules play a big role in a rich dynamics of the system [7] [8].
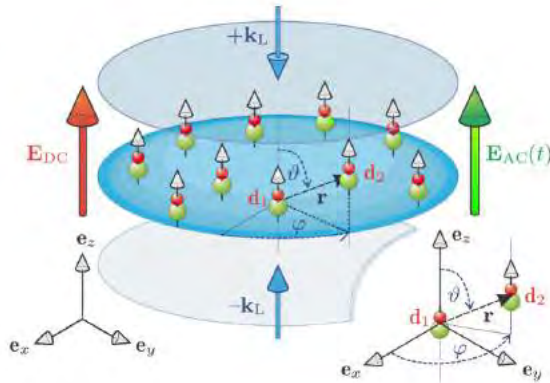

Figure 1.1: A lattice configuration where the polar molecules sit in a periodic arrangement and interact with a dipole-dipole interaction. Adapted from [5]

The choice of an alkali-metal dimer as our polar molecule is based on the feasibility of trapping and cooling such molecules to ultracold temperature. The strategy used in our experiment in to trap and cool two species of alkali fermions to microKelvin temperature. From the constituent atoms, the diatomic molecules are then formed using a magnetic-field-assisted association technique, known as the Feshbach resonance [9]. The magnetic field couples the state of two colliding cold atoms to a near-zero energy molecular bound state, converting the atoms into a weakly-bound molecular state. From this state, the molecule can be brought into the ground state by a stimulated Raman transition [10] where the permanent dipole moment of the molecules can then be polarized with an external DC electric field. The molecule creation [11] and its coherent transfer to the ground state [12] as described above has been experimentally demonstrated with the $^{40}K^{87}Rb$ molecule. However, the permanent dipole moment of this molecule species is fairly low at 0.61 Debye, according to [13]. In our research group, we are interested in adopting the above experimental procedure with a $^{6}Li^{40}K$ mixture which has a higher dipole moment at 3.56 Debye.

One important aspect in the ultracold gas system is the potential energy landscape. First of all, the induced external potential needs to trap the cold gas. Two prominent type of trap that has been utilized experimentally are the magnetic trap [14] [2] and the optical trap [15]. The optical trap is normally used at the later stage of the experiment due to its ability to trap the atoms regardless of their magnetic state and the ease of modifying the potential landscape. In fact, the optical potential is formed by the interaction between a laser and the cold gas, and the potential can be tuned by adjusting the shape of the trapping beam. Several experiments have explored this aspect, realizing a diversity of physical phenomena with different shapes of potential such as an optical lattice with a crystal-like periodic potential [16] [17], a box potential [18] and a vortex beam which carries angular momentum [19].

In this work, we choose a combination of a periodic lattice structure along one dimension and a uniform potential along the other two as our trap geometry. While the periodic lattice is a relatively well-known setup, the creation of a uniform potential is a lot more involved. To form a uniform potential, the intensity of the laser needs to be converted into a flat-top pattern consisting of a uniform distribution at the center which rapidly decreases to zero at the wing. Such a process is also considered in several industrial applications such as welding and etching of metals or plastics [20]. This application is in fact of great relevance for our case since a main difficulty in both the optical trap and the welding process is to handle a high power laser. This is an important consideration in choosing the beam shaping scheme to make sure that the optical elements involved can tolerate a high power beam.

1.2 Scope of This Report

In this project, we address the task of designing an optical trap to hold the ground state ultracold LiK molecules. We begin in chapter 2 by briefly describing the general working mechanism of an optical trap. We shall see that the main problem in optical trapping of alkali-metal dimers is the high loss rate due to a chemical reaction. Therefore, we discuss how a tight confinement with a lattice structure, combined with a flat-top intensity pattern would help to mitigate this problem while maintaining a strong confinement of the molecules.

In chapter 3 and 4, we address the problem of shaping the beam intensity profile from a Gaussian mode to a flat-top pattern. We begin both chapters by introducing various spatial light modulator (SLM) devices which are necessary to perform the beam shaping, with chapter 3 focusing on the phase-modulation type and chapter 4 on the amplitude-modulation type. We then proceed by introducing the beam shaping scheme with the use of the available SLMs such as the Mixed-Region Amplitude Freedom (MRAF) in chapter 3, the Fourier Transform Holography scheme in chapter 4 and finally the Error Diffusion algorithm in chapter 4. In each scheme,

we discuss their advantages and challenges in relation with their experimental implementation.

Finally, in chapter 5, we describe the experimental tests which have been performed to demonstrate the beam shaping to produce a flat-top beam. We perform several characterizations on both the laser system and the SLM used in this test, in addition to their alignment methods according to the chosen shaping scheme. We conclude the chapter with a discussion on our first observation of the beam shaping attempt, and we summarize several steps which could be carried on to continue this project.

Chapter 2

Optical Dipole Trap Design for LiK Molecules

In this chapter, we present a description of the optical trap that is used to hold the LiK molecules. We start by briefly discussing the physical mechanism of an optical trap, which in our case is formed by a far-red detuned, narrowband laser beam. We follow this description by discussing the dominant loss phenomenon due to the collision-induced chemical reaction that limits the lifetime of the molecules in the trap. Taking into account this loss phenomenon, we close this chapter by presenting the choice of the geometry of our trap that we wish to realize experimentally.

2.1 Optical Potential of a Red-Detuned Light

When a monochromatic light (with field frequency ω) interacts with an atom or a molecule, the electric field induces a dipole moment that oscillates with the same frequency as the field. Consequently, it can be shown that this electric dipole-field interaction adds an additional $-\mathbf{E}\cdot\mathbf{D}$ term in the Hamiltonian of the molecule-light system, with $\mathbf{E}$ and $\mathbf{D}$ being the field and the dipole operator, respectively. This interaction gives rise to two effects: a conservative optical potential U_{dip} due to the component of the dipole in-phase with the field, and a dissipation rate $\hbar\omega\Gamma_{sc}$ from the component of the dipole out of phase with respect to field [21]. Their expressions with respect to the light intensity $I(\mathbf{r})$ are given by [22]:

$$U_{dip}(\mathbf{r}) = -\frac{3\pi c^2}{2\omega_0^3}\left(\frac{\Gamma_{sp}}{\tilde{\delta}}\right)I(\mathbf{r}), \tag{2.1.1}$$

$$\Gamma_{sc}(\mathbf{r}) = \frac{3\pi c^2}{2\hbar\omega_0^3}\left(\frac{\Gamma_{sp}}{\tilde{\delta}}\right)^2 I(\mathbf{r}). \tag{2.1.2}$$

The above equations are obtained using a two-level system approach, where ω_0 denotes the transition frequency between the two levels and

$$\Gamma_{sp} = \frac{e^2\omega_0^2}{6\pi\epsilon_0 m_e c^3} \tag{2.1.3}$$

symbolizes the spontaneous emission rate calculated using the classical Lorenz model. We also note that the factor

$$\tilde{\delta} = \left(\frac{1}{\omega_0 - \omega} + \frac{1}{\omega_0 + \omega}\right)^{-1} \tag{2.1.4}$$

is the detuning factor between the transition and the light frequencies. The optical potential is the effect beneficial to trap the molecules. For a red-detuned light, where the frequency of the light beam is smaller than the transition frequency, the detuning factor is positive and thus the optical potential is negatively proportional to the light intensity. In this case, the molecules

will accumulate near the maximum intensity of the light which is also the minimum of the dipole-field interaction energy. In addition, we observe that the dissipation rate of the trap due to spontaneous emission, Γ_{sp}, decreases quadratically in function of detuning as compared to linearly for the potential. Hence a far-detuned optical trap is of interest due to the lower loss rate.

The two-level approximation in the above description does not exactly hold true in reality. A molecule possesses a large number of levels (electronic, rotational and vibrational) due to its rich internal structure. Nevertheless, the general conclusion that the optical potential is proportional to the trapping beam intensity typically still holds with the proportionality factor now depending on the state of the trapped molecule [23]. For our diatomic molecule, we can very crudely estimate this proportionality factor by summing the proportionality factors from Li and K atoms. Such estimation would be rather accurate for the Feshbach state where the molecules are recently associated from the two atoms, but would be less so for the molecules who have been brought to the ground rovibrational state.

2.2   Controlling the Reaction Loss in LiK Molecules

Diatomic molecules formed by a mixture of two species of alkali atoms are known to posses an exothermic reaction by exchange of atoms [24]. For LiK molecule the reaction is in the form $LiK + LiK \rightarrow Li_2 + K_2$. This reaction is not desirable because the release of energy causes the molecules to escape the trap, which will be observed as a decrease in the number of trapped molecules over time. In alkali-metal dimers such as our LiK molecule, this reaction loss is actually the dominant loss mechanism of molecules from the optical trap.

The chemical reaction happens via inelastic collisions of molecules, when two of them are brought to a distance where the chemical forces are relevant. A reduction of inelastic collision by a control of the internal states of the molecules has done in fermionic molecule species such as the $^{40}K^{87}Rb$ mixture [7]. This is done by keeping all the molecules in the same state and therefore forces the collision to occur only in the p-wave channel where a centrifugal barrier prevents the molecules to approach each other [25]. Our $^6Li^{40}K$ molecules however, is of bosonic species which collide through the barrierless s-wave channel.
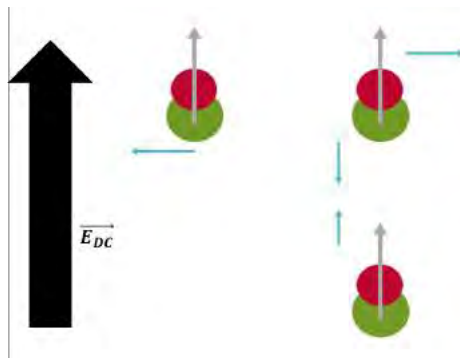

Figure 2.1: The dipole-dipole interaction of polarized ground state LiK molecules. The interaction is repulsive in the plane perpendicular to the static electric field, and attractive on the axis of the field.

An alternative approach to suppress the chemical loss is to take advantage of the polarity of our molecules. The dipole-dipole interaction force between molecules is already prominent at a distance much longer than the chemical force range [24]. By tuning this interaction to be repulsive (i.e. creating a potential barrier) the molecules can be kept at a distance where the chemical force is still insignificant. The interaction force between two dipoles depend both on

the separation vector and the orientations of the dipoles. A particular configuration of interest is where the dipole is polarized to a particular direction, say the Z axis, which can be done by bringing the molecules into the ground state and applying a static electric field along this direction. Following a classical electrodynamics treatment [**?**], the interaction potential can be written as:

$$\mathbf{E}_{dip}(\mathbf{r}) = -\frac{d^2}{4\pi\epsilon_0}\left(\frac{3(\mathbf{e}_r \cdot \mathbf{e}_z)\mathbf{e}_r - \mathbf{e}_z}{r^3}\right), \qquad (2.2.1)$$

where d is the dipole moment of the molecules. In this condition, the interaction between two dipoles is attractive when they are oriented 'head to tail' (i.e. stacked parallel to the static field) but they turn to repulsive when the dipoles are oriented side by side on the plane perpendicular to the static field direction (see figure 2.1). Hence, by keeping all the molecules on the 2D plane, the inelastic collision may be prevented by the repulsive dipole-dipole interaction.
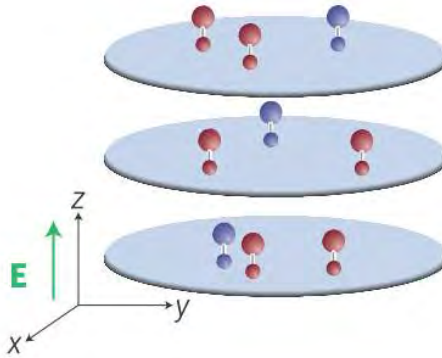

Figure 2.2: Trapped alkali dimer molecules in the optical lattice configuration, with the polarizing static electric field. Figure is taken from [26]

Experimentally, this configuration has been shown for the KRb mixture [26] [27]. The molecules are trapped in an optical lattice configuration, where they are stacked in several pancake-like layer. In one layer, the trapping is very tight along the longitudinal direction while tunneling between different layers are negligible. Thus, the molecules are constrained into a 2-dimensional dynamics where the dipole-dipole interaction is repulsive. As a result, it has been shown that the chemical loss rate in this configuration is significantly better than the loss rate in a 3-dimensional trap.

2.3 The Geometry of the Optical Trap

As discussed in the previous subsections, one of the important consideration for designing the optical trap is to optimize the lifetime of the molecules in trap. First of all, we have discussed the need of confining the molecules in a 2-dimensional geometry instead of a 3-dimensional one. The geometry of the trap is determined by how the molecules are distributed in space, which is dependent on the intensity distribution of the laser used to create the optical trap. To simplify the calculation, we first consider that the molecule cloud is a classical gas which follows a Boltzmann distribution. This assumption is valid when the temperature of the cloud is not too cold (above the condensation temperature for bosonic particles).

Suppose that the laser beam induces an optical potential $U(\mathbf{r})$. According to the Boltzmann distribution and neglecting the interaction energy between the molecules (ideal gas approximation), their density in space is distributed as:

$$n(\mathbf{r}) = n_0\exp(-\beta U(\mathbf{r})), \qquad (2.3.1)$$

where $\beta = 1/(k_B T)$ with the Boltzmann constant k_B and molecule temperature T. Adopting the convention $U(\mathbf{0}) = 0$, the quantity n_0 is equal to the density in the center of the cloud. The central density is calculated by a normalization condition: integrating the density over all space yields the total number of trapped molecules.

Let us now consider the characteristics of the density distribution along the longitudinal (Z) direction for the case of a single-Gaussian beam trap and an optical-lattice configuration. For the first case, the trap is formed by one Gaussian-mode (which is a typical lasing mode of commercial lasers) beam focused at the center of the trap (labeled as $z = 0$). Referring to appendix B, if we assume the beam to have a $1/e^2$ waist of w_0 located at $z = 0$, the beam intensity in cylindrical coordinate can be written as:

$$I_g(r, z) = I_0 \left(1 + \left(\frac{z}{z_R} \right)^2 \right)^{-1} \exp \left(- \frac{2r^2}{w_0^2(1 + (z/z_R)^2)} \right),$$

where $z_R = \pi w_0^2 / \lambda$ is known as the Rayleigh length of the beam and I_0 is the peak intensity of the beam. Near the origin of the coordinate, and along the Z axis, we can develop the intensity in the Taylor series:

$$I_g(0, z) \approx I_0 \left(1 - \left(\frac{z}{z_R} \right)^2 \right). \tag{2.3.3}$$

In the first section, we have established that the optical potential is proportional to the beam intensity. Let us denote the proportionality constant as κ, such that $U(\mathbf{r}) = -\kappa I(\mathbf{r})$. Hence, the optical potential near the origin varies as:

$$U_g(0, z) \approx -U_0 \left(1 - \left(\frac{z}{z_R} \right)^2 \right) = -U_0 + \frac{1}{2} m \omega_z^2 z^2, \tag{2.3.4}$$

where $U_0 = \kappa I_0$. As we can see from equation 2.3.4 above, the optical potential is a harmonic potential near the origin with the characteristic oscillation frequency of

$$\omega_z = \sqrt{\frac{2U_0}{m z_R^2}}, \tag{2.3.5}$$

along the Z direction. Referring back to equation 2.3.1, we obtain a Gaussian density distribution of the molecules near the origin:

$$n(0, z) = n_0 \exp \left(- \frac{m \omega_z^2 z^2}{2 k_B T} \right). \tag{2.3.6}$$

The characteristic length in this density distribution is the $1/e$ width of the Gaussian distribution which we call l_c. In this case, it is related to the trap frequency:

$$l_c = \sqrt{\frac{2 k_B T}{m \omega_z^2}}. \tag{2.3.7}$$

We can compare the situation with the second form of the trap which is the lattice configuration. This configuration is realized by creating an interference pattern between a propagating beam and its retro-reflection off a mirror. Denoting the axis of the propagation of the laser as the Z axis, the intensity pattern along this axis follows a sinusoidal pattern:

$$I_{ol}(0, z) = |\sqrt{I_0} e^{ikz} + \sqrt{I_0} e^{-ikz}|^2 = 4 I_0 \cos(kz)^2, \tag{2.3.8}$$
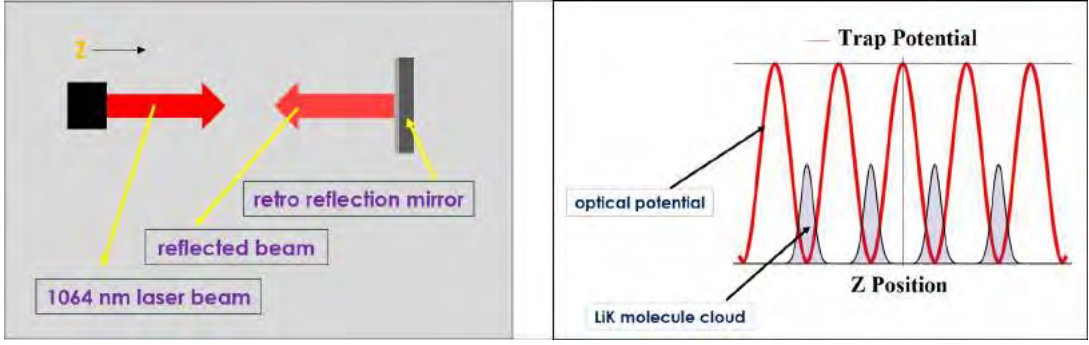
Figure 2.3: (Left) The setup for an optical lattice configuration and (Right) LiK molecules trapped in the periodic potential valleys formed by the interference pattern.

where $k = 2\pi/\lambda$ is the wavenumber. In this configuration, we remark that the intensity varies periodically in function of the longitudinal position. As the laser is red-detuned, the molecules will be trapped around numerous intensity peaks, separated by the distance $\lambda/2 = 532$ nm (refer to figure 2.3). In addition, the peak intensity is enhanced by a factor of 4 due to the constructive interference from the two copies of the beam. Let us concentrate on one particular intensity peak (e.g. at the origin), where again the intensity of the beam can be developed in a Taylor series:

$$I(z) \approx 4I_0(1 - (kz)^2). \tag{2.3.9}$$

Therefore, the potential near each intensity peak is again a harmonic potential:

$$U_{ol}(0, z) \approx -\gamma(4I_0(1 - (kz)^2)) = -4U_0 + \frac{1}{2}m\omega_z z^2, \tag{2.3.10}$$

with a trap frequency of:

$$\omega_z = 2\pi\sqrt{\frac{8U_0}{m\lambda^2}}. \tag{2.3.11}$$

From the description of the two traps, we can compare how the optical lattice configuration produces a much tighter confinement along the Z axis. Firstly, we can compare the width of the gaussian distribution of the molecular cloud which is described by the length l_c. Taking the ratio of l_c for the single beam and the optical lattice, we obtain:

$$\frac{l_{c,g}}{l_{c,ol}} = \frac{\omega_{z,ol}}{\omega_{z,g}} = \frac{2\pi\sqrt{\frac{8U_0}{m\lambda^2}}}{\sqrt{\frac{2U_0}{mz_R^2}}} = 4\pi\frac{z_R}{\lambda} = \frac{4\pi^2 w_0^2}{\lambda^2}. \tag{2.3.12}$$

The typical waist size of the beam used in an optical trap is of the order of 100 μm. Compared to the wavelength which is of the order of 1 μm, the width of the cloud in a single beam setup is therefore up to 5 order of magnitudes greater than in the lattice setup. We conclude that the molecular cloud layers are extermely flat along the Z direction in the lattice setup, and therefore the 'pancake layers' picture is often used to describe the trapped molecules in this configuration. Furthermore, we can assert that the dynamics of the cloud along the longitudinal direction is inactive due to this tight confinement. Treating the optical potential as a simple quantum harmonic oscillator, we remark that the energy separation between the ground state and the excited state is of the order of $\hbar\omega_z$. If the thermal energy is largely inferior to this energy gap, the thermal fluctuation will not be able to lift the states of the molecules from the ground state thus the dynamics is not activated [24]. To calculate the trap frequency according to equation 2.3.11, we need to estimate U_0. We take an example of a 10 W laser, propagating in a Gaussian mode with a waist of 100 μm. Here, the peak intensity is given by $I_0 = 2P/(\pi w_0^2) \approx 6 \cdot 10^8$

9

W/m^2. The κ factor is estimated using the sum of the κ factors from Li and K atoms, and is approximately equal to $2.7 \cdot 10^{-36}$ J/(W/m^2). With these assumptions, the trap frequency is $2\pi \cdot 400$ kHz. With the cloud temperature of 500 nK which is typically achieved in experiment, the energy level separation is of the order of 40 times the thermal energy, justifying our assumption of 2-dimensional dynamics.
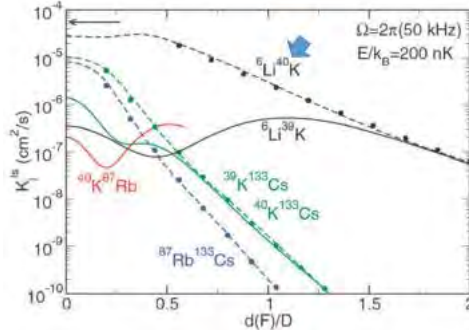

Figure 2.4: Chemical reaction loss rate of several alkali dimers in the optical lattice trap, in function of the induced electric dipole moment [24].

Due to the longer lifetime in an optical trap setting, a lot of theoretical efforts have been dedicated to calculate the chemical reaction loss rate in this trap. In figure 2.4, we show a theoretical calculation from reference [24] which calculates the chemical reaction loss coefficient of the trapped LiK molecules in the 2D dynamics of the optical lattice. The loss rate due to the reaction is the product of this coefficient and the 2D density of the trapped molecule cloud. For the calculation of this density factor, we need to describe the transverse pattern of the beam intensity. First of all, let us consider a conventional Gaussian beam pattern, with a 100 μm waist. The Taylor expansion of the intensity distribution near one intensity peak (chosen to be the origin), in function of the transverse coordinate r is given by (c.f. equation ??):

$$I(r,0) \approx 4I_0 \left(1 - \frac{2r^2}{w_0^2}\right), \tag{2.3.13}$$

where the factor of 4 is inserted to take into account the constructive interference effect. Proceeding with the similar calculation method as we have done, the density distribution of one pancake layer is given by:

$$n(r) \approx n_0 \exp\left(-\frac{m\omega_r^2 r^2}{2k_B T}\right), \tag{2.3.14}$$

where the radial frequency is given by:

$$\omega_r = \sqrt{\frac{16U_0}{mw_0^2}}. \tag{2.3.15}$$

In equation 2.3.14, notice that $_0$ is the peak 2-dimensional density where the longitudinal degree of freedom is integrated out. The highest loss occur at the center of the coordinate where the density is at its peak. Normalizing the peak density to the number of molecules N, we find:

$$\int n(r,z)2\pi r dr dz = N \qquad \Rightarrow \qquad n_0 = \frac{2N}{\pi w_0^2}\left(\frac{4U_0}{k_B T}\right). \tag{2.3.16}$$

The typical number of molecules found in the central pancake layer is of the order of 2000 molecules [26]. Hence, keeping the other parameters the same as in the previous discussion, the central density of the molecule is $n_0 \approx 2.5 \cdot 10^{10}$ cm^{-2}. Referring back to figure 2.4, the loss coefficient can be brought as low as 10^{-7} cm^2/s provided that the static electric field is

strong enough to induce the dipole moment of around 2 Debye. Even then, the loss rate will still be at $2.5 \cdot 10^3$ s^{-1}, implying a 0.4 ms molecule lifetime in the trap. The typical value needed to complete all the experimental sequences are usually on the order of one to several seconds. Thus, we need to increase the lifetime to the order of seconds.

The way to increase the lifetime in this case is to reduce the 2D density of the molecule. One way to achieve this is to enlarge the waist of the trap beam. With a larger beam, the beam intensity is reduced as it is distributed over a larger area. However, in doing this, we also weaken the trap depth which is proportional to the beam intensity, inducing a loss by thermal excitation. Looking at equation 2.3.16, the peak density has an extra $1/w_0^2$ dependence on top of a proportionality to the trap depth $4U_0$. Therefore, in principle we can reduce the peak density and keeping the same trap depth with a large beam waist. However, to keep a constant intensity, we need to supply an increasingly higher beam power that is not available experimentally.

Instead, we propose to alter the transverse intensity distribution of the beam to a uniform (flat-top) distribution. The trapping potential with this beam shape will have a shape of a square-well potential, with the width given by the beam size and the depth given by the beam intensity. According to equation 2.3.1, a uniform trapping potential also implies a uniform molecule density distribution, which gives the lowest peak density for a fixed number of molecules. If instead of a Gaussian beam of 100 μm waist, a 100 μm radius flat-top beam is set as the trap beam, the 2000 molecules are distributed over a circle of 100 μm radius. Hence the peak molecule cloud density is $n_0 = 6.4 \cdot 10^6$ cm^{-2}, which is three order of magnitudes lower than in the Gaussian trap and will give a lifetime of the order of 1 second. Moreover, the density is now independent of the trap depth. With a 10 W power, 100 μm radius flat-top beam, the trap depth is $4U_0 \approx k_B \cdot 250\mu$K, which is a lot higher compared to the thermal energy.

In conclusion, we have presented the design of our optical trap in this chapter. The two main characteristics of the trap we are mostly interested in are the chemical reaction loss rate and the trap depth. Our geometry of choice is the combination of a quasi 2-dimensional molecule cloud through an optical lattice configuration and a uniform transverse beam intensity distribution. The combination of these two ingredients are shown to produce a deep trap with a lifetime of the order of one second.

Chapter 3

Beam Shaping with a Phase-Modulation SLM

This chapter is dedicated to a discussion on how to transform the intensity pattern of a laser, from the input Gaussian pattern, using a phase-modulation Spatial Light Modulator (SLM). We start the discussion with a description of commercially available phase-modulation SLMs. Afterward, we describe a beam shaping method in the form of an iterative algorithm which is compatible with the use of a phase-modulation SLM. Finally, we discuss our analysis of such scheme in view of its implementation for our optical trap.

3.1 Examples of Commercially Available Phase-Modulation SLM

In this manuscript, we narrow down our scope to focus on two classes of SLM devices. One class is the devices which are capable of producing a phase-only modulation of the input beam, while the other is a type which does a binary amplitude modulation. Even under the category of phase-modulation SLM, there are many different types of devices, each offering an advantage in specific quality such as the pixel size, the active area size, the response time, the dynamic range and the resolution of the modulation, the damage threshold, etc. [28]. In this section, we present a brief overview of some popular selections of the phase-only modulation devices, focusing on their modulation mechanism and typical parameters pertinent to our beam shaping scheme.

Liquid Crystal on Silicon SLM

The most popular phase-modulation type SLM device is the Liquid Crystal on Silicon (LCoS) SLM. This type of SLM consists of a nematic liquid crystal (LC) medium, which is sandwiched between a transparent electrode attached to the entry window and a dielectric mirror layer covering a CMOS backplane (see figure 3.1). The backplane consists of pixelated electrodes which are controllable individually. A change in the applied voltage on the electrode rotates the orientation of the LC molecules which modifies the refractive index of the medium.

In this kind of device, the input light enters the LC medium and is reflected out . A light beam propagating through a medium of length l with an index of refraction n acquires a phase shift of $\exp\left(2\pi i n l/\lambda\right)$. Therefore, LCoS SLMs can give a position-dependent phase shift by specifying the voltage in each pixel. By the calibration of the applied voltage and an appropriate design of the thickness of the liquid crystal layer, the SLM is usually designed to provide a phase shift from 0 to 2π, with a usual resolution of 256 levels. The active area of these SLM usually contains 1000 to 2000 pixels, with the interpixel distance (also called the
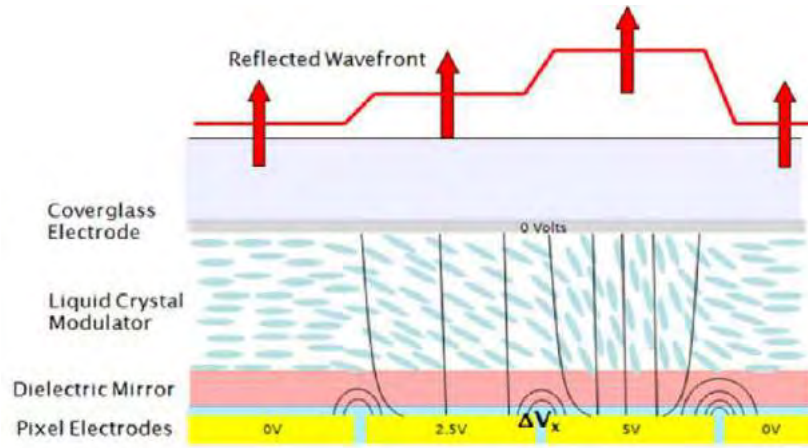
Figure 3.1: Schematic of a typical LCoS type SLM. Figure is taken from [29]

pixel pitch) of the order of 10 μm. The reflectivity from these devices are typically above 80%, limited by the losses from the medium and the presence of gaps between the pixels.

Piston-Type MEMS

This type of SLM falls under the category of a microelectromechanical systems (MEMS). It consists of an array of micrometer-sized mirrors, each controlled by an electrostatic actuator which displaces each mirror in the vertical direction. The reflected beam from this mirror array acquires a relative phase factor due to the optical path difference depending on the height of the mirror pixel at each position of the beam (refer to figure 3.2).
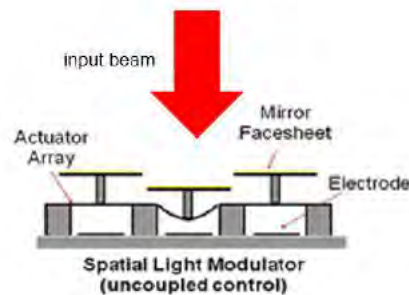

Figure 3.2: Schematic of the piston-type MEMS SLM. Taken and edited from [30]

The main advantage of this type of device is the higher fill factor (smaller interpixel gap) and possibly a high damage threshold while maintaining a dynamic modulation capability (as opposed to a static modulation pattern from a phase plate). The device offers a comparable dynamic range, capable of 1.5 μm vertical displacement (more than 2π phase modulation for 1064 nm beam) with a higher modulation resolution of up to 14 bits [30]. One of the weakness of this device is the slower response time due to the mechanical movement involved which does not pose a problem for our application because we wish to form a static pattern. However, these devices feature a very small number of pixels and is relatively very costly compared to the LCoS SLM.

14

Static Phase-Modulation Plate

Owing to microfabrication technique, it is possible to create a chrome (reflective) or glass (transmittive) plate providing a phase modulation to the input beam. Similar to the piston-type MEMS, the phase modulation is provided by a optical path difference from holes created by the etching process of the mask. The main advantage of the static plate is the very high damage threshold, reflectivity, and the possibility of having more pixels with larger active area. However, there are two weaknesses of this mask system compared to the SLM. First of all, the discretization level of the phase modulation is usually very limited. Some applications reported the use of a phase mask with only binary level ([31]) or four levels ([20]). Secondly, the static plate option loses in terms of versatility to the dynamic SLM option. The beam shaping methods are usually sensitive on the input beam profile, thus, the static plate is not very reliable in situations where the input profile is modified or fluctuates.

3.2 Beam Shaping with the Iterative Fourier Transform Algorithm

The modulation over the phase degree of freedom essentially affects the spreading of the beam in its propagation after being reflected by the SLM. Based on the interference from different parts of the beam, the intensity profiles after various distances of propagation will vary. Nevertheless, it is not directly evident how a certain target intensity pattern can be achieved with this modulation at some point after the SLM. The main idea of this algorithm is to make use of the Fourier Transform relation that is found when the modulated beam is focused by a positive focal-length lens. With this special arrangement, the problem is simplified as the output profile of the beam can be calculated exactly but we shall see that a phase-modulation alone is not enough to attain an exact beam shaping. As such, this algorithm takes advantage of the inverse Fourier Transform relation to iteratively find the best phase-modulation at the SLM based on the current output profile.

Optical Setup and Algorithm Description

To start the discussion, we consider the optical setup which is depicted in figure 3.3. The SLM is placed at a distance equal to the focal length f of a lens away in front of the lens, defined as the input plane. The plane where the molecules will be trapped by the output beam is located at the back focal plane of the lens. We call this plane the Fourier plane since by this arrangement, the electric field at this plane is given by the exact Fourier Transform (FT) of the electric field at the input plane: ([32], refer to appendix A)

$$E_{FP}(x,y) = \frac{1}{i\lambda f} \int_{-\infty}^{\infty} \int_{-\infty}^{\infty} E_{IP}(X,Y) e^{-2\pi i \frac{xX}{\lambda f}} e^{-2\pi i \frac{yY}{\lambda f}} dXdY. \tag{3.2.1}$$

We set a Gaussian beam with its waist located at the input plane as the beam pattern before it is modulated by the SLM. The electric field of this beam is given by a Gaussian intensity distribution and a flat phase:

$$E_{gauss}(x,y) = \sqrt{\frac{2P}{\pi w^2}} \exp\left(-\frac{x^2+y^2}{w^2}\right), \tag{3.2.2}$$

where P denotes the power of the beam and w its waist (which is assumed to be symmetric in both vertical and horizontal directions). For a beam modulated by an LCoS SLM, our modulation capability is limited to the phase of the beam. Therefore, the modulated field at the input plane E_{IP} has a restricted shape where the amplitude is given by the initial gaussian distribution of the laser and the phase modulation of the SLM:

$$E_{IP}(x,y) = E_{gauss}(x,y) \exp\left(i\Phi_{SLM}(x,y)\right). \tag{3.2.3}$$

For our purpose, we want the Fourier plane beam intensity I_{FP} to have a flat-top distribution. In principle, this can be exactly achieved only if the input plane intensity E_{IP} is the inverse Fourier Transform of a flat-top beam. However, this situation is clearly impossible in our case since the SLM lacks the ability to modulate the amplitude of the input beam.
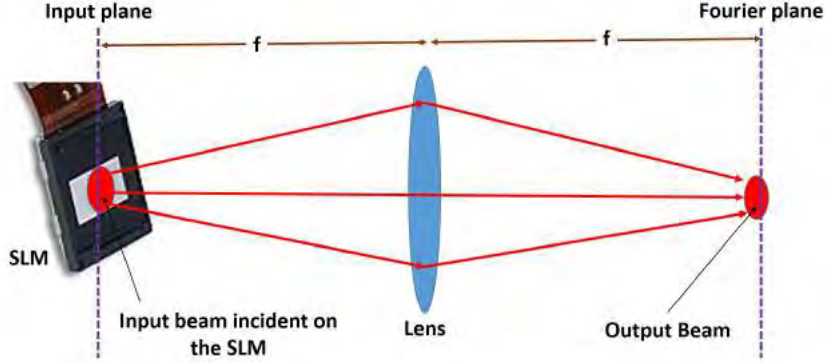

Figure 3.3: The schematic of the optical setup used in the Fourier Transform-based beam shaping algorithm.

It is interesting, however, to find out if it is still possible to produce a beam with a flat-top (or more generally, any arbitrary) intensity pattern in the Fourier plane with only a phase-modulation SLM. To tackle this problem, several solutions have been proposed which are based on finding the best approximate phase-modulation by a form of iterative Fourier Transform algorithm (IFTA). For any guess phase modulation given by the SLM, the field at the Fourier plane E_{FP} can be computed via equation 3.2.1. The concept behind the IFTA is to improve the initial modulation guess by comparing E_{FP} with the desired pattern, and perform sucessive Fourier Transforms with updated guess pattern in each step. In this report, we present a particular algorithm of this class which is called the Mixed Region Amplitude Freedom (MRAF) algorithm [33].

The first step of this algorithm is to produce the initial guess for the SLM phase modulation $\Phi_{SLM}^{(0)}(x, y)$. This quantity is set to be the argument of the phase part of the inverse Fourier Transform of the flat-top beam $E_{flat} = \sqrt{I_{flat}}$:

$$\Phi_{SLM}^{(0)} = \arg(\mathcal{F}^{-1}(E_{flat})). \tag{3.2.4}$$

With this choice of initial phase, we recover the flat-top profile at the Fourier Plane exactly if the amplitude profile of the input beam matches the amplitude profile of the inverse FT of the flat-top beam. However, for our case, the amplitude profile of the input beam is always given by E_{gauss}. Therefore, our initial beam profile at the input plane is given by $E_{IP}^{(0)} = E_{gauss} \exp(i\Phi_{SLM}^{(0)})$.

According to equation 3.2.1, the initial input beam $E_{IP}^{(0)}$ will produce the diffraction pattern $E_{FP}^{(0)} = \mathcal{F}(E_{IP}^{(0)})$ at the Fourier plane. Since this algorithm is recursive, consider the case where we have arrived at the n$^{\text{th}}$ iteration, with the field $E_{FP}^{(n)}$. To produce the next phase modulation guess, we divide the Fourier plane into two areas. We define an area of a certain size from the center of the Fourier plane which we call the signal region (SR), and we define the region outside this area as the noise region (NR). Furthermore, we define a new electric field called the mixed field as the following:

$$E_{mix}^{(n)} = \left\{ m|E_{flat}|_{SR} + (1-m)|E_{FP}^{(n)}|_{NR} \right\} e^{i \arg(E_{FP}^{(n)})}, \tag{3.2.5}$$

16

where m is a constant called the mixing parameter, which regulates the relative power distribution between the two terms in the signal and noise region. The distinction between the two degrees of freedom (amplitude and phase) in the Fourier plane is the particularity of the MRAF algorithm. The decrease in terms of pattern restriction from both amplitude and phase throughout the Fourier plane to only the amplitude pattern in the signal region of the Fourier plane improves the chance of finding an appropriate SLM phase modulation. In addition, the insertion of the target amplitude pattern in the mixed field is the key step to bring the diffracted field intensity closer to the desired pattern in each iteration. The phase guess in the next iteration step is defined as the phase component of the inverse FT of the mixed field:

$$\Phi_{SLM}^{(n+1)} = \arg(\mathcal{F}^{-1}(E_{mix}^{(n)})), \tag{3.2.6}$$

which completes the iteration procedure of the algorithm.

We adopt two quantities as a measure of the quality of the output beam in each step of the iteration. First of all, the output intensity produced at the nth step, $I_{FP}^{(n)} = |E_{FP}^{(n)}|^2$, is fitted against a flat top intensity pattern with three fit parameters: the peak intensity, the center position, and the width of this flat-top profile. Note that the fitting is restricted inside the signal region and let the fitted intensity at this n^{th} step be $I_{fit}^{(n)}$. The diffraction efficiency $\xi^{(n)}$ is calculated by taking the ratio of the power between the output and input beam:

$$\xi^{(n)} = \frac{\sum I_{fit}^{(n)}}{\sum |E_{IP}|^2}. \tag{3.2.7}$$

Furthermore, we define the fractional error $\eta^{(n)}$ of the ouput beam as the averaged root mean square difference between the actual and fitted output beam profile, normalized by the amplitude of the fitted flat-top profile:

$$\eta^{(n)} = \frac{1}{N_{SR}} \sqrt{\sum_{SR} \left(\frac{I_{FP}^{(n)} - I_{fit}^{(n)}}{I_{fit}^{(n)}} \right)^2}. \tag{3.2.8}$$

Here, N_{SR} denotes the number of summation points i.e. the number of pixels contained in the signal region. In principle, the algorithm will continue to improve the output beam profile as long as the fractional error decreases with each step of the iteration. Thus, we can use this criterion as a condition to stop the algorithm. The summary of the complete algorithm is shown in the flowchart in figure 3.4.

Numerical Simulation Test of the IFTA Algorithm

Simulation Methods and Parameters

To test the effectiveness of this algorithm for our application, we conduct a numerical simulation. We choose the relevant parameters to follow the experimental condition as closely as possible. First of all, we model the SLM as a 1024x1024 pixel grid with an interpixel distance of 8 μm. These parameters are found, for example, in the PLUTO SLM from Holoeye [34]. We model our input beam as an ideal collimated Gaussian beam, with its waist located at the SLM. We have the liberty to choose the size of the beam waist since it can be adjusted by placing a lens before the SLM. With a bigger beam waist, we can reduce the peak intensity of the beam incident at the SLM, which is important since we are working with a high power beam. Therefore, we choose the input beam waist to be 3 mm in this simulation.

Our next step is to define the flat-top pattern at the Fourier plane. In general, there are several functions which can be used to describe a flat-topped beam, ranging from the super-Gaussian, flattened-Gaussian, the window/tapering function, and the super-Lorentzian pattern
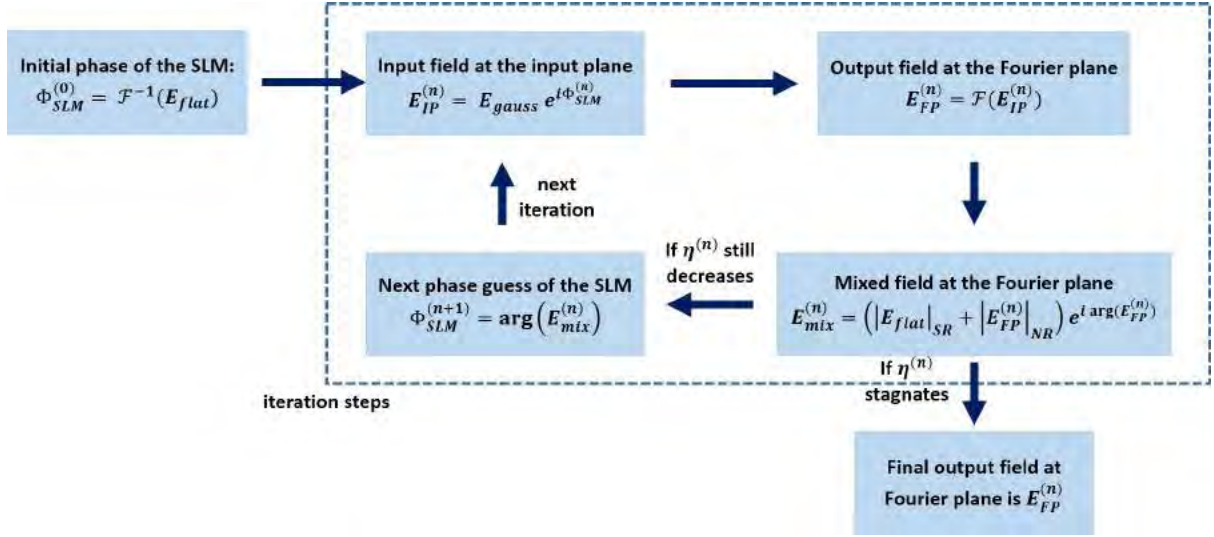
Figure 3.4: Flowchart diagram illustrating the IFTA Algorithm.

[35] [36]. In all these functions, the essential feature that gives the flat-top profile is the higher leading power in the Taylor development of the functions near their central maximum. For a Gaussian profile e^{-x^2}, the leading power is quadratic. For our simulation, we choose to describe the flat-top as a super-Lorentzian (SL) function:

$$ SL_n(r) = A \left[1 + \left| \frac{r}{w_{SL}} \right|^n \right]^{-1} . \tag{3.2.9} $$

With this choice, the radius of the flat-top beam is given by w_{SL} while the leading power in the expansion is now given by the integer n. The profile of higher order SL function falls more sharply in the wing, as we can see in figure 3.5 below. Finally, the current experimental setup uses a 300 mm lens to focus the trapping beam in the experiment chamber. Thus, we adopt the same value for our simulation.
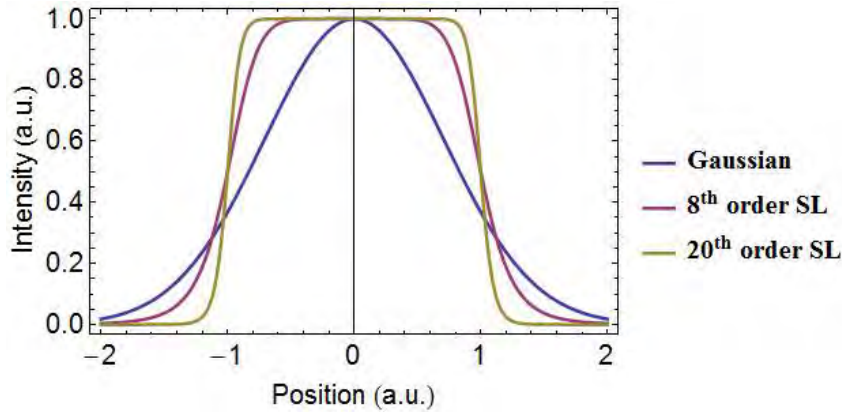
Figure 3.5: Comparison between the Gaussian and higher order Super-Lorentz functions.

This simulation is performed in Mathematica. The only nontrivial computation step is to model the Fourier Transform between the input plane and the Fourier plane. For this, we use a built-in Fast Fourier Transform (FFT) method which is essentially a Riemann sum approximation of the Fourier Transform integration. The 1024 by 1024 pixels are chose to optimize the computation speed based on the particularity of the FFT algorithm.

Simulation Results and Discussion

By the Fourier Transform relation, the pixel size at the Fourier plane depends on the size of the pixel at the input plane. If we discretize the input plane with N pixels with the interpixel distance of Δ, the diffraction-limited pixel size at the Fourier plane is given by $\tilde{\Delta} = \frac{\lambda f}{N\Delta}$, where λ is the beam wavelength (1064 nm) and f is the focal length of the lens (300 mm). Therefore, $\tilde{\Delta} \approx 39\mu$m. To have a sufficient amount of pixels, we start with an order 20 Super-Lorentz beam with 400 μm radius as the target pattern. The signal region is defined as a square box of side equals to 1200 μm surrounding the intended flat-top pattern, which is sufficiently large for this target pattern. We take the mixing parameter m in equation 3.2.5 to be constant at 0.4 in each step, as suggested by the original author of this algorithm[33].

We run 200 steps of iterations for this particular choice of beam input and output, and we present the final output intensity in the Fourier plane in figure 3.6. This output profile matches very well with the target flat-top pattern, as can be seen by the comparison with the fitted profile (the solid line in the right hand side of figure 3.6). The fit result is a flat-top pattern with the same radius as the intended target (400 μm), however with a lower maximum amplitude. We can see from the diffraction efficiency plot (figure 3.7) that the power contained in the flat-top beam in the signal region approaches 44.44%, with the rest of the power dispersed out in the error region. The power loss to the noise region is a tradeoff to achieve a smoother profile in the signal region, marked by a very small final fractional error of less than 1%. In fact, other variants of IFTA algorithm can achieve a higher diffraction efficiency albeit with a significantly noisier output profile [33].
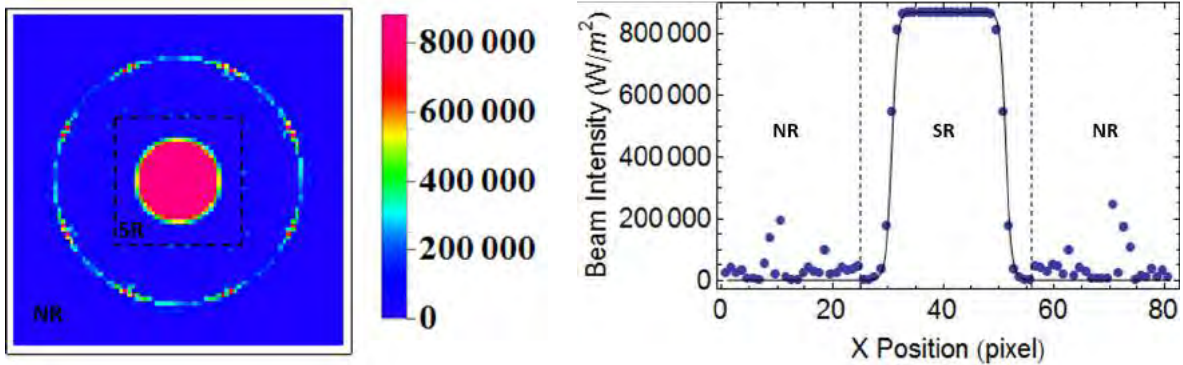

Figure 3.6: Intensity profile of the output beam in the Fourier plane after 200 iterations for the 400 μm target profile: the full 2D profile (Left) and the cut across the Y axis (Right). Note the boundary between the signal region (SR) and the noise region (NR).
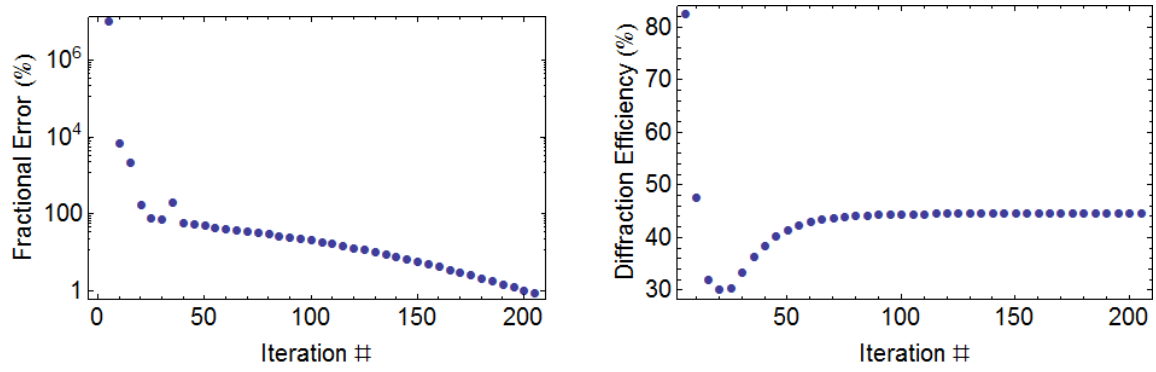
Figure 3.7: Evolution of the Fractional Error $\eta^{(n)}$ (Left) and the Diffraction Efficiency $\xi^{(n)}$ (Right) over the 200 iterations of the MRAF algorithm.
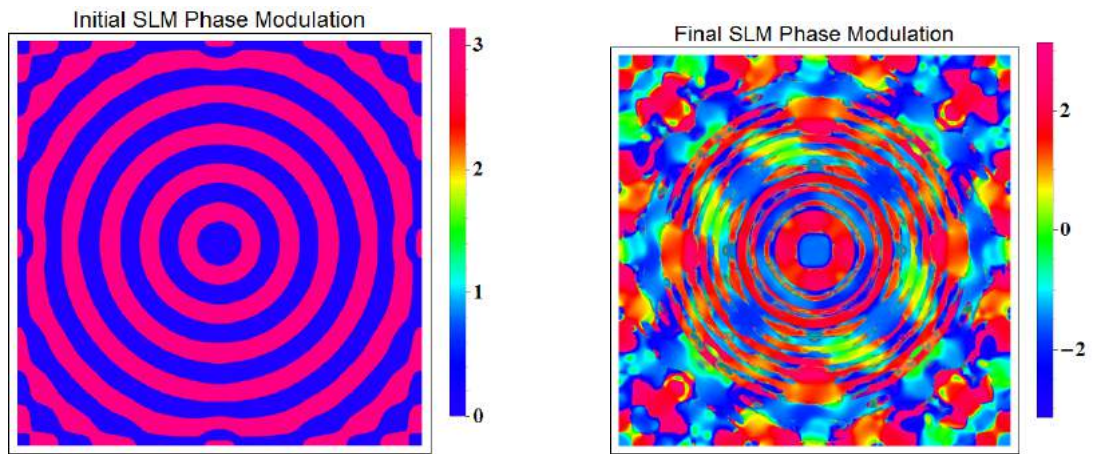

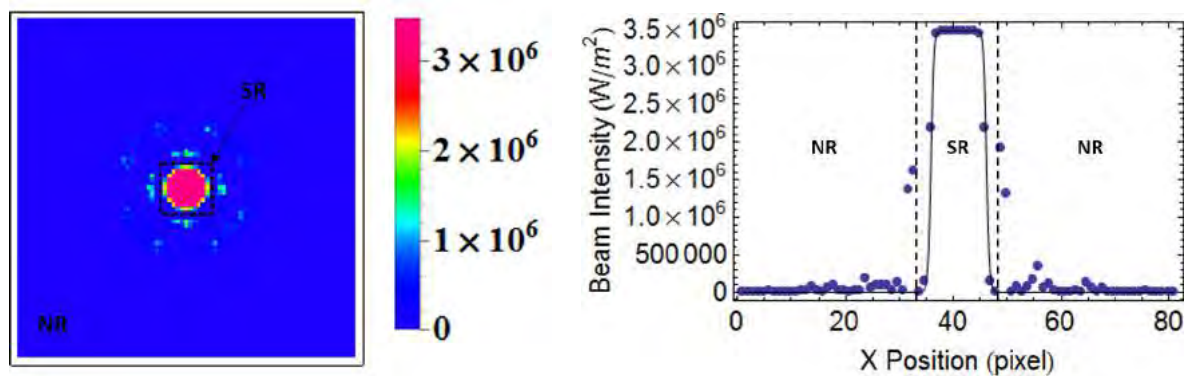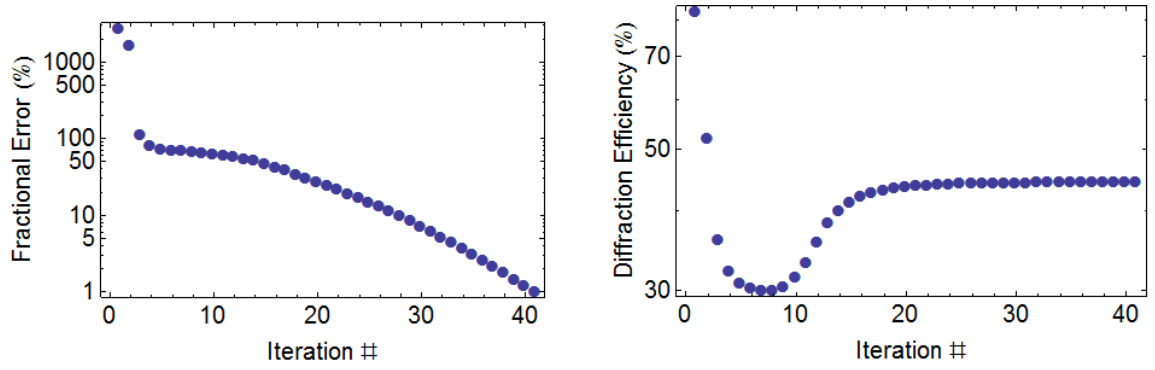Figure 3.8: Initial (Left) and final (Right) SLM phase guess with 200 iterations for the 400 μm target profile.

Figure 3.9: Intensity profile of the output beam in the Fourier plane after 200 iteration steps for the 200 μm target profile: the full 2D profile (Left) and the cut across the Y axis (Right).

20

Figure 3.10: Evolution of the Fractional Error $\eta^{(n)}$ (Left) and the Diffraction Efficiency $\xi^{(n)}$ (Right) over the 200 iterations of the MRAF algorithm for the 200 μm target profile.

Since the flat-top beam size which is relevant for our trap should be of the order of 100 μm, it is of interest to try this MRAF algorithm with a smaller target pattern. We first tried the algorithm with a flat-top target of 200 μm radius (approximately 5 times the diffraction-limited pixel size) and the corresponding mask of 600 μm in side. We find that even for this small target, the MRAF algorithm is still able to converge with a similar diffraction efficiency (44 %) and fractional error (1%) after 200 iterations. However, the algorithm finally stalls for a very small target. We tried the MRAF algorithm with a flat-top beam target of 120 μm radius (approximately 3 times the diffraction-limited pixel size) and with the corresponding resize of the mask to 400 μm. For this very small target, as we can see from figure 3.12, the fractional error is stalled at a relatively high 50% and we can observe the roughness of the output profile from its intensity profile (figure 3.11). This observation shows that the algorithm becomes less and less reliable when the target size approaches the resolution limit set by the Fourier Transform relation.
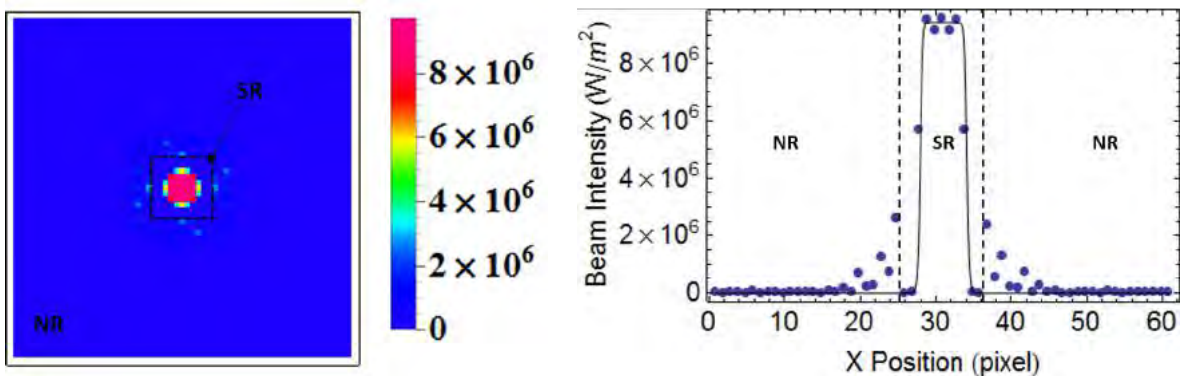

Figure 3.11: Intensity profile of the output beam in the Fourier plane after 200 iteration steps for the 120 μm target profile: the full 2D profile (Left) and the cut across the Y axis (Right).
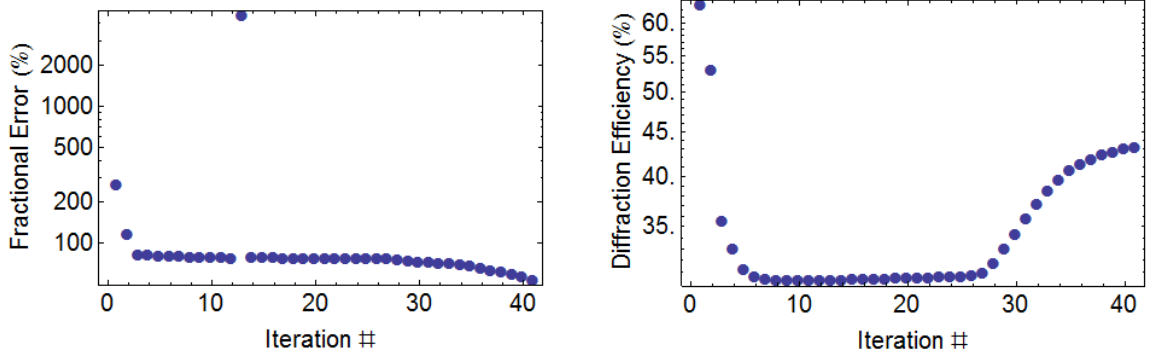
Figure 3.12: Evolution of the Fractional Error $\eta^{(n)}$ (Left) and the Diffraction Efficiency $\xi^{(n)}$ (Right) over the 200 iteration steps of the MRAF algorithm for the 120 μm target profile.
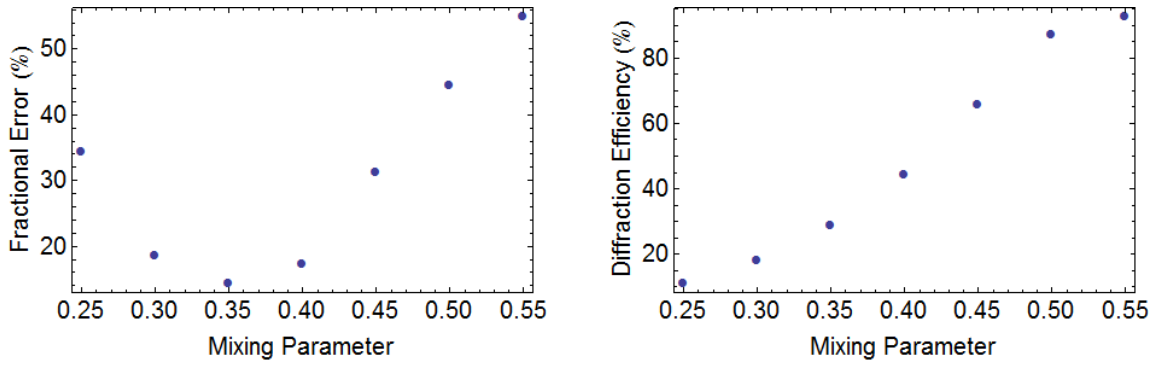

Figure 3.13: The Fractional Error (Left) and the Diffraction Efficiency (Right) in function of the mixing parameter m after 100 iteration steps.

Finally, we investigate the optimal choice of the mixing parameter m by performing this algorithm for 100 iteration steps, each with a different values of m. Note that the value of m is still constant in each iteration step. The diffraction efficiency and the fractional error achieved at the final stage of the iteration are plotted against the choice of m and are displayed in figure 3.13. We observe that the diffraction efficiency is always smaller for a smaller value of the mixing parameter. This phenomenon is a direct consequence of the structure of the mixed field (refer to equation 3.2.5), where the amplitude of the signal region component is proportional to m. However, the fractional error displays a minimum around the mixing parameter value of 0.35. This shows that if we opt for higher efficiency with a larger mixing parameter, the convergence to the desired pattern requires more iteration steps. The initial choice of the mixing parameter value of 0.4 is justified as a good compromise between a smooth output pattern and a reasonable efficiency.

Viability for the Realization of the Optical Trap

We dedicate this section to comment on the advantages and the disadvantages of performing the beam shaping with a phase-modulation SLM and this MRAF algorithm, particularly our optical trap application. From a favorable point view, we have seen that the MRAF algorithm produces a very smooth reproduction of the target intensity (shown by a very small fractional error) within a reasonable number of iterations. It has been show that a slight modification of this algorithm could generate a faster convergence with an even sharper target profile [37]. Secondly, the MRAF algorithm offers the advantage of having a natural extension to a feedback loop algorithm that is more practical in the real experimental situation. The feedback loop

algorithm can be constructed for example by using the measured field amplitude at the Fourier plane in the expression of the mixed field in equation 3.2.5 instead of the calculated amplitude by FFT. We expect this modification to improve the stability of the output profile against fluctuations present in the input profile. Finally, the optical setup involved is very simple, with only one lens involved in front of the SLM.

Several issues are to be taken note for the application of this scheme to construct our optical trap. First of all, we note that this MRAF algorithm (and for other beam shaping algorithms in general) is very dependent on the knowledge of the input profile. In experiment, this situation is rather inconvenient because it requires a stringent measurement of the beam profile at the SLM plane. This can be performed, for example by inserting a flip mirror which redirect the input beam into a CCD camera, placed at an equivalent plane to the SLM, which measures the intensity of this input beam at the SLM plane (refer to figure 3.14).
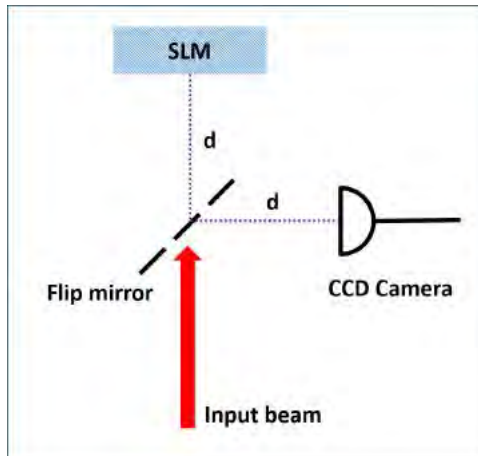

Figure 3.14: The measurement setup for the beam intensity profile at the SLM plane.

One drawback of this scheme is the resolution of the flat-top beam that can be achieved. We have seen that the MRAF scheme is limited by the diffraction-limited pixel size of 40 μm, which is comparable to the intended size of the flat-top. There are several ways to reduce this diffraction limit. First of all, we can use an SLM with a larger active surface. Our simulation assumes an SLM with 1024 pixels of 8 μm wide, hence a surface area of 8 mm by 8 mm. Unfortunately, to our knowledge, none of the commercially available SLM has an active area exceeding 10-20 mm. A second method we can try is to change the imaging lens to one with a shorter focal length. This solution, however, is not very practical due to the constraint of our experimental chamber which restricts the placement of the lens to be a certain distance away from the molecules. Lastly, we can place a telescope which relays the Fourier plane after the initial imaging lens to the plane of the molecules while demagnifying the flat-top beam. The disadvantage of this solution are the increased optical path length of the setup, and a possible degradation of the output beam profile.

A point to take note when applying the MRAF algorithm with a real SLM device is the discretization of the phase modulation provided by the SLM. Typical SLM devices are able to provide the full 0 to 2π phase modulation with an 8-bit (256 levels) discretrization. Consequently, it is more relevant to look at the diffraction from the discretized version of the modulation pattern. We investigate this effect by taking the final phase profile obtained for the 400 μm radius flat-top target after 200 iteration steps and discretizing it to 256 levels. The output diffraction pattern from the discretized phase modulation shows only a small error (see figure 3.15), keeping the same 44% diffraction efficiency and an increased of the fractional error from around 1% to 7%.
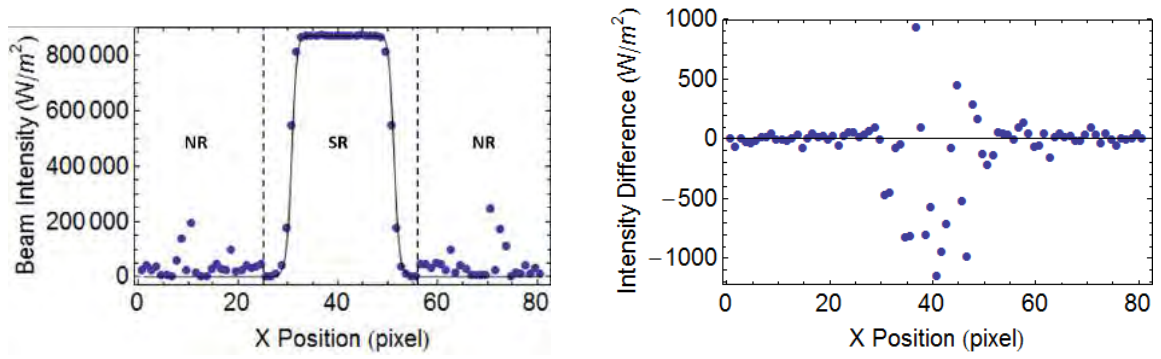
Figure 3.15: The intensity profile comparison of the diffraction pattern with a discretized phase modulation. (Left) A cut across the Y axis profile of the discretized-modulation diffraction intensity and (Right) the difference between the discretized-modulation and continuous-modulation diffraction intensity.

Another problem with the original MRAF scheme is the lack of control over the phase of the beam in the entire Fourier plane. For applications which are solely interested in the intensity profile at the output plane, the phase of the beam is of course of no importance. Yet, our optical trap is of the form of a lattice where it is desirable to keep the flat-top intensity profile over at least several lattice sites. If the phase of the beam is uncontrolled, the beam profile might rapidly change over a very short propagation distance. This is contrary to the case where the beam phase is kept flat in the output plane, where we expect the flat-top profile to be maintained over a distance of the order of the Rayleigh range of the beam [36]. We attempt to modify the MRAF algorithm by imposing a flat phase pattern in the signal region, i.e. modifying the expression of the mixed field into:

$$E_{mix}^{(n)} = (E_{flat})|_{SR} + (1-m)\left(E_{FP}^{(n)}\right)|_{NR}. \tag{3.2.10}$$

This modified algorithm shows a very poor result, as can be seen from figure 3.16 where we show the final output profile after 200 iterations, taking the 400 μm radius flat-top profile as target. We can see that even though we manage to keep a zero phase throughout the signal region, the amplitude pattern does not converge to a flat-top pattern. Hence, we are forced to abandon the control over the phase degree of freedom, which is a serious limitation of this algorithm for our application.
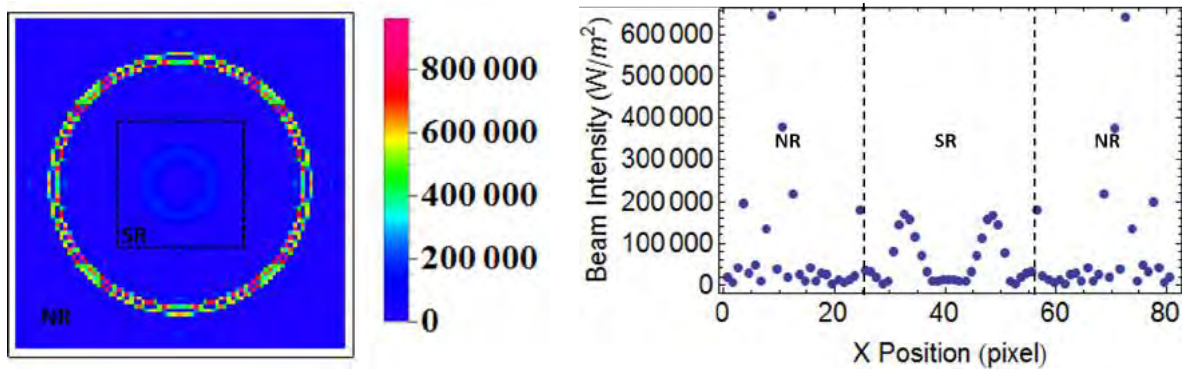

Figure 3.16: The intensity profile of the output beam in the Fourier plane with the modified MRAF algorithm after 200 iteration steps: the full 2D profile (Left) and the cut across the Y axis (Right). Note the boundary between the signal region (SR) and the noise region (NR).

From the SLM device point of view, the main concern with our application is the high power that we intend to employ for our trap. The liquid crystal type of SLM is especially prone to
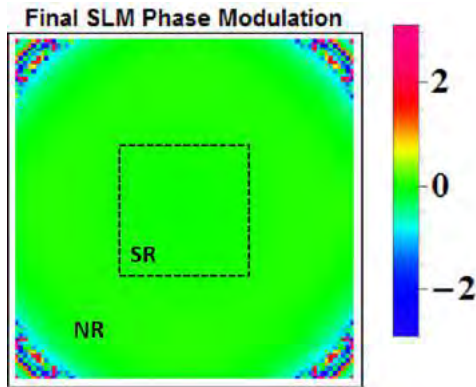
24

Figure 3.17: The phase profile of the output beam at the Fourier plane with the modified MRAF algorithm after 200 iteration steps.

damage when used with a high power beam as the liquid crystal molecules in the SLM may absorb the energy from the beam and boil, irreversibly damaging the device. In addition, both the LC and piston-type SLM are very costly compared to the amplitude-modulation type SLM which will be described in the next chapter.

To conclude this chapter, we have described the MRAF algorithm that is capable of generating a phase-only modulation to a Gaussian beam to produce a relatively smooth flat-top diffraction pattern. The iteration form of the algorithm is beneficial to be used as a feedback loop in the actual experimental implementation. However, as this algorithm is not capable of both the amplitude shaping to the desired target pattern and a flat-phase output pattern, it is not very suitable for the production of an optical lattice-type of trap geometry.

Chapter 4

Beam Shaping with an Amplitude-Modulation SLM

In this chapter, we explore a different beam shaping scheme which utilizes an amplitude-modulation type SLM instead of the phase-modulation type. As we have explained in previous chapter, an exact beam shaping requires both the phase and amplitude modulation simultaneously. In this section, we describe two possible beam shaping schemes that are applicable to optical setups with a binary amplitude-modulation SLM: the holography scheme and the Error Diffusion algorithm. These two schemes complete our overview of various beam shaping strategies, and thus we aim to provide some comparisons between them to motivate our choice of implementation, detailed in the next chapter.

4.1 Examples of Commercially Available Amplitude-Modulation SLM

As we have done in the previous chapter, we give a brief description of the amplitude-modulation type SLM devices. In this work, we focus only on two specific examples of devices, the Digital Micromirror Device (DMD) from Texas Instrument and the static amplitude modulation plate. Both are capable only of binary (on or off) amplitude modulation by design.

The Digital Micromirror Device (DMD)

This device was initially developed by Texas Instrument as a component for a projector. It consists of a 2D array of micromirrors, each mounted on a torsion hinge that can be tilted by an electrostatic actuator. In its active state, the device supports a command to tilt each individual mirror either to the left or to the right (see the right side of figure 4.1). Consequently, an incident input beam will be split into two components which are reflection from the pixels in the two different tilt states. These two components are separated in angle of propagation. By blocking off one component with a beam block, we effectively define one tilt state to be the 'ON' state which reflects the incoming input beam, and other to be the 'OFF' state which does not reflect the input beam. In this manner, the SLM acts as a binary amplitude modulation device.

This DMD device is packaged in different sizes, ranging from the small DLP3000 chip (608x684 pixels of 7.6 μm pitch) to the large DLP9500 chip (1920x1080 pixels of 10.8 μm pitch). The tilt angle of the pixels are + or -12^0 with respect to the substrate plane. The reflectivity of the device is specified to be around 67%, resulting from various factor such as the window transmission, micromirrors reflection factor, and the reduction from stray diffraction due to the pixelated structure and the interpixel gap [38]. Unfortunately, this device is not tested for applications with a high power laser as the input. The larger version of the chip
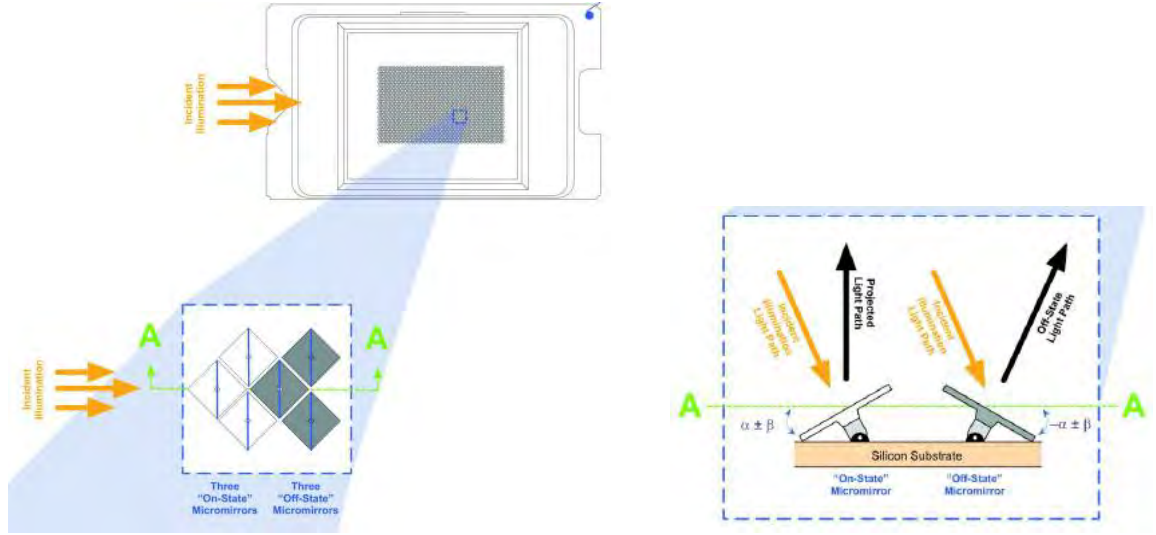
Figure 4.1: The cross section view of the DMD device. (Left) The top view and (Right) the side view.

supports a higher damage threshold due to the larger active area and a better heat dissipation system.

Static Binary-Amplitude-Modulation Plate

Just like the phase-modulation plate, a binary-amplitude-modulation plate is also realizable. In fact, we can fabricate this plate by a modified concept of a photomask. In the normal usage, a photomask is a fused silica glass plate (a very high damage threshold material) covered with an absorbing chrome metal layer. The photomask, as the name suggests, is used to block a lithography light such that the chrome pattern in the photomask is imprinted to the wafer. With current semiconductor lithography techniques, it is possible to imprint a 10-20 μm chrome pattern into the photomask, which will serve as the 'OFF' state pixels. By having a reflective chrome-metal layer instead, the photomask should be suitable for a very high power application.

4.2 Beam Shaping with the Holography Method

In this section, we will explore the first of the two beam shaping methods using an amplitude-modulation SLM that are covered in this chapter. The optical setup for this first scheme is identical to the one used in MRAF algorithm (see figure 3.3 in previous chapter), but with an amplitude-modulation SLM replacing the phase-modulation SLM in the input plane. This setup is well-known as a variation of the holography scheme, normally called the Fourier-Transform Holography [39] [40].

To understand how the conversion from a phase-modulation to amplitude modulation is done, we observe the following reflectance pattern:

$$r_{holo} \propto |E_{gauss} + E_{obj}|^2 = I_{obj} + I_{flat} + E_{gauss}E_{obj}^* + E_{gauss}^*E_{obj}, \qquad (4.2.1)$$

called the hologram pattern. In the above expression, the reflectance pattern is in the form of an interference between the input electric field E_{gauss} and a new electric field E_{obj} which will be determined later by our analysis. By modulating the input beam E_{gauss} with this reflectance pattern, we obtain the following field at the input plane:

$$E_{in} = E_{gauss} \cdot r_{holo} \propto \underbrace{(I_{obj} + I_{flat})E_{gauss}}_{\text{unmodulated field}} + \underbrace{(I_{gauss})E_{obj}}_{\text{object field}} + \underbrace{(E_{gauss}^2)E_{obj}^*}_{\text{conjugate field}}. \qquad (4.2.2)$$

28

In equation 4.2.2 above, we can distinguish three components of the field in the input plane. Firstly, there is a component proportional to E_{gauss}, called the unmodulated field because it is indeed a copy of the original Gaussian beam transmitted with a certain transmission percentage. However, we are mostly interested in the two fields which carry our imposed intensity pattern: the object field proportional to E_{obj} and the conjugate field that is proportional to the complex conjugate of the object field E_{obj}^*. In fact, we can exactly obtain a flat-top intensity pattern at the Fourier plane from this object beam, by equating its field to the inverse Fourier Transform of the flat-top beam field: $E_{obj} = \mathcal{F}^{-1}(E_{flat})$. A technical difficulty at this point is to separate the object beam from the unmodulated beam and the conjugate beam in the Fourier plane. One way to achieve this is to add an angle in the propagation of the object beam such that it is spatially separated from the unmodulated beam after a certain distance of propagation. In a similar manner to a plane wave, we can define a beam propagating in the direction given by its wavenumber $\mathbf{k}$ by adding a phase factor $e^{i\mathbf{k}\cdot\mathbf{r}}$ to the field expression. Thus, by defining the object beam as

$$E_{obj} = \mathcal{F}^{-1}(E_{flat})\, e^{i\mathbf{k}\cdot\mathbf{r}}, \tag{4.2.3}$$

we will see that the input Gaussian beam is split into three beams: the unmodulated beam propagating in the same direction as the input beam, the object beam deflected to an angle θ and its conjugate beam deflected in the opposite direction at angle $-\theta$. This separation allows us to collect only the object beam with the imaging lens, as depicted in figure **??**.
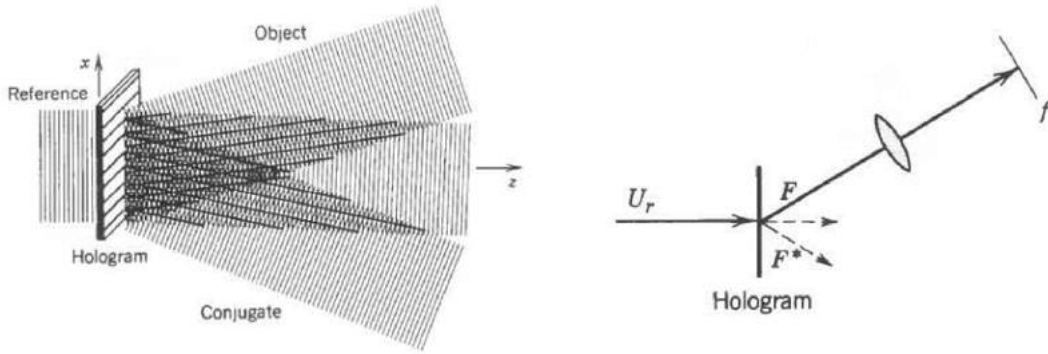

Figure 4.2: The schematic diagram of the Fourier-Transform Holography scheme. The modulated input beam is split into three beams, and the object beam is imaged by an imaging lens to form the desired pattern [39].

We perform a brief numerical study of this scheme. We take a 1024x1024 pixels discretization of the input and Fourier plane to optimize the Fast-Fourier Transform computation speed, but still taking the same pixel size as the DLP3000 SLM (7.637 μm). The input Gaussian beam waist is set to 3 mm, the same as the previous simulation. Similarly, the flat-top beam intensity is modeled as an order 20 Super Lorentz function of 400 μm radius. The focal length of the imaging lens is 300 mm. With this input and output definition, we calculate r_{holo} according to equation 4.2.1, normalizing the maximum reflectance to one. We then observe the beam profile at the Fourier plane, assuming that all three parts of the reflected modulated input beam are captured and imaged by the 300 mm lens.

In figure 4.3, we show our numerical simulation result of this holography scheme. In the left figure, we plot the log of the beam intensity profile in the Fourier plane. In the right part of the figure, we zoom in at the object beam which is diffracted to the side as expected from its propagation angle. Here we can see that the flat-top intensity pattern is exactly reproduced in this part of the beam.
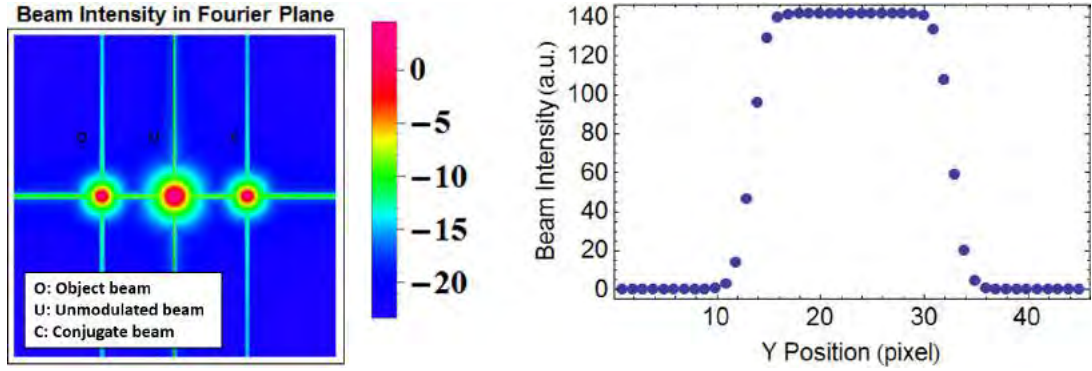
Figure 4.3: Numerical Simulation result of the Fourier-Transform Holography scheme. (Left) Log scale beam intensity profile at the Fourier plane and (Right) intensity profile of the object beam at the Fourier plane.

At this point however, we decided not to further pursue with this scheme due to several disadvantages that we found with this initial study. A major problem that we find in this simulation is the extremely low portion of the beam power that is distributed to the object beam. In figure 4.3, the intensity map is plotted in log scale due to the fact that the unmodulated beam contains more than 99.9% of the input power. Our several attempts in modifying the parameters of the simulation (input beam size, target beam size and order, adding a certain weight coefficient in the object beam part in equation 4.2.1) fails to appreciably increase the object beam power. Unfortunately, even if we manage to lower the power in the unmodulated beam, the power will still be at least split into two parts in the object and conjugate beam. This 50% efficiency in the perfect case is already comparable to the efficiency in the MRAF scheme (44%). Secondly, we find that a simple discretization procedure into a binary hologram reflectance pattern significantly degrades the beam shaping quality. In figure 4.4, we compare the object beam intensity profile with the ideal reflectance pattern r_{holo} and the binary approximation to this pattern by setting the reflectance to one at the positions where they are greater than 0.5, and 0 otherwise. As we can see, the binary reflectance hologram performs poorly and this is a big issue for our binary reflectance SLM.
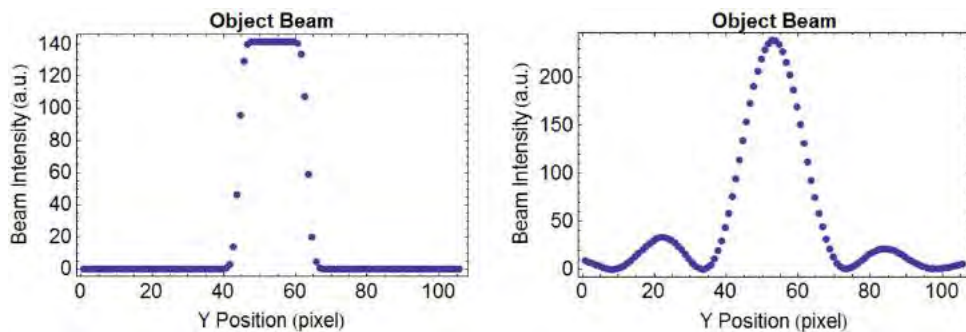

Figure 4.4: Comparison between the object beam intensity profile in the Fourier plane with the ideal (Left) and binary (Right) hologram.

In conclusion, this section describes our brief study of the Fourier Transform Holography scheme for the beam shaping purpose. The chief strength of this scheme is its ability to perfectly replicate any target pattern in form of the object beam, with only an amplitude modulation SLM as a requirement. Nevertheless, the efficiency and binary discretization issues remain a clear hindrance for an experimental adaptation of this scheme.

30

4.3 Beam Shaping with the Error Diffusion Algorithm

In the previous two beam shaping methods, we focus on controlling the spread of the beam in its propagation, then using a lens to control the diffraction pattern of the beam. A very straightforward method, however, can be implemented by setting a reflectance pattern provided by the SLM as the ratio between the target and the input field pattern (refer to figure 4.5). With this simple idea, the only technical difficulty to surmount is to provide a method to approximate the aforementioned reflectance pattern with a binary one. This is precisely the problem which the Error Diffusion algorithm tries to address.
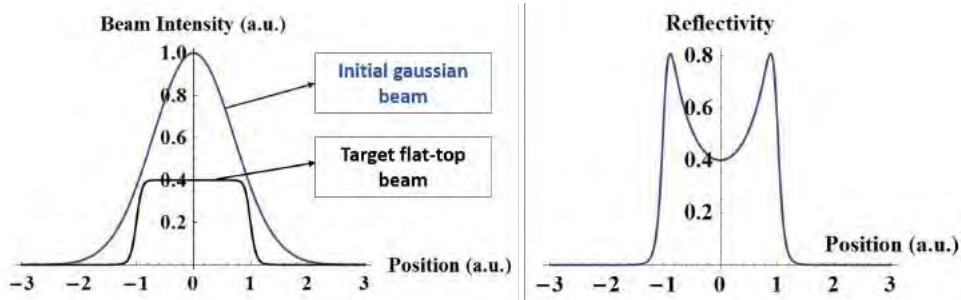
Figure 4.5: Beam shaping from a gaussian intensity pattern to a flat-top intensity pattern with a space-varying reflectivity pattern.

Optical Setup and Algorithm Description

The optical setup we consider with this algorithm is different from the previous one, since our goal is to exactly map the profile of the beam at the input plane (i.e. the SLM plane). To achieve this goal, we have to use an even number of lenses to form the so-called relay telescope arrangement. We start our analysis with the simplest setup involving a pair of lenses in figure 4.6 below:
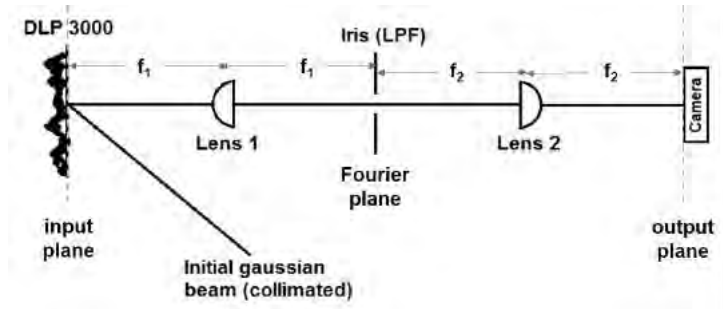

Figure 4.6: The schematic of the optical setup used in the error diffusion beam shaping algorithm.

There are four optical components involved in this scheme as we ca see from figure 4.6. The first one is the SLM, represented by the DLP3000 which we actually use in the experiment described in the next chapter. We mark the SLM plane as the input plane in this configuration. The SLM is placed at distance f_1 away from the first positive lens (of focal length f_1). The first lens is followed by the second lens (of focal length f_2) where they are separated by a distance $f_1 + f_2$. Finally, an iris or a pinhole is placed at the Fourier plane, which is located at distance f_1 behind the first lens. The output plane where the we impose the target pattern is located at distance f_2 away from the second lens. We place a camera icon at this location in spirit of our test setup. In the real experiment, this will of course be replaced by the trapped molecules.

The input beam at the SLM plane is assumed to be the Gaussian beam at its waist, as the case in previous two systems. The reflected beam from the SLM carries a binary amplitude modulation $s(x, y)$, where $s(x, y)$ is either 0 (if the pixel at (x, y) is turned off) or 1 (if the pixel at (x, y) is turned on). Hence, the electric field at the input plane is given by:

$$E_{IP}(x, y) = E_{gauss}(x, y) \cdot s(x, y). \tag{4.3.1}$$

Neglecting the iris for the moment, the electric field of beam at the output beam is proportional to the field at the input plane, due to the relay telescope arrangement ([32], refer to appendix A):

$$E_{OP}(x, y) = -\frac{f_1}{f_2} E_{IP}\left(-\frac{f_1}{f_2}x, -\frac{f_1}{f_2}y\right). \tag{4.3.2}$$

We recognize the usual magnification factor of a telescope which is just the ratio of the second and the first lens focal lengths. For our application, our goal is to set the output beam pattern to a flat-top pattern, preferably with a flat phase: $E_{OP} = E_{flat}(x, y)$. Let us first suppose that we were equipped with an SLM capable of producing an arbitrary reflectance pattern $r(x, y)$, where r can vary between 0 and 1. Considering the following reflectivity pattern:

$$r_{flat}(x, y) := E_{flat}(x, y)/E_{gauss}(x, y), \tag{4.3.3}$$

we will exactly obtain the flat-top beam as desired. Since our SLM is limited to binary modulation, the most natural approximation of r_{flat} is to set a pixel to be 'on' whenever the required reflectance is more than 0.5, and 0 otherwise:

$$s_{flat}(x, y) := \mathbf{1}_{r(x,y)\geq 0.5} \tag{4.3.4}$$

Equation 4.3.2 implies that if our telescope has an infinite numerical aperture (i.e. it captures all ray bundles diffracted from the SLM), the intensity we expect that the output plane with s_{flat} modulation is our Gaussian profile with dark spots at places where the pixels of the SLM are set to 0. An interesting situation takes place if we limit the numerical aperture of the lens system by installing an iris at the Fourier plane. Due to the Fourier Transform relation, a rapidly-varying spatial modulation (e.g. an 'off' and 'on' pixel beside one another) mostly contributes to the far-wing part of the beam intensity at the Fourier plane. The iris placed at the Fourier plane will therefore act as a low pass filter (LPF), filtering out high spatial-frequency modulation while leaving the slowly-varying component. As a result, the rapid-modulations are averaged out in the output beam profile.

To understand this averaging effect more precisely, let us consider the propagation of the input field E_{IP} from the SLM to the output plane. Neglecting the finite aperture of the lens, the field at the Fourier plane is given by the Fourier Transform of the input field multiplied by the transmission of the pinhole T_{ph}:

$$E_{FP}(x, y) = T_{ph}(x, y) \cdot \frac{1}{i\lambda f_1} \int_{-\infty}^{\infty} \int_{-\infty}^{\infty} E_{IP}(X, Y) e^{-2\pi i \frac{xX}{\lambda f_1}} e^{-2\pi i \frac{yY}{\lambda f_1}} dX dY. \tag{4.3.5}$$

Propagating to the output plane, the field there is another Fourier Transform of the field at the Fourier plane, but with the focal length factor from the second lens:

$$\begin{aligned}
E_{OP}(x, y) &= \frac{1}{i\lambda f_2} \int_{-\infty}^{\infty} \int_{-\infty}^{\infty} \left(E_{FP}(X, Y) T_{ph}(X, Y)\right) e^{-2\pi i \frac{xX}{\lambda f_2}} e^{-2\pi i \frac{yY}{\lambda f_2}} dX dY \\
&= \frac{1}{i\lambda f_2} \left(\mathcal{F}(E_{FP}) * \mathcal{F}(T_{ph})\right)\left(\frac{x}{\lambda f_2}, \frac{y}{\lambda f_2}\right) \\
&= -\frac{f_1}{f_2} \int_{-\infty}^{\infty} \int_{-\infty}^{\infty} \frac{r_{ph}}{\lambda f_1 \sqrt{X^2 + Y^2}} E_{IP}\left(-\frac{f_1}{f_2}x - X, -\frac{f_1}{f_2}y - Y\right) \\
&\quad J_1\left(\frac{2\pi r_{ph}}{\lambda f_1}\sqrt{X^2 + Y^2}\right) dX dY. \tag{4.3.6}
\end{aligned}$$

We note the use of convolution theorem in the second line of the above equation. We assume the pinhole to be spherical with an opening radius r_{ph}. The Fourier Transform of the pinhole transmission function is the Airy function, which can be written in terms of the Bessel function of the first kind J_1.

Notice the difference in the structure of the output field in case of an ideal telescope (equation 4.3.2) and a telescope with a pinhole in its Fourier plane (equation 4.3.6). In an ideal telescope, the field at the output plane is a one to one mapping from the input field. The output field at a certain image position (x, y) only depends on the input field at the object position $(-\frac{f_2}{f_1}x, -\frac{f_2}{f_1}y)$. In the presence of a pinhole, the output field at the image position (x, y) is now an integral over the entire input field, meaning that the field at that position is a weighted sum over contributions from the neighborhood of the object point $(-\frac{f_2}{f_1}x, -\frac{f_2}{f_1}y)$ in the input plane. The typical size of the neighborhood which contributes significantly to the output field is determined by the convolution kernel $K(X, Y)$:

$$K(X, Y) = \frac{r_{ph}}{\lambda f_1 \sqrt{X^2 + Y^2}} J_1 \left(\frac{2\pi r_{ph}}{\lambda f_1} \sqrt{X^2 + Y^2} \right). \tag{4.3.7}$$
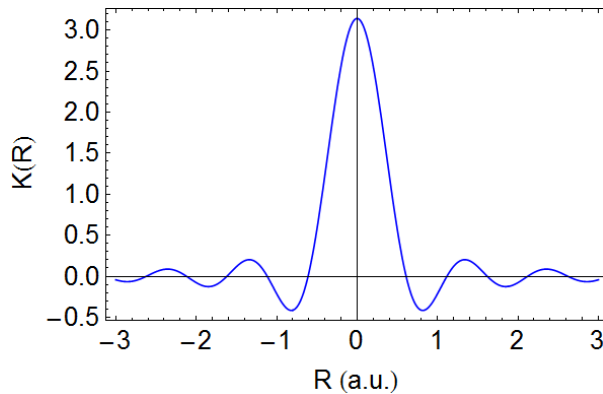

Figure 4.7: Plot of the convolution kernel function of the telescope with a spatial filter.

The plot of the convolution kernel (the Airy function) in figure 4.7 shows that the typical size of the neighborhood which contributes to the output field is of the order of the first minimum of this function which occurs at distance

$$R \approx 0.61 \frac{\lambda f_1}{r_{ph}}. \tag{4.3.8}$$

If we look back at our system, we can convert this distance in terms of the number SLM pixels. In this manner, we can think of the output profile as the average of input field from a bunch of pixels, centered at the pixel containing the object point.

With this concept in mind, an alternative method of approximating a variable reflectivity with a binary one has been studied by several authors. Since the amplitude of the output beam is an average over several pixels, one can achieve values between 0 and 1 by turning on the corresponding fraction of pixels over the averaging area. However, the main difficulty of implementing this idea is to correctly choose whether each pixel should be in the 'on' or 'off' state. According to equation 4.3.8, a smaller pinhole will increase the number of pixels to be averaged which should lead to a smoother modulation. At the same time however, a pixel contributes to a larger portion of the output beam. As such, it is not evident how to perform a deconvolution to directly determine the state of each pixel based on the target amplitude pattern.
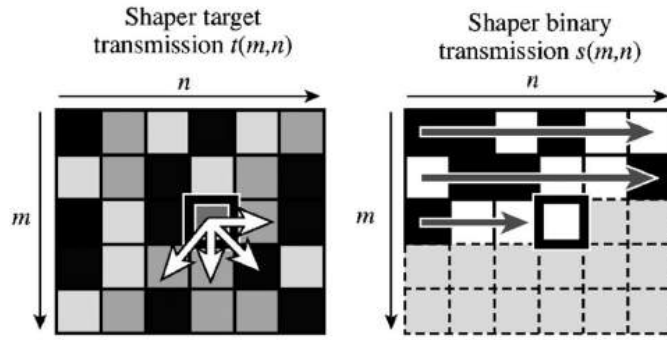
Figure 4.8: The diagrammatic illustration of the error diffusion algorithm. The ideal transmission matrix (Left) is processed sequentially and the binary transmission matrix is created based on the ideal transmission modified by the propagated error terms from its neighbors.

The error diffusion algorithm, first developed by Floyd and Steinberg [41] and later by Dorrer and Zuegel [42], attempts a different approach to this pixel assignment problem. At the beginning of the algorithm, the pixelated form of the target reflectance pattern r (equation 4.3.3) is calculated. We follow a sequential order of processing starting from the top left to the bottom right as indicated in figure 4.8 to calculate the binary pattern approximation $s_f lat$. Let us suppose that we have arrived to process the pixel in the nth row and m^{th} column. The binary pattern pixel is taken to be 0 if the target reflectance is less than 0.5, and 1 otherwise as we did previously. However, we notice that our approximation induces an error term $e(m,n) = r(m,n) - s(m,n)$ which needs to be compensated. This can indeed be done in the system with the spatial filter due to the pixel-averaging effect. The error diffusion algorithm takes advantage of this feature by spreading the error term to the neighboring unprocessed pixels, i.e. modifying their target reflectivity pattern to compensate for this error term. Refering to figure 4.8, there are four unprocessed nearest neighbors: the right side with coordinate $(m, n+1)$, the lower right side $(n + 1, m + 1)$, the bottom side $(n + 1, m)$, and the lower left side $(n + 1, m - 1)$. We adopt the error diffusion method described in [42], where the error term from the pixel position (n, m) is distributed to these four unprocessed nearest neighbors with the following weight coefficients:

$$r(m, n + 1) \rightarrow r(m, n + 1) + \frac{7}{16} e(m, n)$$
$$r(m + 1, n + 1) \rightarrow r(m + 1, n + 1) + \frac{1}{16} e(m, n)$$
$$r(m + 1, n) \rightarrow r(m + 1, n) + \frac{5}{16} e(m, n)$$
$$r(m + 1, n - 1) \rightarrow r(m + 1, n - 1) + \frac{3}{16} e(m, n). \tag{4.3.9}$$

It is suggested in some references that changing the distribution of the weight coefficients or involving more neighboring pixels do not significantly improve the result of this algorithm [42] [35].

Numerical Simulation Test of the Error Diffusion Algorithm

Simulation Methods and Parameters

As we did with the previous algorithms, we conduct a numerical simulation to test the algorithm. We choose the parameters to suit the DLP3000 chip which is in our disposition for the actual experimental test. The chip consist of 684x608 pixels of 7.637 μm pitch, which is arranged in a diamond configuration (refer to figure 4.9). In our simulation, we represent this pixel geometry by rotating the pixels 45 degree to obtain a rectangular tiles and then embedding it in a 950x950

pixel block as shown in figure 4.10. The area outside the mirror chip is not physical, and their reflectivity is always set to 0.
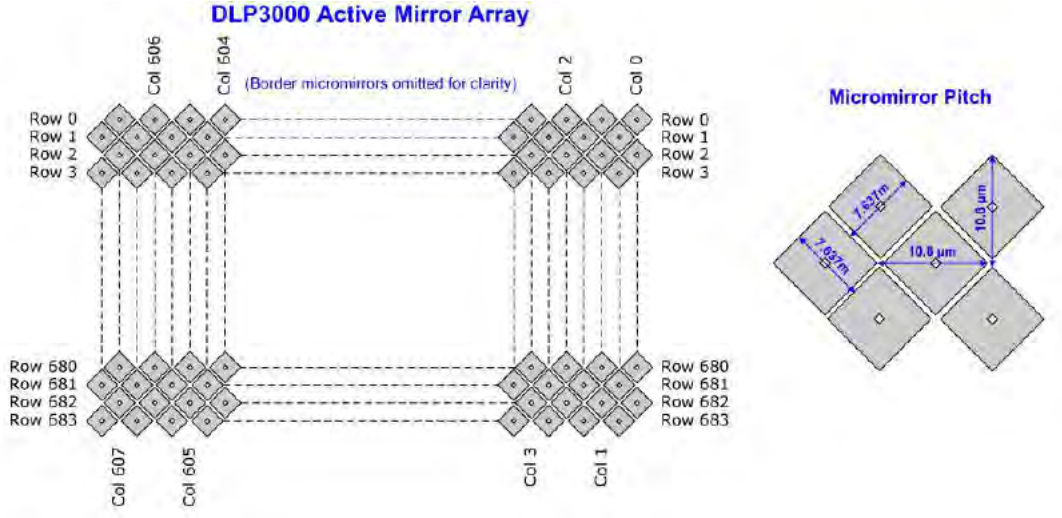

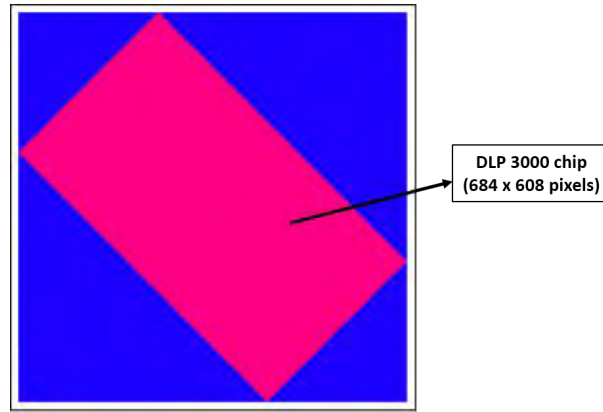Figure 4.9: The pixel structure of the DLP3000 [38].

Figure 4.10: The representation of the DLP3000 pixel geometry for the simulation. The pink area represents the pixels of the DLP3000 chip, while the blue are not physical.

The active area of the DLP3000 chip is a rectangle, 3.7 mm in height and 6.6 mm in width. We adjust our input Gaussian beam to the maximum size allowable by the chip aperture. Based on the argument of Campbell and DeShazer [43], the truncation at the aperture will induce a fringe at the far-field starting from the beam waist larger than around one-third of the aperture size. Hence, we choose the input Gaussian beam waist to be 1.2 mm. The waist is again located at the SLM plane, such that the beam phase at this plane is flat equal to 0. Since we are dealing with only the beam amplitude, we choose to normalize the beam such that the maximum intensity of this input beam is equal to 1:

$$I_{gauss}(x, y) = \exp\left(-\frac{2(x^2 + y^2)}{w_{Gauss}^2}\right), \qquad (4.3.10)$$

where w_{Gauss} denotes the waist of the Gaussian beam.

In this simulation, the flat-top intensity profile is again represented by a Super-Lorentz

function. We remind that this function takes the form:

$$SL_n(r) = I_{SL} \left[1 + \left| \frac{r}{w_{SL}} \right|^n \right]^{-1} . \tag{4.3.11}$$

Here w_{SL} is the radius of the flat-top beam. A special care has to be exercised in this situation, as we cannot allow the target reflectivity pattern to be larger than one. At the same time, the parameters of the flat-top pattern (the maximum intensity and the width) are to be chosen to maximize the shaping efficiency which in this case is equal to the power of the output profile divided by the power of the input Gaussian profile. By numerically integrating the Super-Lorentz (SL) function, the power of the flat-top profile and therefore the beam shaping efficiency is calculated for any height and width parameters. In figure 4.11, we show a sample of our efficiency calculation for order 8 and 20 Super-Lorentz function, intentionally removing the choice of parameters that leads to a greater than one reflectivity. We observe that the beam shaping is more efficient for lower order SL functions, as the pattern is less sharp and more similar to the Gaussian pattern. For the simulation, we choose the value of 0.4 for the maximum intensity of the flat-top and the width of between 0.67 (800 μm) and 0.75 (900 μm) of the original input beam waist. We take note that the physical radius of the flat-top beam in the output plane would be equal to the above set value, multiplied by the magnification of the telescope. For these values, the beam shaping efficiency is of the order of 40-50%.
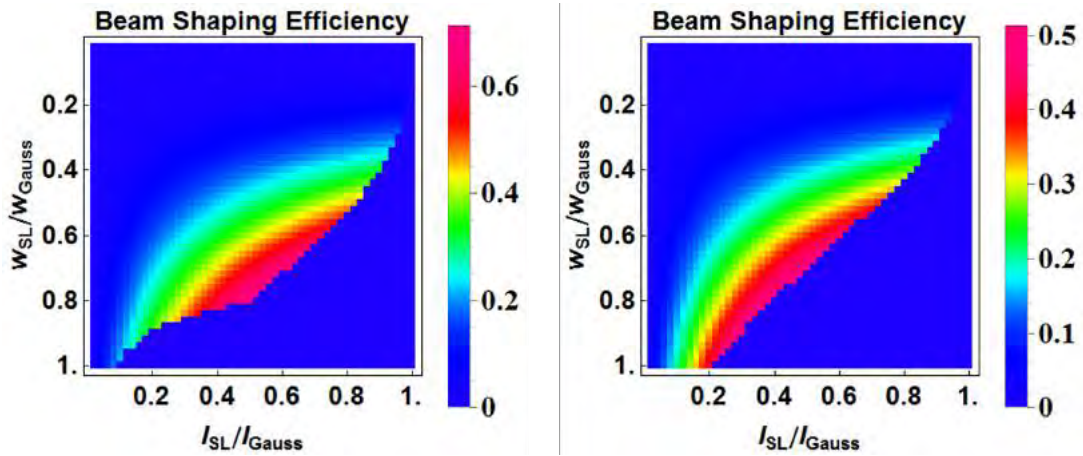

Figure 4.11: Beam shaping efficiency for various values of flat-top maximum intensity and width. (Left) Efficiency for the order 8 Super-Lorentz function and (Right) for the order 20.
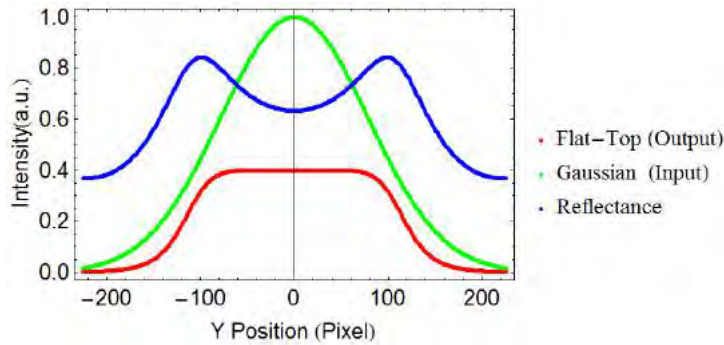

Figure 4.12: The normalized input gaussian beam intensity, the target beam intensity and the reflectance for this set of input and output. The input waist is 1.2 mm, the output beam is an order 8 SL function with 0.4 maximum intensity and 0.9 mm radius.

As for the optics, we take the first lens to be a 300 mm lens as is used in the test setup described in the next chapter. For this simulation, the focal length of the second lens only plays the role of determining the magnification of the system (i.e. the physical size of the flat-top beam in the output plane) but does not influence the beam shaping process. The opening radius of the pinhole is an independent variable in the simulation which will be investigated to optimize the smoothness of the output profile I_{OP}. This quality is analyzed in similar manner to the IFTA simulation. We fit the output profile to the SL function of the same order as the target, with its width and amplitude as the fitting variables. We reuse the same definition of the fractional error:

$$\eta = \frac{1}{N_{SR}} \sqrt{\sum_{SR} \left(\frac{I_{OP}^{(n)} - I_{fit}^{(n)}}{I_{fit}^{(n)}} \right)^2} \tag{4.3.12}$$

as previously, but with the measured region defined to be some area big enough to contain the entire flat-top profile.

The simulation is implemented in Mathematica. We first begin by initializing the input Gaussian profile centered at the mirror chip in the aforementioned 950x950 pixels representation. Following this step, we also define the Super-Lorentzian target intensity pattern, and calculate the target reflectance (refer to figure 4.12 for an example). We then define a subset area of the mirror chip large enough to contain the whole target pattern, where the binary pattern is processed according to the error diffusion algorithm. The pixel of the chip is set ot 0 outside this area. To model the effect of the pinhole, we discretize the Airy function (equation 4.3.7) into a matrix which we call the low pass filter (LPF) matrix. The output field is thus obtained by performing a discrete convolution between the LPF matrix and the matrix of the input beam multiplied by the binary modulation of the mirror chip. The output field is then fitted against the SL function and the fractional error is calculated. We repeat this procedure while varying the output target profile and the opening size of the pinhole.

Simulation Results and Discussion

In figure 4.14, we show the result of this error diffusion algorithm, shaping a 1.2 mm waist gaussian beam into an 8th order SL beam of radius 0.9 mm. As we can observe by eye, the resulting output beam is smooth, confirmed by a low fractional error of around 0.25%. While the opening diameter of the pinhole is varied, a particular trend can be observed in figure 4.15. For a large pinhole diameter (6 mm), the output profile is rather rough, reminiscent of the contrast of the binary reflectivity. As we decrease the pinhole opening, the pattern turns smoother, with the best output between 2 and 3 mm diameter (compare with the fractional error plot in figure 4.16). However, as we decrease the opening further, some fringes appear in the output pattern which could be a sign of over-averaging. Finally, we note that the efficiency of the scheme (the ratio between the power of the output and the input beam) is approximately 50% for the best output produced with 2 mm diameter pinhole. The number is consistent with the one obtained with numerical integration of the SL function, further supporting the success of the beam shaping procedure.

To get an estimation of the extent of the averaging by the pinhole, we could use a Gaussian beam propagation as a model. Suppose that we start with a Gaussian beam of waist w at the input plane. Following the Gaussian beam propagation, (see appendix B), the beam waist at the Fourier plane of the lens is given by:

$$w_{FP} = \frac{\lambda f}{\pi w}. \tag{4.3.13}$$

According to the criterion by Campbell and DeShazer [43], a Gaussian beam is transmitted with negligible disturbance if the opening radius of an aperture is at least twice the waist of the beam.
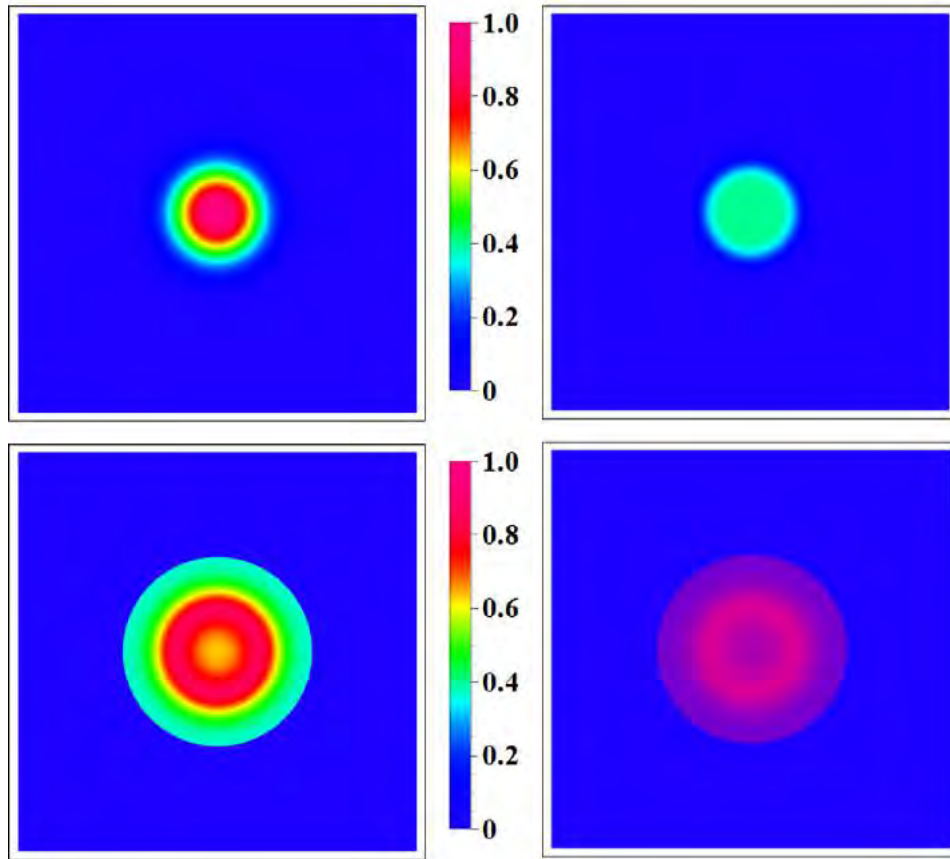
Figure 4.13: Input, output and reflectivity pattern in the numerical simulation of the Error Diffusion Algorithm. Top pictures: (Left) input Gaussian pattern and (Right) output SL pattern. The intensity is normalized to the peak intensity of the input pattern. Bottom pictures: (Left) target reflectance pattern r and (Right) binary reflectance pattern s obtained by the algorithm.
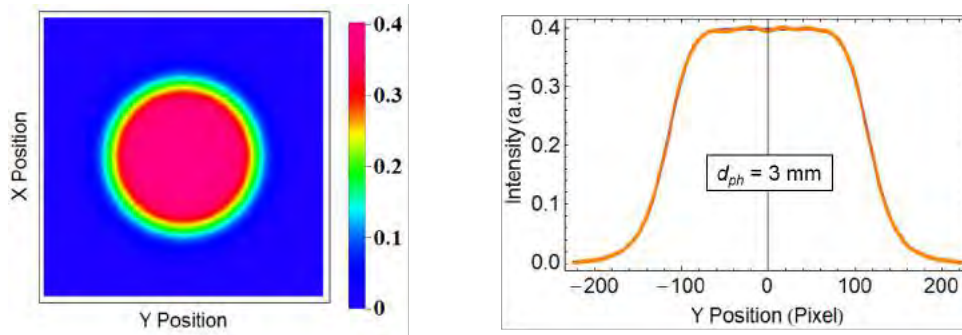

Figure 4.14: Output profile of the beam shaped with the Error Diffusion Algorithm. (Left) The 2D profile and (Right) the cut across X axis. Simulation parameters: input waist is 1.2 mm, output is the 8th order Super-Lorentzian with 0.9 mm radius, pinhole diameter is 3 mm.

Taking the pinhole diameter of 2 mm, the undisturbed transmitted Gaussian beam would be those with waist equals to 500 μm or less. Refering back to equation 4.3.13, the corresponding waist of the beam at the SLM plane is 200 μm or larger. Converting to the pixel size of the SLM, the waist of 200 μm is roughly equal to 27 pixels, which means the optimum averaging for this algorithm requires an average over a pixel block of 27 pixels radius. This method is useful as an estimate, especially when considering the effect of the aperture from other optical elements in the beam path.
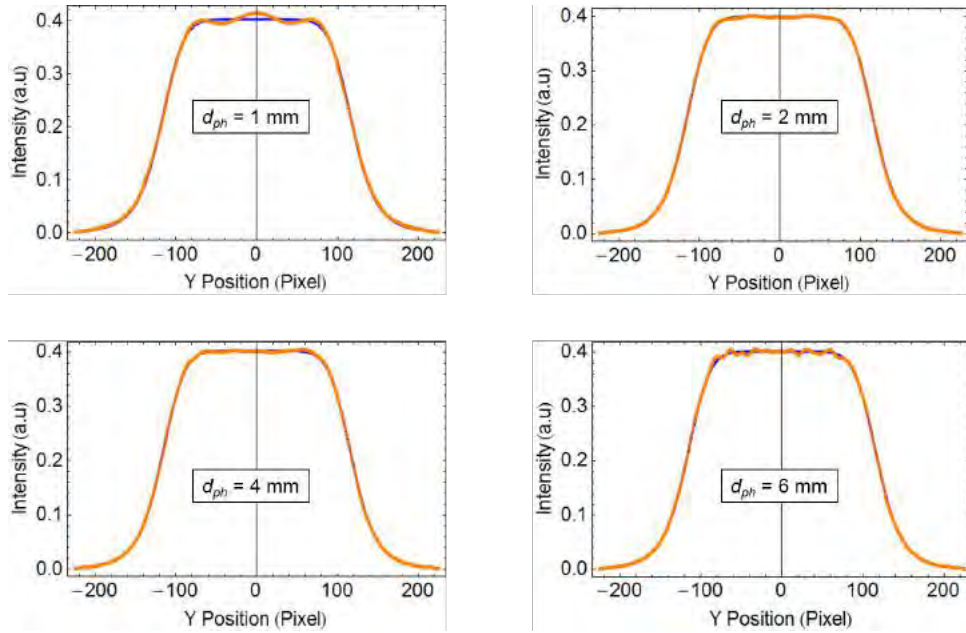
Figure 4.15: Cut across X axis of the output profile from the error diffusion algorithm with various pinhole opening diameter d_{ph}. Orange dots are the simulated beam profile, while the blue line is the fit. Simulation parameters: input waist is 1.2 mm, output is the 8th order Super-Lorentzian with 0.9 mm radius.
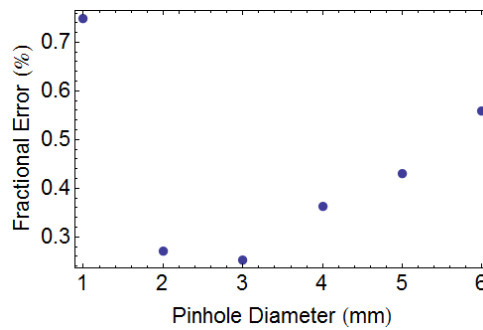

Figure 4.16: Fractional error of the beam shaped with the error diffusion algorithm in function of pinhole diameter. Simulation parameters: input waist is 1.2 mm, output is the 8th order Super-Lorentzian with 0.9 mm radius, pinhole diameter is 3 mm.
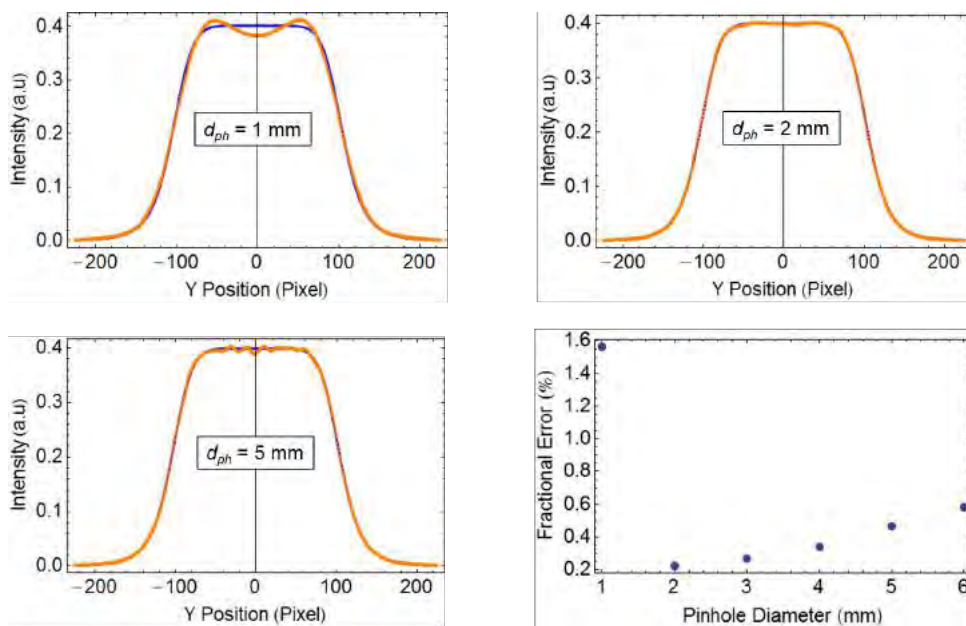

39

Figure 4.17: Cut across the X axis of the output profiles of the beam shaped with the Error Diffusion Algorithm, and the fractional error plot in function of pinhole diameter d_{ph}. Simulation parameters: input waist is 1.2 mm, output is the 8th order Super-Lorentzian with 0.8 mm radius.

To further our exploration with this algorithm, we make a comparison with a smaller radius target profile. The pattern we use is the same 8th order SL function but with a smaller radius of 800 μm. As we can see from figure 4.18, we found that the output profiles display a similar trend as observed with the larger target radius: a fringe for 1 mm diameter pinhole, a smooth pattern for 2 - 3 mm diameter which gradually grows more noisy for larger pinhole diameters. The fractional error is still of the order of 0.2%, but the efficiency is lower (40% for both simulation and theoretical) due to the smaller target size.

In addition, we also compare the performance of this algorithm with a steeper target profile. For this, we set the target to be the order 20 SL function of radius 900 mum. We observe that the error is larger in comparison to the order 8 SL target, and that the optimum pinhole diameter shifts to a larger value. The best profile is found at 4 mm diameter, with a fractional error of 0.48%. The efficiency for this steeper target is also smaller at 46%. However, this shows that a very sharp flat-top shape is theoretically achievable with this scheme.
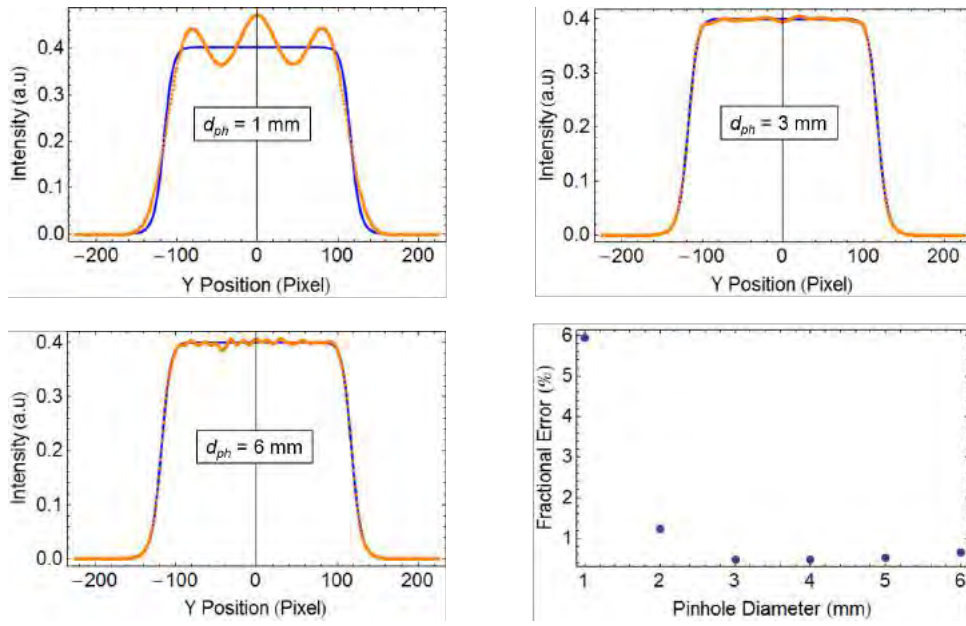

Figure 4.18: Cut across the X axis of the output profiles of the beam shaped with the Error Diffusion Algorithm, and the fractional error plot in function of pinhole diameter d_{ph}. Simulation parameters: input waist is 1.2 mm, output is the 20th order Super-Lorentzian with 0.9 mm radius.

Viability for the Realization of the Optical Trap

As we did with the previous algorithms, we address several comments on the application of this Error Diffusion Algorithm with the binary amplitude-modulation SLM on our optical trap setting. To start with the positive notes, the algorithm performs very efficiently to produce a smooth flat-top profile with only one step processing. The fractional error of the output beam is of the same order as the one produced by the MRAF algorithm, and we don't run into trouble of having to define a very small target of several pixels in size (i.e. higher resolution). The efficiency of the two schemes (MRAF and Error Diffusion) are comparable, 44% in the case of MRAF and around 50% for the Error Diffusion algorithm. The optical components involved (a pair of lenses and a spatial filter) are also still relatively simple. However, caution must be exercised to ensure that the spatial filter is not damaged when the input power is high.

Unlike the MRAF algorithm, this algorithm does not modulate the phase of the beam.

Therefore, if the input beam is well placed at the SLM plane and the telescope is well set, the output beam will have a flat phase front. A deviation from this condition will induce a quadratic phase curvature to the output profile, which means that the flat-top intensity profile occurs when the beam is already expanding or shrinking. Barring those misalignment effects, the flat phase front is exactly what is needed for the optical lattice setup.

Nevertheless, one disadvantage of the Error Diffusion algorithm is its non-iterative form. As mentioned in the previous chapter, an iterative algorithm is important to adapt the SLM modulation against fluctuations, misalignment, and imperfection of the input profile since the beam shaping scheme is always very dependent on the input. A suggestion to circumvent this problem, for example from [44], is to implement a separate iterative correction method to the initial binary modulation pattern provided by the algorithm.
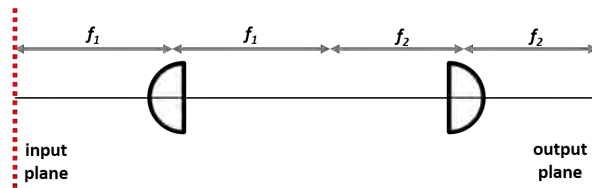

Figure 4.19: Optical setup of a relay telescope.

Another point to take note from this algorithm is the size of the output profile. As previously mentioned, the physical radius of the flat-top beam is equal to the radius set in the simulation, multiplied by the demagnification of the telescope. This means that if we convert a 1.2 mm waist Gaussian beam into a 0.9 mm radius flat-top pattern, and we wish to have a 50 μm radius flat-top beam for the trap, we need to provide a factor of 18 demagnification using the telescope alignment. The conventional relay telescope setup (figure 4.19) provides a magnification factor of f_2/f_1 for a total length of $2f_1 + f_2$. We see that to achieve a demagnification, the first lens must be of a longer focal length than the second. Due to the constraint of the vacuum chamber and a possible aberration, the last lens before the atoms should not be smaller than 50 mm in focal length. Even then, if we only use one telescope to provide the factor 18 demagnification, the first lens have a focal length of at least 900 mm, and therefore a total telescope length of 1.9 m, which is very space-consuming. To save space, we can employ several strategies. First of all, we can stack two telescopes instead of only one. For example, taking two pairs of a 200 mm followed by a 50 mm lenses will give a total demagnification of 16 (output radius of 56.25 μm) for a total length of 1 m. Secondly, we can use only a single lens to provide a demagnification. We know from classical optics that placing an object at distance d_1 in front of a lens of focal length f, the image is formed at distance $d_2 = \frac{d_1 f}{d_1 - f}$ with a magnification factor of $|d_2/d_1|$ (refer to figure 4.20). Hence, if the object distance is equal to nf, where n is larger than one, the image is found at distance $nf/(n-1)$ with a demagnification factor of $n-1$. For example, with a single 50 mm lens, we can achieve a factor 16 demagnification with a shorter setup length of 853 mm (object distance is 800 mm, image distance 53 mm). However, there are two drawbacks of this setup: a much reduced numerical aperture caused by the long object distance and the inevitable addition of a quadratic phase factor. In fact, the extra quadratic phase factor can cause a very severe focusing/expansion of the beam which have to be avoided in the lattice setup. We found that the additional quadratic phase is less important if the input beam is of smaller size. Therefore, the single-lens demagnification is more suitable to be used as a second stage of a two-stage magnification setup (preceded by a relay telescope, e.g. in reference [45]). Thirdly, we can of course, decrease the input beam waist as necessary. The main disadvantages for this is the higher peak intensity of the input beam which requires an SLM with a very high damage threshold and the reduced number of pixels which effectively participates in the beam shaping process.
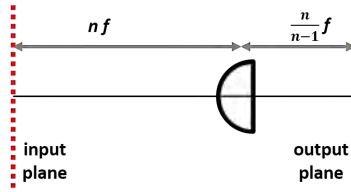
Figure 4.20: Optical setup of a single-lens demagnification telescope.

Finally, the SLM that we intend to use with this algorithm is the DLP3000 chip. The SLM still suffers from a low damage threshold, as it has a small active area and no particular heat dissipation design, in addition to a relatively smaller reflectivity factor (around 67% as described in previous section). However, the chip is available at an affordable price, and we choose to proceed with this solution for a proof-of-concept experiment.

In conclusion, we have described the Error Diffusion algorithm that generates a binary amplitude modulation approximation to an unconstrained amplitude modulation beam shaping. Used in combination with a low-pass spatial filter, the binary reflectance pattern is able to perform a smooth and relatively efficient beam shaping from a gaussian to a flat-top intensity pattern. In particular, the scheme generates a flat phase front flat-top beam, which is suitable for the optical lattice trap design.

Chapter 5

First Experimental Results of the Optical Lattice Setup

We present some early results of the implementation of the beam shaping scheme with the Error Diffusion algorithm and the DLP3000 mirror chip. We will start by introducing the laser system which we intend to use to form the actual optical trap, followed by some preliminary measurements to characterize the system. Finally, we present our early measurement results of the beam shaping from the laser output to a flat-top beam profile.

5.1 The Laser System

The laser system in our disposition is the Mephisto MOPA series from Coherent Inc. [46]. The laser features a high power (up to 55 W) output from several MOPA amplification stages of the laser diode source, and lases at 1064 nm wavelength. In addition, the laser output beam has a very narrow linewidth of ≈ 1 kHz and is equipped with a noise suppression module (for more information, refer to the data from the laser manual at [47]).

Our first approach is to control the power output of the laser. The high power output of the laser needs to be accounted for and excess power dump properly in each step, to prevent the damage on optical components and the risk of injury to the user. The output power of the laser depends on the provided current and therefore, we make a measurement of the beam output power in function of the applied current. The measurement is taken with the S322C thermal power sensor from Thorlabs, that has a damage threshold of 200 W [48]. The sensor is placed approximately 55 cm away from the output port of the laser. The measured data is displayed in figure 5.1.
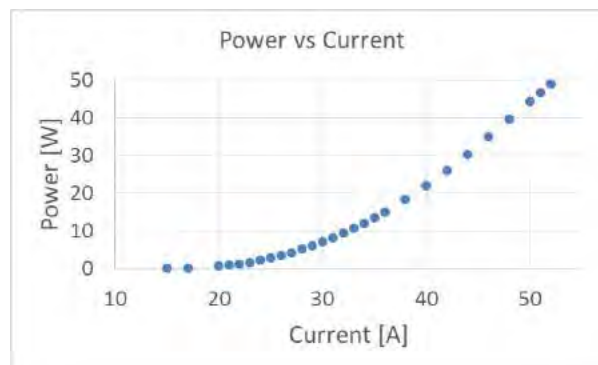

Figure 5.1: Laser output power in function of the applied current to the laser box.

The lasing threshold is found to be around 10-11 A. We find that the output power grows to around 50 W at 52 A current but the device can provide even more power at higher current.

Nonetheless, we decide to stop at 52 A since we don't really need to use the full power of the laser. This data is used in subsequent discussions as our means to convert the reading of the current to the actual laser power.

Figure 5.2: Mounted optical isolator, with safety tubes to house the high power beam.

Our next step is to install an optical isolator directly the laser output. The optical isolator is an optical element which attenuates any back-reflection which would be directed back to the laser. The isolator in our setup is the Faraday-type isolator from EOT, designed for high power beam at 1045 to 1080 nm wavelength [49]. A Faraday isolator typically consists of a big magnet (Faraday rotator) placed between two polarizing beamsplitter cubes (PBS). For a beam propagating in the forward direction (entering from the input face and exiting through the output face), the rotator rotates the beam polarization by 45°due to the Faraday effect, and thus it will be transmitted by the output PBS. In the contrary, for a beam propagating in the backward direction, the beam polarization is rotated by -45°, and thus the beam will be reflected by the input face PBS, preventing it from reaching the laser port.
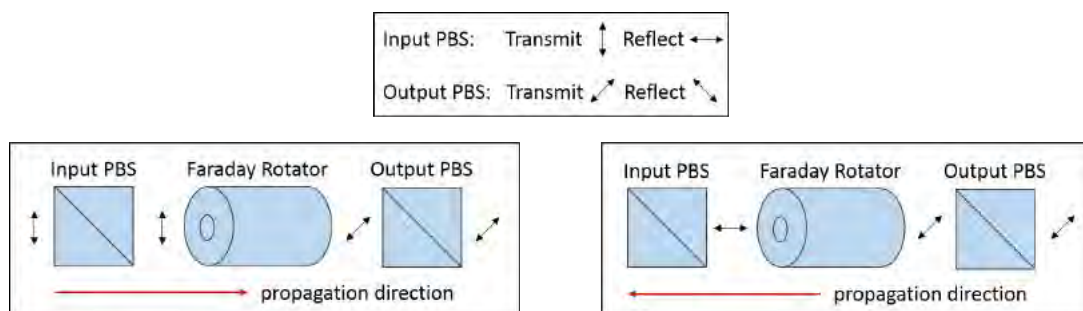

Figure 5.3: Schematic diagram of a Faraday isolator.

We conducted two measurements for the isolator, to determine the transmission and the isolation figures. For the transmission, the isolator is placed directly in front of the laser output, and we measure the transmitted power of the beam. We optimize the transmission of the isolator by rotating the whole isolator body to match the polarization of the beam with the entry PBS. The transmission of the isolator is calculated as the ratio between the measured transmitted beam power with and without the isolator, and it is plotted in figure 5.4 in function of the input beam power. This transmission factor is greater than 95%, and it tends to increase at higher beam power perhaps due to a better beam mode at higher power. To measure the isolation factor of the isolator, we mount the isolator in reverse, such that the beam now enters from

the exit face. The beam therefore simulates the back-reflected light from an optical component, and the transmission from the input face is the leakage which would go back to the laser port. We place a half waveplate (HWP) before the isolator to match the beam polarization with this exit face PBS as to maximize the power of the leakage beam. The isolation of the isolator is defined as the ratio between the transmitted leakage beam power and the power of the input beam. As we can see from figure 5.4, the average isolation figure is about 0.1% (30 dB), which is consistent with the specification from the device datasheet.
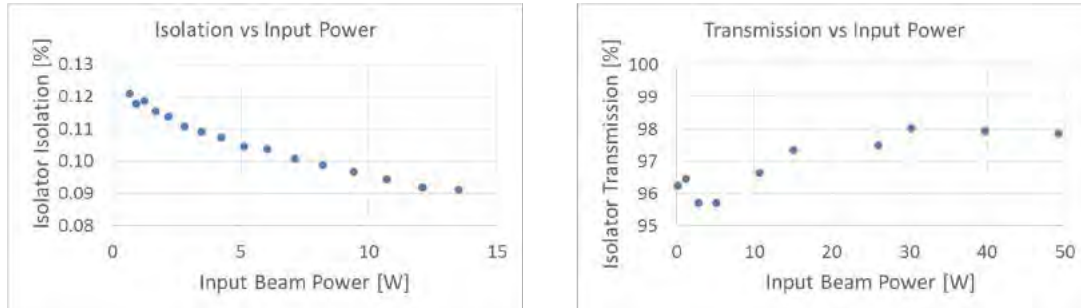
Figure 5.4: The transmission (Left) and isolation (Right) of the optical isolator in function of the power incident to the isolator.

5.2 Beam Profile Measurement Before the SLM

Once we establish the laser output through the optical isolator, our next step is to prepare and measure the beam profile for the beam shaping scheme. The beam profile measurement is done with the Beam Master device from Coherent [50]. This device consists of a silicon photodetector preceeded by two main perpendicular knife edges. As a knife edge slides along an axis, the detector measures the power of the unblocked part of the beam. Hence, the change of the measured power in a particular position is equal to the beam intensity, integrated along the transverse direction, at that position. The beam master measures the integrated intensity profile along the two perpendicular axes of the knife edges. The device has a square aperture of 9 mm side and it can measure a beam as small as a few micrometer in size with a typical resolution of 1 μ[51].
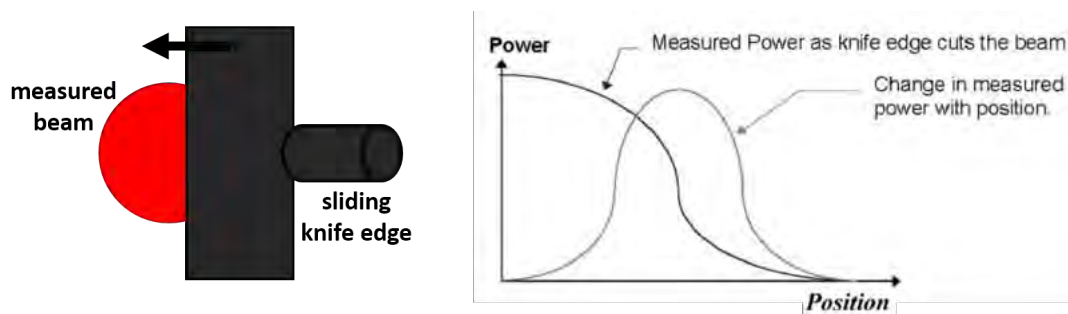

Figure 5.5: The principle behind the operation of the Beam Master device [51].

Before feeding the beam into the Beam Master, we need a considerable attenuation of the high power beam to avoid damaging the device. The Beam Master is equipped with a slot for an attenuator in front of its sensor. However, even with the thicker attenuator, the maximum specified input power is 1 W. We have the option of putting additional attenuators in front of the device, however we prefer not to do so for two reasons. First of all, attenuators usually introduce unwanted fringes due to some interference or due to some pollutant in either face of

the attenuator. Secondly, the attenuators in our disposition are absorptive attenuators which is not suitable for a high power laser. A factor 100 attenuation of a 50 W beam means 49.5 W absorbed power by the attenuator, a definite cause of damage to this component.

Instead of placing attenuators, we decide to attenuate the power of the beam with several components, as shown in figure 5.6. Directly after the isolator, we place the pair of a half waveplate (HWP) and a beam sampler. The beam sampler is in essence an uncoated glass plate which reflects between approximately 1 to 10% of the beam power, depending on the polarization of the beam. The remaining of the beam power is transmitted through the beam sampler, and is dumped to the Thorlabs power meter (for power measurement) or any other beam dump. We place a negative lens before the dump to enlarge the beam, thus reducing its peak intensity. To eliminate the further use of attenuators, we place a block containing a polarizing beamsplitter cube (PBS) followed by a HWP and another PBS. The first PBS cleans up the polarization of the beam, transmitting only the horizontally polarized component of the beam. The HWP allows a rotation of the beam polarization before the final PBS, hence allowing us to choose the power transmitted by this PBS. With this arrangement, the final beam output (the one transmitted by the last PBS) can be tuned between ≈ 0.5 mW to 300 mW, for the input power of 50 W (laser current of 52 A). We remark that the majority of the optical components (mirrors, lenses, PBS, and beam sampler) are made from the UV Fused Silica substrate that has a high damage threshold.
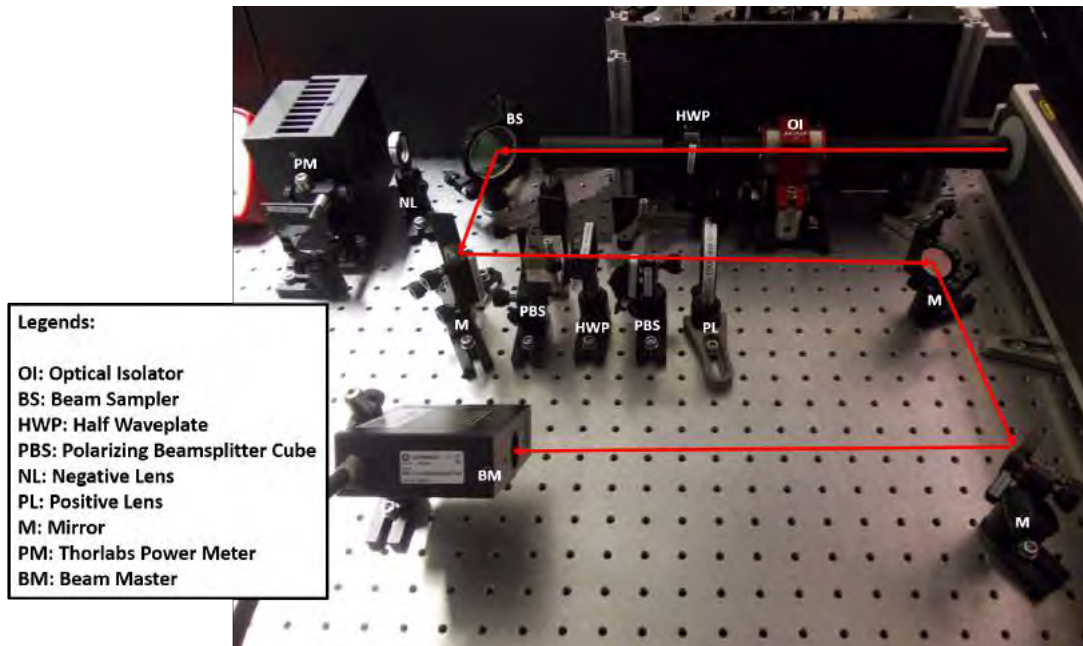

Figure 5.6: Experimental setup for the beam profile measurement. The red arrow indicates the path of the main beam, measured by the Beam Master.

Initial Beam Profile Measurement

For the first measurement, we measure the profile of the beam directly after the PBS block. The purpose of this measurement is two-fold: firstly, to check that the laser output profile is Gaussian and secondly, to find out where and how big is the beam waist. We record the integrated intensity profile along the horizontal and vertical axis with the Beam Master for several values of distances between the laser output port and the Beam Master and for different power of the beam.
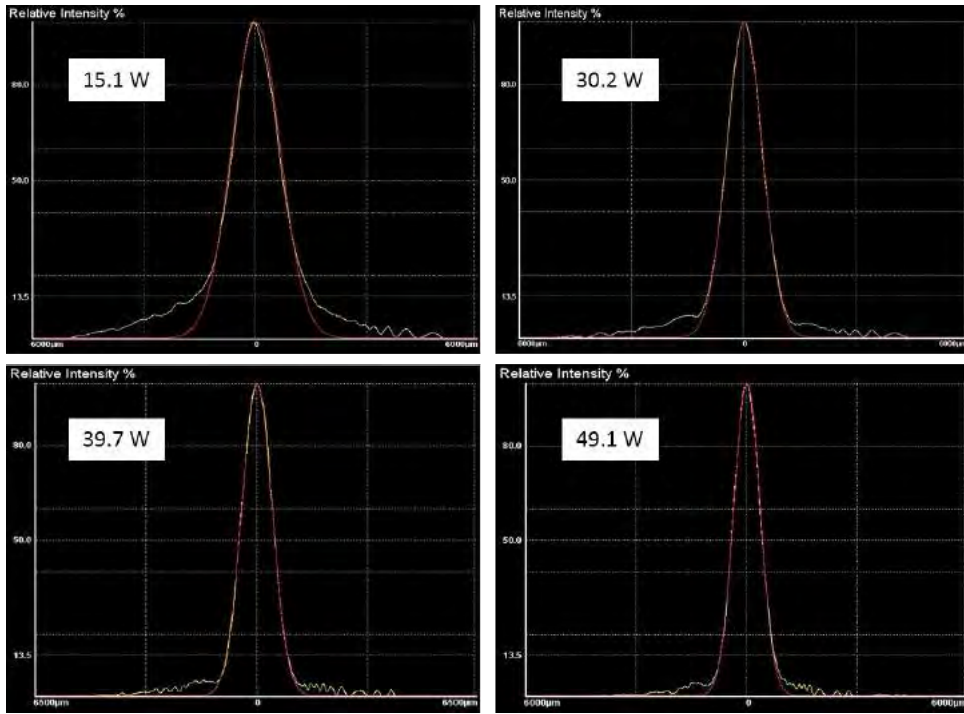
Figure 5.7: Vertical axis intensity profile for some selected beam power. The sensor is 580 mm after the output port. Yellow line is the measured intensity while the red line is the gaussian fit to the measured profile.

We start with the comparison of the intensity profile for various beam power. In figure 5.7, we display the intensity along the vertical axis for different beam powers. As can be seen from the figure, the intensity profile is a Gaussian peak with some additional background intensity on the wing. Furthermore, we observe that the background intensity, which can be attributed to the spontaneous emission from the amplification crystals, contributes to a smaller percentage of the total power when the beam power is higher. Hence, we decide to keep the laser power at 49.1 W (52 A of applied laser current) for all the subsequent measurements.
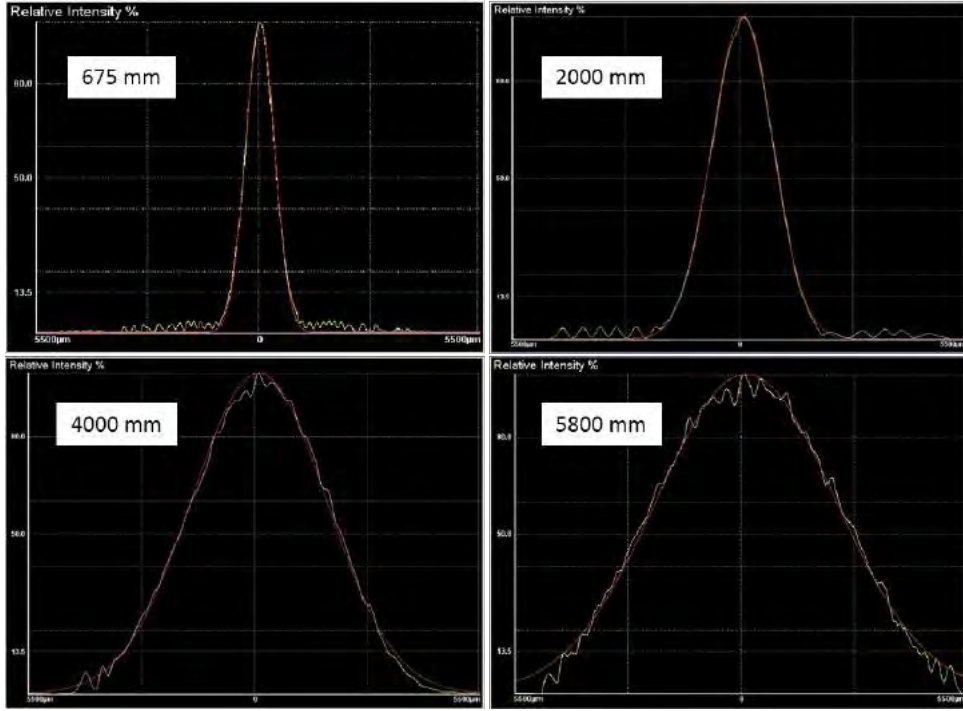
Figure 5.8: Horizontal axis intensity profile of the laser output beam for some selected distances. Yellow line is the measured intensity while the red line is the gaussian fit to the measured profile.

In figure 5.8 and 5.9, the plot of the integrated intensity profile along the horizontal and vertical axis respectively, for several distances are displayed. Comparing the beam profile with the built-in Gaussian beam fit, we observe that the profiles in both directions are very well Gaussian even for long propagation distances. In distances nearer to the output port, we observe some fringes at the wing of the profile, while for the long distances, the beam expand and we can see some noise around the central Gaussian peak.

Subsequently, we analyze the propagation profile of the beam by fitting the intensity profile both vertical and horizontal directions to a Gaussian distribution. In figure 5.10, we plot both the beam spot size in horizontal direction and the beam ellipticity, defined as the ratio of the beam spot size in the horizontal and vertical directions, in function of position (the laser output port is defined as the origin). The spot size profile shows that the beam waist is located near the output port of the laser. Fitting the spot size function to the formula given by the gaussian beam propagation: (refer to appendix B)

$$w(z) = w_0 \sqrt{1 + \left(\frac{\lambda(z - z_0)}{\pi w_0} \right)^2}, \tag{5.2.1}$$

we determine the beam waist w_0 and its position z_0. For the vertical direction, the waist is 379 μm, located 142.4 mm behind the output port. For the horizontal direction, the waist is 406 μm, positioned at 75.5 mm behind the output port of the laser. Therefore, the beam features a minor ellipticity (different waist size in the two directions) and astigmatism (different waist position in the two directions) but still within the specification from the laser datasheet. In fact, the ellipticity of approximately 1.1 observed from figure 5.10 is the upper limit mentioned in the datasheet.
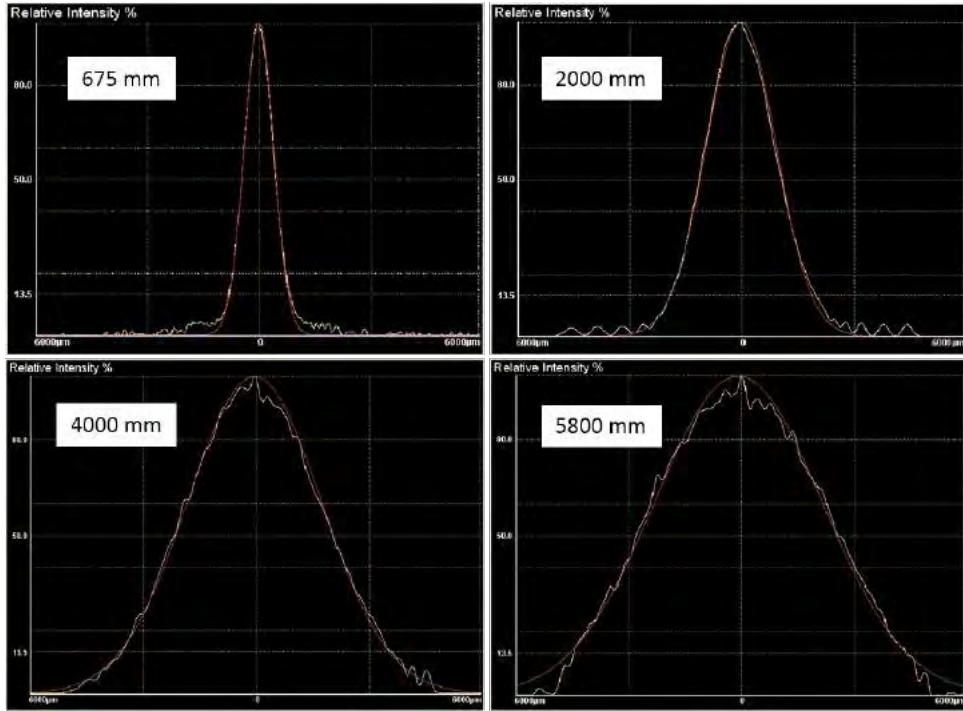
48

Figure 5.9: Vertical axis intensity profile of the laser output beam for some selected distances. Yellow line is the measured intensity while the red line is the Gaussian fit to the measured profile.
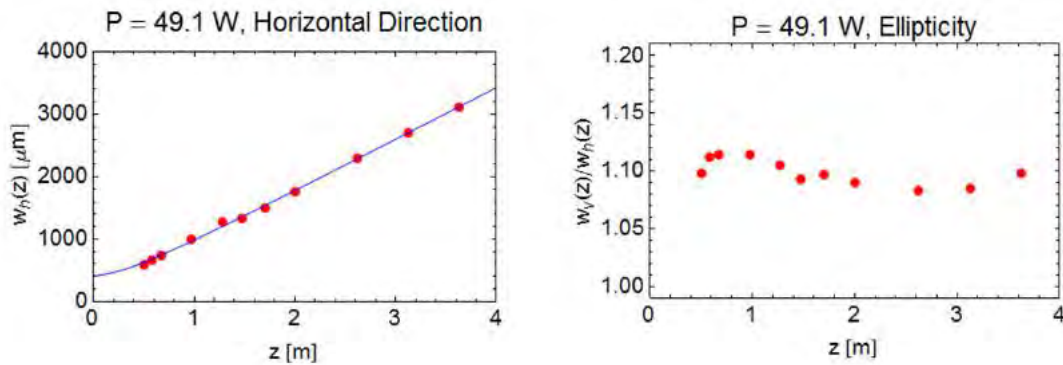

Figure 5.10: Laser output beam spot size in function of position from the laser output port, for the laser power of 49.1 W. Red dots indicate the data points, while the blue line is the fit to the Gaussian beam propagation function (equation 5.2.1).

Collimated Beam Profile Measurement

The beam shaping scheme requires the input beam waist at the SLM plane. Experimentally, this condition is never perfectly achievable and instead, we aim to produce a collimated beam as the input. Practically, a collimated beam is a Gaussian beam with a large waist of the order of 1 mm. For a beam with such waist, the Rayleigh length of the beam is of the order of several meters. Therefore, we would observe that the beam size is nearly constant within several hundreds of milimeters, the typical distances in an optical alignment. This point of view explains the classical optics picture, where a collimated beam is pictured as beam propagating with a constant spot size.

As we understand from the classical optics, a collimated beam is produced by placing a lens

at a distance equals to its focal length away from the source. In our case, the source location is the position of the waist of the output beam which is of the order of 100 mm behind the output port. The space constraints due to various optical elements controlling the beam power leads to our decision to place a 1000 mm lens around 900 mm in front of the output port to collimate the beam (refer to figure 5.6).

Referring to figure 5.11, we first remark that the beam is reasonably well-collimated, shown by the width of the beam which doubles approximately after 5-6 m of propagation. We also report an anomalous propagation profile of this collimated beam. In this horizontal intensity profile, we first observed a gaussian beam at a distance close to the lens with a fringe pattern in the wings. With an infrared card, we affirm that the Gaussian peak of the beam is surrounded by several bright rings. As the beam propagates, the profile starts to firstly show destructive around the central peak that later evolves into two minimas surrounding the central peak. The similar evolution is also observed in the vertical intensity profile of the beam. From this observation, we hypothesize that the strange beam profile results from a substantial interference between the bright ring pattern and the main Gaussian beam.
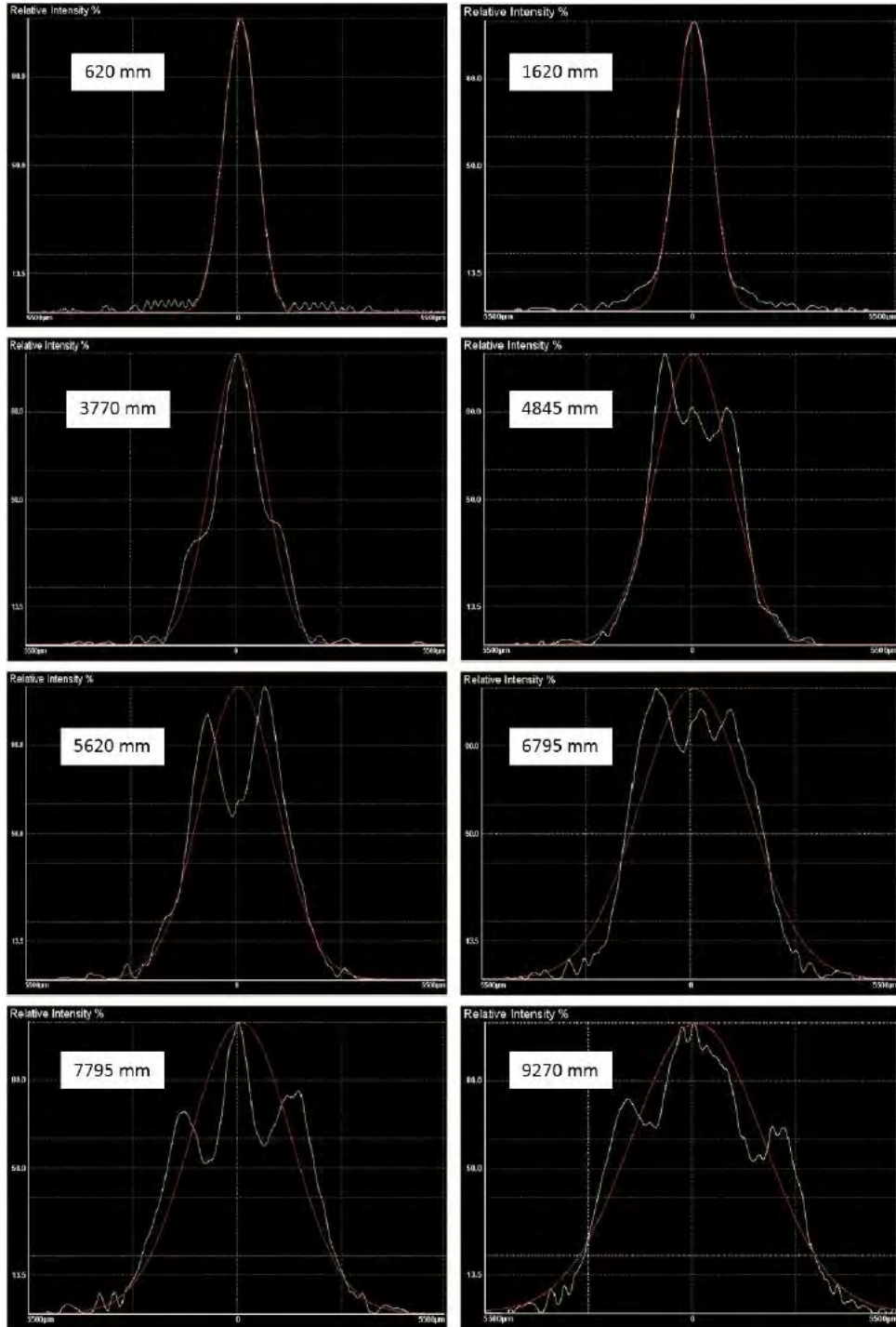
Figure 5.11: Horizontal axis intensity profile of the collimated beam for some selected distances. Yellow line is the measured intensity while the red line is the gaussian fit to the measured profile.

Collimated Beam Filtered with an Iris Profile Measurement

To test this hypothesis, we aim to block the ring pattern before the lens to prevent it from interfering with the main beam. Thus, we install an iris before the lens to block the ring pattern outside the main beam. To align the iris, we remove the collimating lens, and we detect the beam profile just after the iris with the Beam Master (figure 5.12). With the high resolution profile, we adjust the opening size of the iris until the fringes pattern at the wing is covered (see figure 5.13). The fine positioning of the iris with respect to the beam is adjusted with the help of the last mirror before the iris. We measure that the power blocked by the iris is
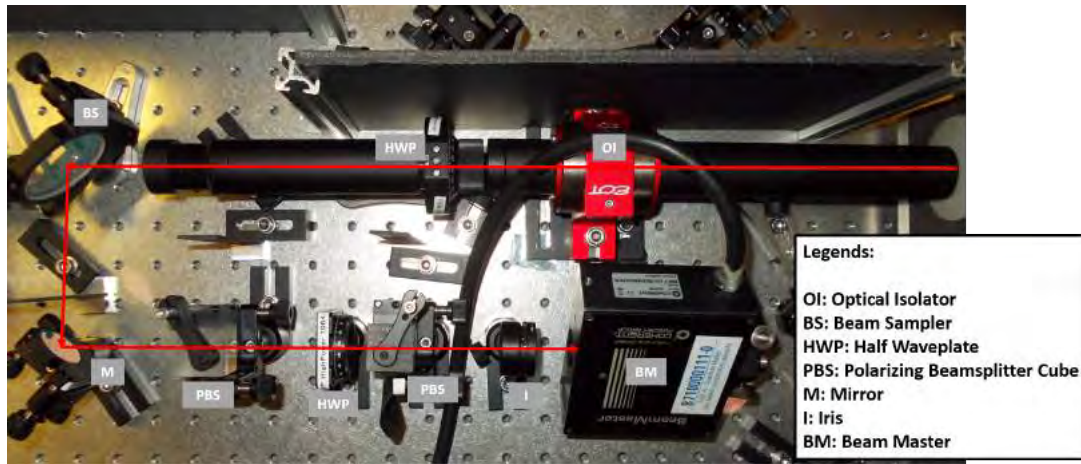
Figure 5.12: Experimental setup for the placement of the iris. The red line indicates the beam propagation path from the laser output port.

approximately 10% of the total beam power. This fact supports our hypothesis that the ring pattern can indeed cause a considerable interference effect, since it contains a fair amount of power.
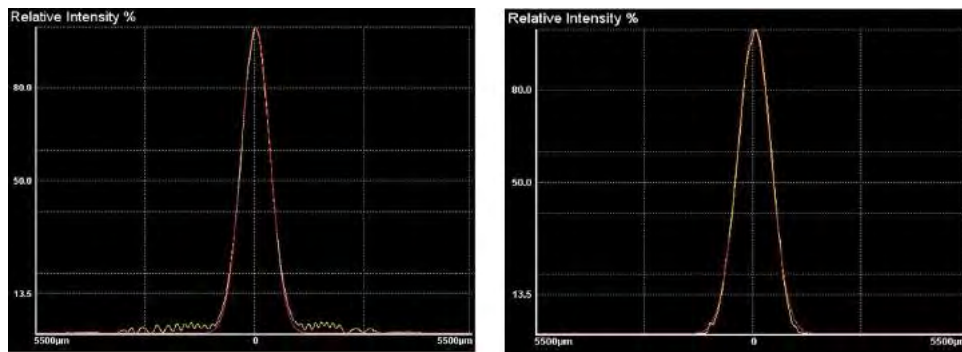

Figure 5.13: Comparison of the horizontal axis intensity profile with (Right) and without (Left) the iris.

With the iris filtering the unwanted ring pattern, we reinstall the collimating lens at its original positon and remeasure the beam profile. The profile for both the horizontal (figure 5.14) and vertical (figure 5.15) axis intensity are relatively good gaussian profiles. We repeat once again the measurement and gaussian beam fit in function of position, this time taking the position of the lens as the origin. In figure 5.21, we display the horizontal beam spot size and the beam ellipticiy in function of position for this collimated and filtered beam. Fitting the beam propagation to the Gaussian beam propagation, we obtain the vertical beam waist of 919 μm, 116 mm in front of the lens whereas for the horizontal axis, the beam waist is 837 μm, 248 mm in front of the lens. The Rayleigh length for this values of beam waist is around 2 m.
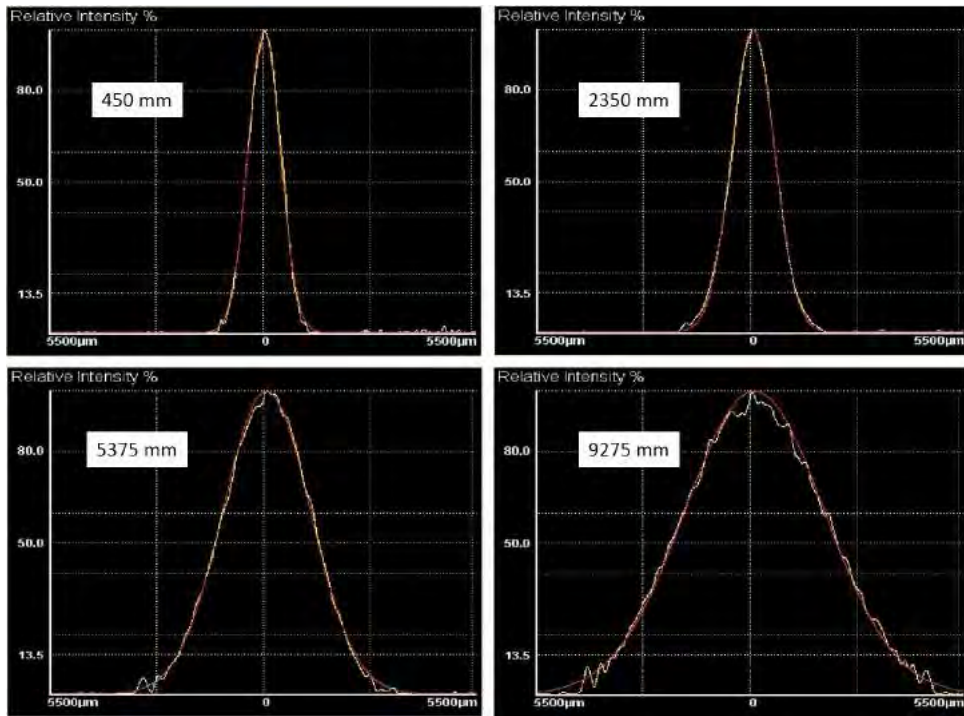
Figure 5.14: Horizontal axis intensity profile of the collimated, filtered beam for some selected distances. Yellow line is the measured intensity while the red line is the Gaussian fit to the measured profile.
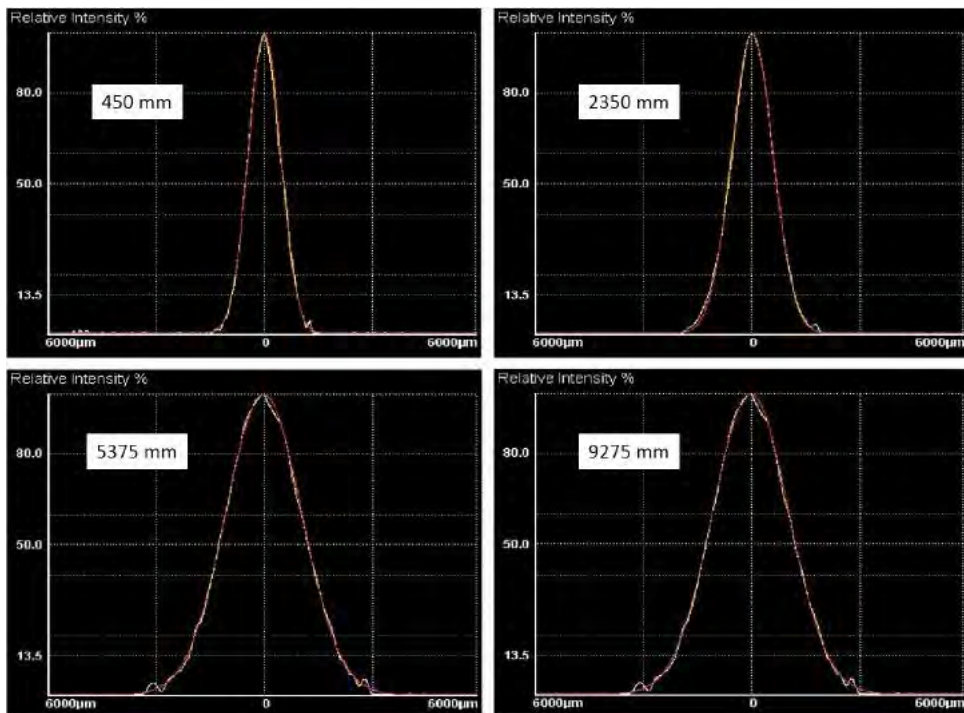

Figure 5.15: Vertical axis intensity profile of the collimated, filtered beam for some selected distances. Yellow line is the measured intensity while the red line is the Gaussian fit to the measured profile.
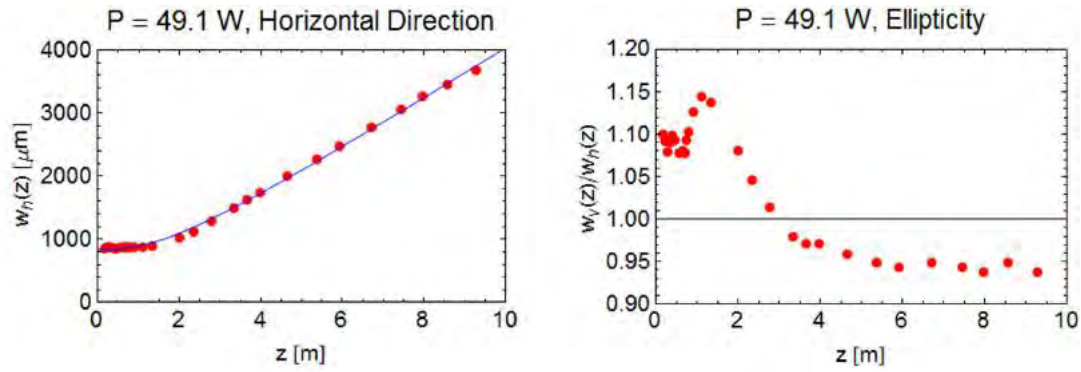
Figure 5.16: Collimated, filtered beam spot size in function of position from the laser output port. Red dots indicate the data points, while the blue line is the fit to the Gaussian beam propagation function (equation 5.2.1).

5.3 First Experimental Results of the Flat-Top Beam Shaping

In this section, we will describe our current results in the attempt of producing the flat-top beam with the DLP3000 mirror chip and the Error Diffusion algorithm. We start by describing our SLM and the relay telescope setup, focusing on the necessary alignment methods. Finally, we end this section by presenting our current flat-top beam result.

SLM Description and Testings

The DLP3000 mirror chip which we use as our SLM is packaged as an evaluation module called the 'DLP Lightcrafter' [52]. The module is a mini projector device, consists of three colors LED, the DLP3000 mirror chip with its electronic circuit board, and the projector lens. Since we only need the mirror chip, the chip and its electronic board is transferred from the module to a house-made box which also facilitates the mounting process of the DLP chip. The chip is operated with a 5 V DC power source and the state of the mirrors is addressed with a provided control software.
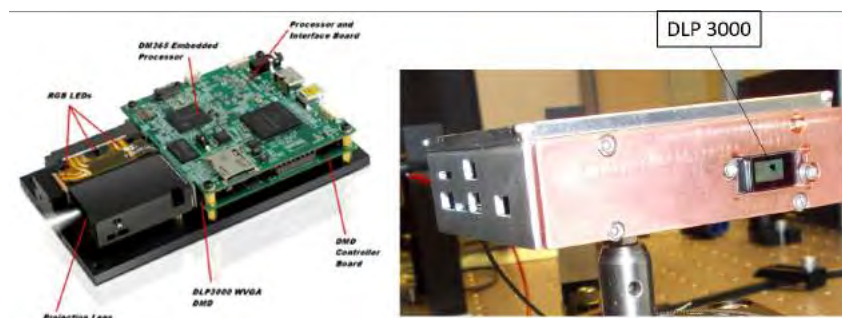

Figure 5.17: (Left) The DLP Lightcrafter module and (Right) the extracted DLP3000 with the electronic control board housed in the metal box.

We begin our tests with the working characteristics of the DLP3000 chip. Firstly, we check the specified tilting states of the mirror arrays. The datasheet specifies three possible tilting states of the mirror array: a tilt by $+12^0$ and -12^0, which are assignable to any individual mirror and a flat state where the mirror array is parallel to the substrate of the chip. This flat state is only achieved globally when the chip is switched off, where all individual mirrors are set to this flat state. We set all the micromirrors into each of the three states, and we observe the

reflection of the collimated beam off the mirror chip. We found that each tilt state deflects the beam into three different directions as expected. However, we note that the main reflection is accompanied by numerous other reflection spots that are less bright but are still detectable by an infrared card or an infrared viewer. These stray reflections are present due to the pixelated structure of the chip which resembles a diffraction grating (which diffracts light into several orders).
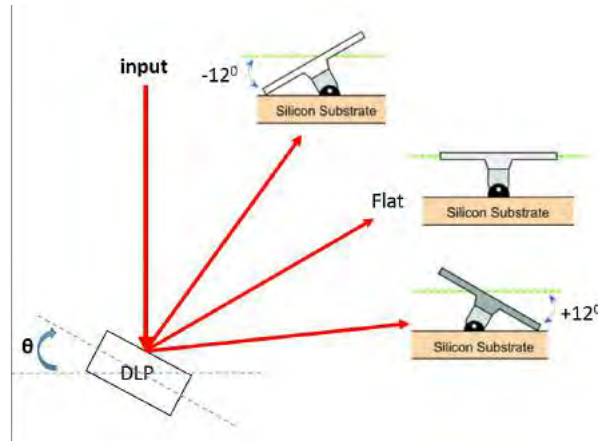

Figure 5.18: Schematic setup of the reflection off the DLP3000 chip for each of the three tilt states.

Subsequently, we aim to optimize the reflection factor of the DLP chip. This is especially important with a high power beam because the unreflected portion of the incoming light is converted into heat which can damage the device. The datasheet-specified damage threshold of the DLP3000 chip for a 1064 nm input beam is 10 mW, and thus we set the input power at 3 mW to be conservative. We discovered that the reflectivity of the chip is very angle-sensitive along the horizontal tilt plane, which is also the tilting plane of the mirrors. we also found that this is not the case for the vertical tilt plane. Therefore, we mount the DLP3000 chip on top of a 2" mirror mount that provides a fine-tuning of the horizontal tilt angle and a rotation platform which provides the coarse angle tuning. We record the optimum reflected power for several values of the chip rotation angle θ (refer to figure 5.18) and for the case where all the mirrors are set to either one of the two active states ($\pm 12^0$). To find the angle which gives this optimum condition, we place a lens (of focal length f) at a $2f$ distance in front of the chip, followed by the power meter at another $2f$ distance after the lens (see figure 5.19). This 2f-2f arrangement minimizes the physical displacement of the beam at the power meter as we fine tune the reflection angle of the beam with the mirror mount.

From the result displayed in figure 5.20, the maximum reflectivity is obtained when the chip is tilted by 25-30 ^{0}, for the -12^0 tilt state. The reflectivity factor of $1.95/3 = 65\%$ matches the specification of the datasheet (refer to the description in the previous chapter). Therefore, we set the DLP chip at this optimum angle, and we define the -12^0 tilt as the 'On' state, the $+12^0$ tilt as the 'Off' state in the beam shaping scheme. We let through the main reflection beam from this -12^0 tilt state to the next optical elements, blocking the reflection from the $+12^0$ tilt state and other stray reflections.
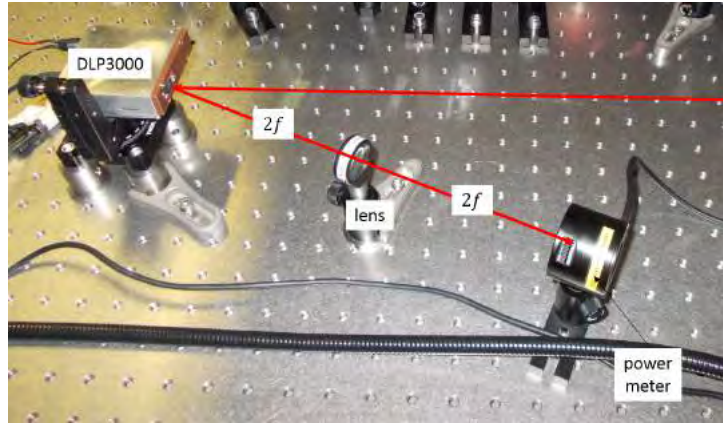
Figure 5.19: The 2f-2f configuration used in the measurement of the angle-dependence of the DLP3000 chip reflection factor.

Mount Angle (^{0})	Optimum Reflected Power (mW)	
	-12^0 State	$+12^0$ State
0	1.25	1.24
5	1.86	1.94
10	1.2	1.83
15	1.89	1.74
20	1.86	1.36
25	1.95	0.81
30	1.95	0.42
35	1.66	0.9
40	1.85	0.87

Figure 5.20: Measurement result of the angle-dependence of the DLP3000 chip reflection factor. Note that the input power is 3 mW.

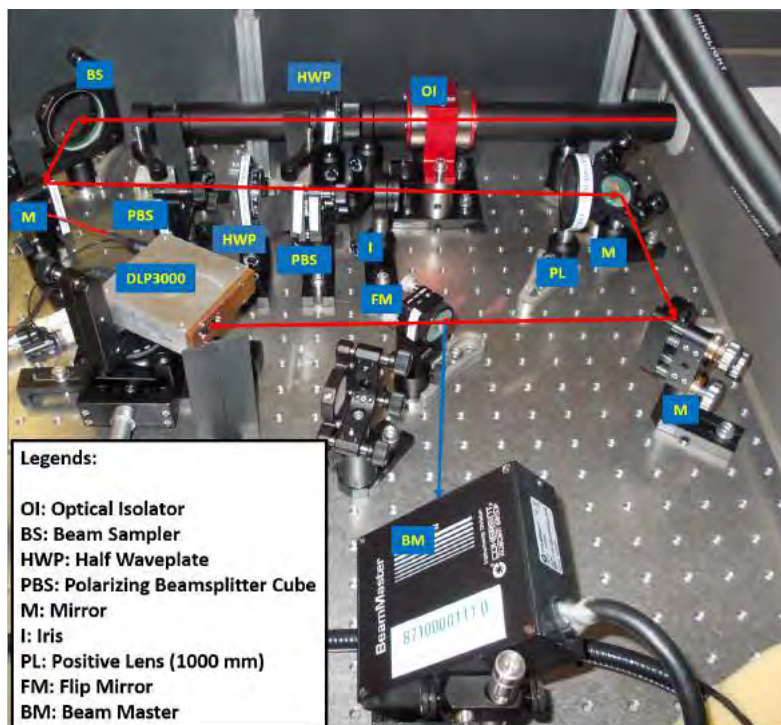## Measurement of the Beam Profile at the SLM plane

Figure 5.21: Experimental setup for the measurement of the beam profile at the SLM plane. The flip mirror deflects the collimated beam into the Beam Master (path shown in blue arrow). When the flip mirror is folded, the beam is sent directly to the DLP3000 chip (path shown in red arrow).

One requirement for the beam shaping algorithm is to know the profile of the input beam at the SLM plane. For this measurement, we insert a flip mirror before the DLP chip. When the mirror is installed, the collimated beam is deflected to the Beam Master which is placed at the same distance with respect to the flip mirror as the DLP chip. The measured profile shows that the beam spot size is 930 μm along the vertical direction and 850 μm along the horizontal direction. In addition, we mount the Beam Master on top of a translation stage which allows a displacement of approximately ± 1 cm in the direction of the propagation of the beam. Within this distance, we check that the variation of the beam spot size is negligible.

Telescope Alignment and Beam Shaping Result

At this stage, we are ready to proceed with the installation of a relay telescope after the DLP3000 for the beam shaping scheme. For this test setup, we use a pair of 300 mm and 200 mm lenses for a magnification for of 2/3. The longer focal length of the second lens is chosen to ease the alignment, as we aim to first demonstrate the experimental realization of the beam shaping and later modify the lens setting to rescale the flat-top beam as needed. We place the Beam Master 200 mm away from the telescope, approximately around the output plane of the telescope. The observed beam waist at this position has been shrunk from 930 μm to 620 μm for the vertical direction and 850 μm to 670 μm for the horizontal direction. The magnification factor is as expected for the vertical direction, and slightly too large for the horizontal direction. However, we deem that the deviation is not too significant, and we proceed with the next stage of the experiment.
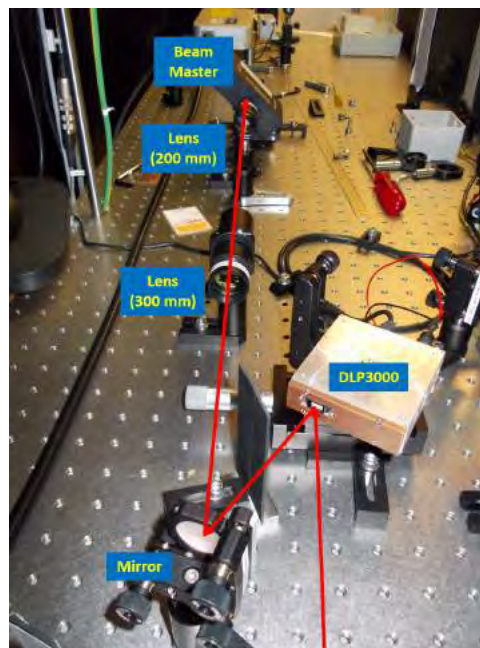

Figure 5.22: Relay telescope setup in front of the SLM.

One more alignment step to be done prior to loading the binary reflectance pattern that converts the Gaussian beam into the flat-top beam is to center the input gaussian beam on the DLP chip, which is an assumption in the calculation of the reflectance pattern. To do this, we load a 'hole pattern' to the DLP chip, where all the pixels are set to 'On' position, except a circular region at the center of the chip (refer to figure 5.23). We observe the intensity pattern with the Beam Master placed after the telescope, but the distance from the telescope is varied to measure the focused image position of the telescope. The beam transverse position at the DLP is adjusted differently for the vertical and horizontal direction. For the vertical direction, we move the beam with the last mirror before the DLP chip. However, for the horizontal direction,
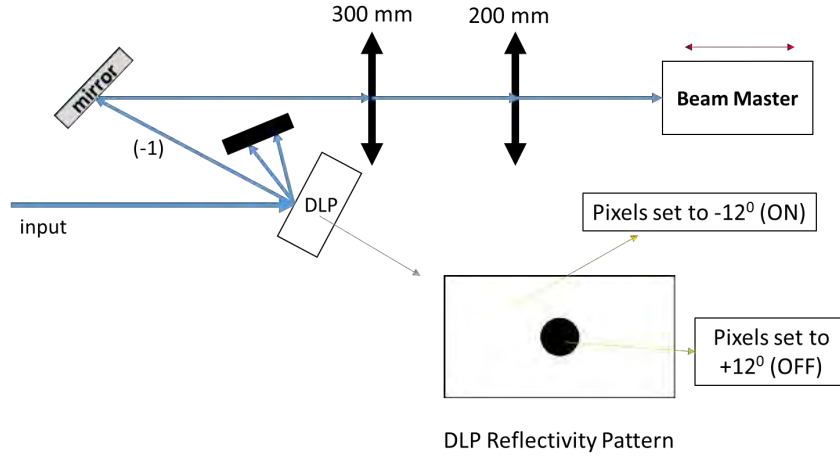
Figure 5.23: Setup for centering the beam at the DLP chip and the Beam Master at the output plane of the telescope.

we cannot do this since this will change the angle of incidence and therefore the reflectivity factor of the DLP chip. Instead, we move the chip along the horizontal direction by mounting it on top of a translation stage (refer to figure 5.22).

The hole pattern at the center of the SLM does not reflect the beam and will induce a dark spot in the measured beam profile. We move the beam position at the DLP plane such that the measured dark spot is found at the center of the beam. Furthermore, while moving the Beam Master position with respect to the telescope, we observe a change in contrast of the dark spot (figure 5.24). Indeed, the dip in the beam intensity at the center, due to this hole pattern initially increases as we move further from the telescope but later decreases after reaching the maximum contrast. We interpret the position where we found the biggest contrast from the hole pattern as the position where the image of the telescope is most focused. At this condition, the sensor is positioned between 220 mm to 245 mm from the telescope, which is only slightly different from what is predicted from the ideal case (200 mm).
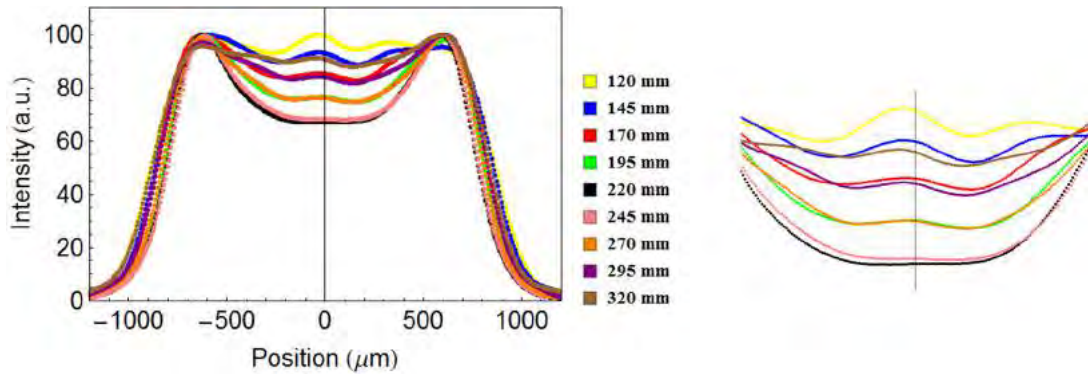

Figure 5.24: Vertical axis intensity profile of the collimated beam diffracted by the hole pattern and magnified by the relay telescope, in function of the detector position from the telescope. The profile is displayed on the left while the right image is a magnified view of the central region of the profile.

Finally, we present our first realization of the beam shaping scheme. We obtain the binary reflectance pattern with the Error Diffusion algorithm, converting the input beam of 930 μm by 850 μm waist to an order 20 Super Lorentz beam of 700 μm radius. We compare the observed

diffraction profile with this reflectivity pattern for two situations: the telescope setup without a spatial filter and the telescope setup with an iris placed approximately at the Fourier plane (300 mm from the first lens, and 200 mm behind the second lens). The iris is attached to a telescope mounting tube which is connected to the second lens such that it is well-centered on the beam. We empirically adjust the opening of the iris based on the observed beam profile. The comparison between the profiles in the two situations are displayed in figure 5.26 for the horizontal direction and in figure 5.25 for the vertical direction. As we can observe, the vertical axis profile does improve in the presence of the iris. The improvement is debatable for the horizontal axis profile, as the central region becomes slightly flatter but the profile falls less sharply around the wing, an indication that the profile is degraded into a lower order flat-top profile.
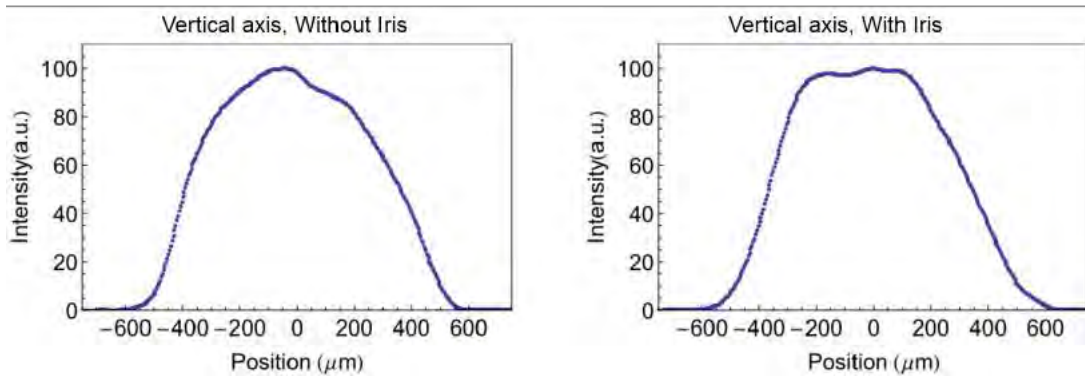

Figure 5.25: Comparison between the vertical axis flat-top beam profile produced by the setup with (Right) and without (Left) a spatial filter.
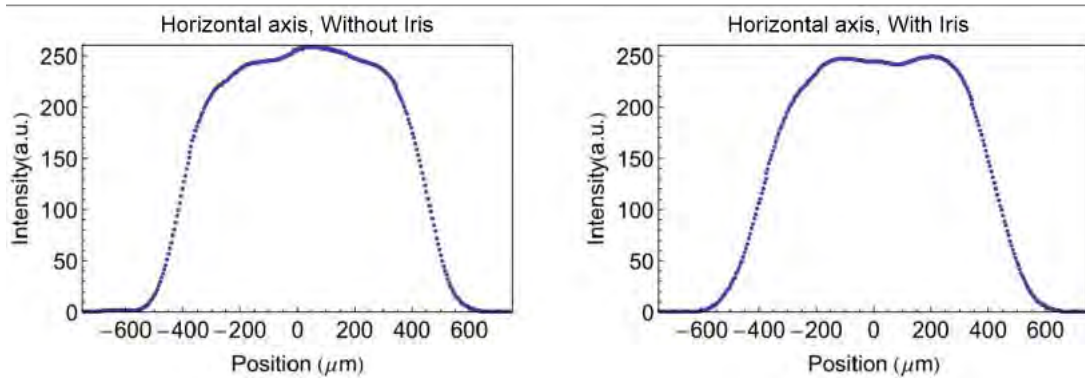

Figure 5.26: Comparison between the vertical axis flat-top beam profile produced by the setup with (Right) and without (Left) a spatial filter.

In figure 5.27, we show the plot of the intensity profile with the iris setup, with the fit to a Super Lorentz (SL) profile. We try the fitting process with the central position of the beam and its width as the fitting parameter, leaving the order of the SL function pre-determined. We found that the best fits that yield the lowest RMS error occur at a lower order as the target pattern. The horizontal profile is best fitted to an order 8 SL function whereas the vertical profile is best fitted with an order 6 SL function, down from the order 20 target profile. This degradation in the output beam order might also explain our finding that the shaping process works less well with a lower order beam target. We observed that using an order 8 SL function instead of 20, the output beam still very much resembles the initial Gaussian profile. We also find that the output pattern is less flat-top-like when a smaller radius target (600 μm and 650 μm) is used.
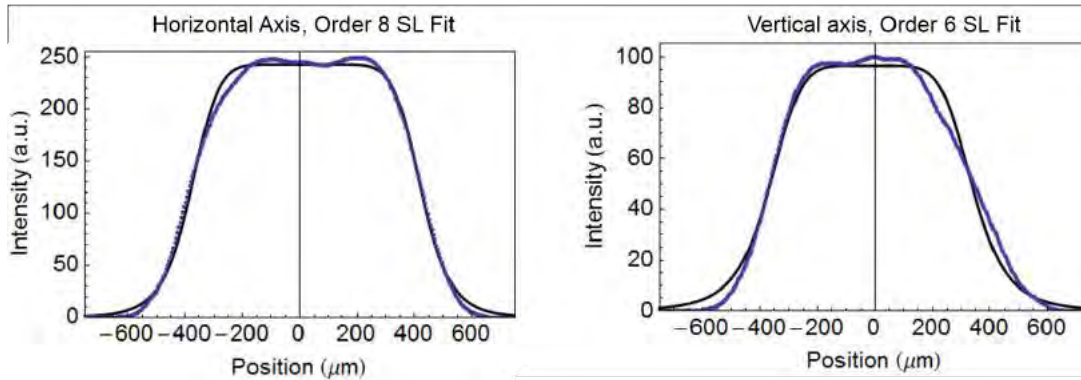
Figure 5.27: Comparison between the actual and fitted intensity profile of the flat-top beam produced with the telescope with iris setup. The blue dots are the measured profile while the black lines are the fitted profile.

5.4 Summary and Future Directions

To conclude this initial study, we have set the beam shaping scheme with a relay telescope imaging the reflection off the binary pattern initiated with the Error Diffusion algorithm. We admit that our current flat-top beam is not perfect, shown for example by the deviation from the fit and the observed degradation in the beam order. In addition, we would like to point out our initial observation of intensity fluctuations present in the output profile which is partially masked in the data we have presented due to an internal averaging process of the Beam Master device. A further study to characterize this noise would be our next step in the continuation of this project. Several measurements that can be tried out are, for example, observing the noise spectrum before and after the DLP3000 chip with a photodiode, and cross-checking the output beam profile by measuring it with a CCD camera instead of the Beam Master.

We would like to point at two future directions to take in order to further advance this study. Firstly, we could concentrate on developing a feedback process in order to ameliorate the output beam profile. Reference [44] described one such method, where the feedback process tries to search, isolate, then smoothen parts of beam for which the deviation from a flat-top profile is the largest. The algorithm locates the pixel correspondence of the part of the beam and randomly switch off (resp. on) a neighboring pixel if the beam intensity at this part is too high (resp. low). Afterward, we could characterize and improve the limit of the beam power which can be used with this scheme. A measurement of the maximum beam power that can be tolerated by the DLP3000 chip could be done by placing a temperature sensor in contact with a thermal monitoring point of the chip and recording its temperature as we increase the input beam power. The rise of temperature above the recommended operational condition would be a good indication for the limit of the input power. This measurement method carries the risk of permanently damaging the chip, and would preferably be done after all other measurements have been completed. If the input power threshold is too low for the trap application, we could replace the DLP3000 chip with a static chrome photomask described in chapter 4. In this manner, the DLP3000 chip serves as a test setup to design the mask pattern imprinted in the chrome photomask.

Appendix A

Fourier Optics

A.1 Beam Propagation Equation

In this chapter, we summarize some important results of the Fourier Optics treatment, which treats the propagation of a diffracted beam. Let us consider a monochromatic beam propagating in a particular direction, for example along the Z axis, and incident to an aperture Σ. Following Huygens-Fresnel principle, the electric field in a plane perpendicular to Z axis is a summation of many wavelets emitted from every point of the aperture (refer to figure A.1). Adopting a paraxial approximation, the electric field at a point on a plane located at distance z away from the aperture is given by: [32]

$$E(x,y,z) = \frac{e^{ikz}}{i\lambda z} e^{\frac{ik}{2z}(x^2+y^2)} \int\int_{\Sigma} \left(E(\xi,\eta,0) e^{\frac{ik}{2z}(\xi^2+\eta^2)} \right) e^{\frac{2\pi i}{\lambda z}(x\xi+y\eta)} d\xi d\eta, \qquad (A.1.1)$$

where $k = 2\pi/\lambda$ is the wavenumber and λ the beam wavelength. Notice the linearity of the structure of equation A.1.1 above. Writing the integration as an operator: $E(z) = \mathcal{P}_z(E(0))$, we can easily prove that $E(z1 + z2) = \mathcal{P}_{z2} \cdot \mathcal{P}_{z1}(E(0))$. This property validates the fact that the equation A.1.1 can be interpreted as the propagation equation: it describes the field at a distance z away from a source by a Fourier Transform integral of the field at the plane of the source.
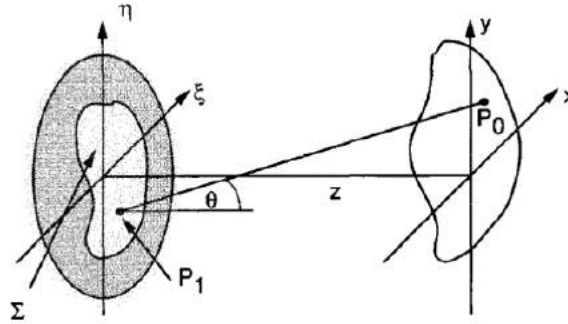

Figure A.1: Huygens principle of diffraction. Figure is taken from [32]

A.2 The Effect of a Thin Spherical Lens

A lens is an optical component that is used a lot in the beam shaping schemes we have considered in this report. It is therefore important to consider how a lens alters the propagation of a beam. Let us consider a lens which has a position-dependent thickness $\Delta(x,y)$. A lens consists of two spherical faces (with radius of curvature R_1 and R_2 respectively) separated by a certain thickness Δ_0. Let us consider the thickness of the lens at position (x,y) from the center as

shown in the right side of figure A.2. The thickness due to the left part of the curved side is given by:

$$d_1 = \Delta_{01} \left(R_1 - \sqrt{R_1^2 - x^2 - y^2} \right) \approx \Delta_{01} - \frac{1}{2R_1}(x^2 + y^2), \tag{A.2.1}$$

where Δ_{01} is the central thickness of this curved face. Here, we have used a paraxial approximation assuming that the size of the lens is small compared to its curvature (x,y R_1). The total thickness of the lens will include a thickness d_2 between the two curved face and the thickness $d_3 \approx \Delta_{03} - \frac{1}{2R_2^2}(x^2 + y^2)$ of the second curved face. Thus, the total thickness of the lens is given by:

$$d(x,y) = d1 + d2 + d3 = \Delta_0 - \left(\frac{1}{2R_1} + \frac{1}{2R_2} \right)(x^2 + y^2). \tag{A.2.2}$$

We remark that in this equation, the radius of curvatures are defined to be positive when the face is convex, and negative when it is concave. Therefore, we see that a double convex lens is thickest in the middle, as opposed to a double concave lens which is thinnest in the middle.
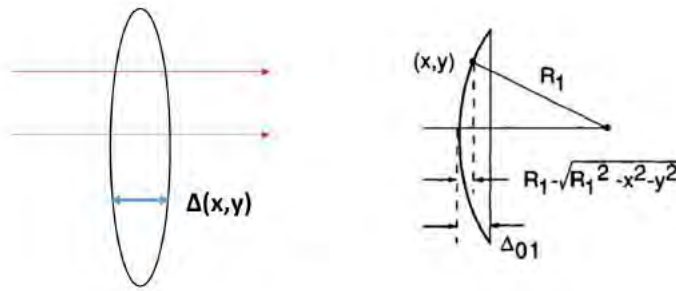

Figure A.2: The geometry of a spherical lens

As lenses are usually very thin, a beam is not appreaciably distorted as it passes through a lens. The most dominant effect is a phase shift due to the lens material. Suppose that the lens has an index of refraction equals to n. The phase shift acquired as the beam propagates through a material is equal to $\exp(ikl_o)$, where l_o is the optical length which is equal to the physical length multiplied by the index of refraction of the material. The optical length in function of position is:

$$l_o(x,y) = \underbrace{n \cdot d(x,y)}_{\text{lens}} + \underbrace{1 \cdot (\Delta_0 - d(x,y))}_{\text{air}} = n\Delta_0 - (n-1)(\frac{1}{2R_1} + \frac{1}{2R_2}(x^2+y^2) = n\Delta_0 - \frac{1}{2f}(x^2+y^2).$$
$$\tag{A.2.3}$$

The last line of the above equation uses the lens maker equation which relates the focal length f to the lens curvatures:

$$\frac{1}{f} = (n-1)\left(\frac{1}{R_1} + \frac{1}{R_2} \right) \tag{A.2.4}$$

As we can see, the effect of a lens, aside from a constant phase-shift due to its thickness is a quadratic phase shift term: $\exp\left(-\frac{ik}{2f}(x^2 + y^2) \right)$.

A.3 Special Optical Configurations

In this section, we will apply the propagation and lens equation we have derived to explain the imaging property of the two setups used in the manuscript: the Fourier imaging by a single positive lens and the relay telescope. For the first, we recall that the setup involves an input field pattern E_{in} which is placed at a distance f away behind a lens, and we observe the output profile at the plane f distance away behind the lens (refer to the right picture of figure A.3). Therefore, the output field is obtained by first propagating the input beam over a distance f,
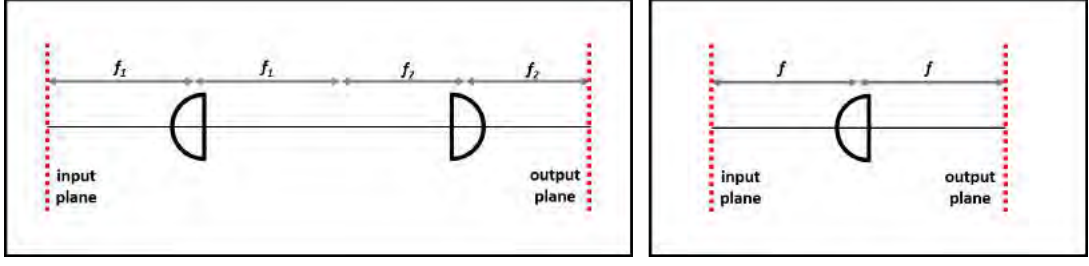
Figure A.3: Optical setup for (Left) a relay telescope and (Right) a single-lens Fourier imaging.

multiplying the field with the lens quadratic phase factor, and then propagating it over another f distance.

Let us perform the explicit calculation sequentially. The field at the plane just before the lens E_{bl} is the propagated input field E_{in} over a distance f:

$$E_{bl}(x,y) = \frac{e^{ikf}}{i\lambda f} e^{\frac{ik}{2f}(x^2+y^2)} \int \int \left(E_{in}(X,Y) e^{\frac{ik}{2f}(X^2+Y^2)} \right) e^{\frac{2\pi i}{\lambda f}(xX+yY)} dX dY. \qquad (A.3.1)$$

We notice that the quadratic phase factor $e^{-\frac{ik}{2f}(x^2+y^2)}$ of the lens exactly cancels out the quadratic phase term in the field E_{bl}. Hence the expression of the field at the plane just after the lens E_{al} is given by:

$$E_{al}(x,y) = \frac{e^{ikf}}{i\lambda f} \int \int \left(E_{in}(X,Y) e^{\frac{ik}{2f}(X^2+Y^2)} \right) e^{\frac{2\pi i}{\lambda f}(xX+yY)} dX dY. \qquad (A.3.2)$$

Finally, the output field profile E_{out} is obtained by propagating E_{al} over a distance f:

$$\begin{aligned}
E_{out}(x,y) &= \frac{e^{ikf}}{i\lambda f} e^{\frac{ik}{2f}(x^2+y^2)} \int \int \left(E_{al}(X,Y) e^{\frac{ik}{2f}(X^2+Y^2)} \right) e^{\frac{2\pi i}{\lambda f}(xX+yY)} dX dY \\
&= -\frac{e^{2ikf}}{(\lambda f)^2} e^{\frac{ik}{2f}(x^2+y^2)} \int \int \int \int E_{in}(\bar{x},\bar{y}) e^{\frac{ik}{2f}(\bar{x}^2+\bar{y}^2)} e^{\frac{ik}{2f}(X^2+Y^2)} e^{\frac{2\pi i}{\lambda f}(X\bar{x}+Y\bar{y})} \\
&\qquad\qquad\qquad e^{\frac{2\pi i}{\lambda f}(xX+yY)} dX dY d\bar{x} d\bar{y} \\
&= \frac{e^{2ikf}}{i\lambda f} \int \int E_{in}(\bar{x},\bar{y}) e^{\frac{2\pi i}{\lambda f}(\bar{x}x+\bar{y}y)} d\bar{x} d\bar{y}. \qquad (A.3.3)
\end{aligned}$$

Therefore, aside from a constant phase shift term e^{2ikf}, the output field is a Fourier Transform of the input field, hence the name of Fourier imaging in this case.

For the relay telescope, we notice that the setup can be broken down into two Fourier imaging setups with lens f_1 followed by f_2. The field at the Fourier plane of the first lens (i.e. a plane of distance f_1 behind the first lens, f_2 in front of the second lens) is given by the Fourier Transform of the input field E_{in}:

$$E_{FP} = \frac{e^{2ikf_1}}{i\lambda f_1} \int \int E_{in}(X,Y) e^{\frac{2\pi i}{\lambda f}(Xx+Yy)} dX dY, \qquad (A.3.4)$$

63

and the output field is given by the Fourier Transform of the field at the Fourier plane:

$$
\begin{aligned}
E_{out}(x, y) &= \frac{e^{2ikf_2}}{i\lambda f_2} \int\int E_{FP}(X, Y)\, e^{\frac{2\pi i}{\lambda f_2}(Xx+Yy)}\, dX dY \\
&= -\frac{e^{2ik(f_1+f_2)}}{\lambda^2 f_1 f_2} \int\int\int\int E_{in}(\bar{x}, \bar{y})\, e^{\frac{2\pi i}{\lambda f_2}(Xx+Yy)}\, e^{\frac{2\pi i}{\lambda f_1}(X\bar{x}+Y\bar{y})}\, dX dY d\bar{x} d\bar{y} \\
&= -\frac{e^{2ik(f_1+f_2)}}{\lambda^2 f_1 f_2} \int\int E_{in}(\bar{x}, \bar{y})\, \delta\left(\frac{x}{\lambda f_2} + \frac{\bar{x}}{\lambda f_1}\right) \delta\left(\frac{y}{\lambda f_2} + \frac{\bar{y}}{\lambda f_1}\right) d\bar{x} d\bar{y} \\
&= -\frac{f_1}{f_2} E_{in}\left(-\frac{f_1}{f_2}x, -\frac{f_1}{f_2}y\right).
\end{aligned}
\tag{A.3.5}
$$

Therefore, the output field of a relay telescope arrangement is proportional to the input field with a magnification factor of $-f_2/f_1$ which we recognize from the classical optics.

Appendix B

Gaussian Beam Properties

B.1 Gaussian Beam Propagation

In this section, we will give a brief introduction to the important properties of a TEM_{00} gaussian mode beam which is the idealized lasing mode of commercial lasers. The gaussian mode is one of the allowed solution of the Helmholtz equation, which governs the propagation of an electromagnetic wave in space. The field of a gaussian-mode beam propagating along the positive Z direction can be described as [53]:

$$E_g(x, y, z) = \left(\frac{2P}{\pi w(z)^2} \right)^{1/2} \exp \left(-\frac{x^2 + y^2}{w(z)^2} \right) \exp \left(-ik\frac{x^2 + y^2}{2R(z)} \right) e^{i\psi(z)} e^{ikz}. \qquad \text{(B.1.1)}$$
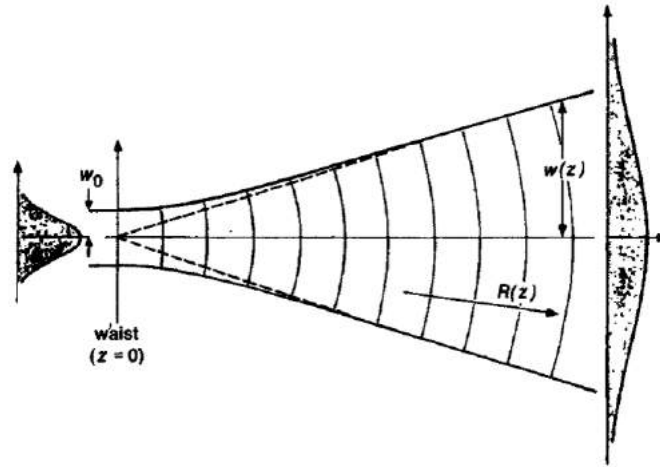

Figure B.1: Parameters in the propagation of a gaussian beam.

Notice that the field expression can be broken down into four components:

- **Amplitude distribution**

    In any plane perpendicular to the Z axis, the electric field amplitude follows a gaussian distribution: $\left(\frac{2P}{\pi w(z)^2} \right)^{1/2} \exp \left(-\frac{x^2 + y^2}{w(z)^2} \right)$, where P denotes the power of the beam. The equivalent radius of the beam is traditionally set as the distance where the amplitude falls to $1/e$ of the maximum amplitude (which is positioned at the center of the coordinate). As we can see, this distance is given by $w(z)$, which is called the spot size of the beam.

The spot size varies as the beam propagates in space, with its evolution given by:

$$w(z) = w_0 \sqrt{1 + \left(\frac{z}{z_R}\right)^2}, \tag{B.1.2}$$

where $z_R = \pi w_0^2/\lambda$ is known as the Rayleigh length of the beam, and w_0 is called the waist of the beam. The beam waist is in fact the smallest spot size of the beam, and it is positioned at $z = 0$ in this convention. As we follow the beam propagation starting from $z = -\infty$, the spot size first shrinked until it is equal to the waist, then reexpands. The Rayleigh length is the distance along z between the waist and the position where the spot size has grown to $\sqrt{2}w_0$. This range gives an estimation of a range for which the beam spot size is approximately constant (i.e. collimated beam in the classical optics point of view).
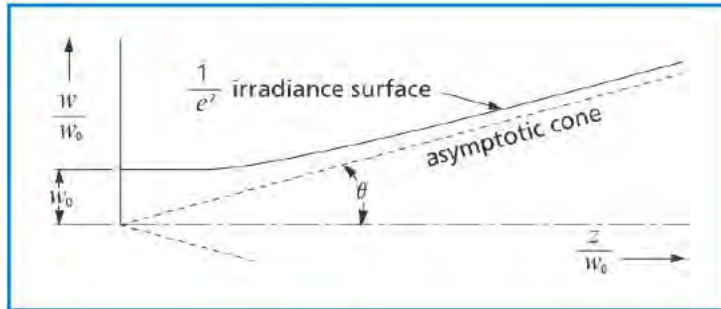

Figure B.2: Linear expansion of an uncollimated beam. Figure is taken from [54]

As we can observe from the expression of the Rayleigh length, a gaussian beam with a larger waist has a larger Rayleigh length, meaning that they stay collimated over a longer distance. In addition, when the beam is very far away from the waist ($z \gg z_R$), the spot size grows approximately linearly:

$$w(z) \approx \frac{\lambda \pi}{w_0} z. \tag{B.1.3}$$

In this condition, the beam is not collimated; it is either expanding or focusing as it propagates in space.

- **Spherical phase curvature**

The second part of the field is a phase factor with a spherical phase front: $\exp\left(-ik\frac{x^2+y^2}{2R(z)}\right)$. The radius of curvature of this phase term is:

$$R(z) = z + \frac{z_R^2}{z}. \tag{B.1.4}$$

We notice that the curvature at the plane of the beam waist ($z = 0$) is infinity, meaning that the phase front at this plane is flat. Otherwise, the spherical phase front is always curving outwards with respect to the plane of the waist (see figure B.1).

- **Gouy phase and propagation phase**

66

The last two terms are the extra phase shift called the Gouy phase: $e^{i\psi(z)}$ and a customary phase shift due to the propagation e^{ikz}. The Gouy phase shift is given by:

$$\psi(z) = \arctan(z/z_R) \tag{B.1.5}$$

A compact way of describing the gaussian beam is to utilize the complex beam parameter defined as:

$$q(z) := z + iz_R. \tag{B.1.6}$$

The field (ignoring the constant phase shift and the Gouy phase) can then be described in term of this single parameter:

$$E_g(x, y, z) = E_0 \exp\left(-\frac{ik(x^2 + y^2)}{2q(z)}\right) \tag{B.1.7}$$

B.2   Focusing through a Lens

Let us consider the setting where a gaussian beam is incident on a lens with a focal length f. If we let the position of the waist to be d_1 in front of the lens, we could calculate the output field at any position behind the lens by the Fourier Optics formulation considered in the appendix A. The resulting beam after the lens is still a gaussian mode, but with a change in the size of the waist and its position. Denoting the position of the waist of the focused beam as d_2 (with the convention of $d_2 = 0$ at the lens), this position is given an equation only slightly distinct from a classical lens equation [54]:

$$\frac{1}{d_1 + z_R^2/(d_1 - f)} + \frac{1}{d_2} = \frac{1}{f}, \tag{B.2.1}$$

and the waist of the focused beam w is given by:

$$w = \frac{w_0}{\sqrt{[1 - (d_1/f)]^2 + [z_R/f]^2}}. \tag{B.2.2}$$

In particular, in the Fourier imaging setup where $d_1 = f$, the resulting output beam is located exactly at the back-Fourier plane of the lens ($d_2 = f$) and the focused beam waist is given by:

$$w = \frac{\lambda f}{\pi w_0}. \tag{B.2.3}$$

Therefore, a larger input beam will be focused as a smaller beam, which is what we expect from the Fourier Transform relation.

Bibliography

[1] M. H. Anderson, J. R. Ensher, M. R. Matthews, C. E. Wieman, and E. A. Cornell, *Science* 269, 198 (1995).

[2] K. B. Davis, M.-O. Mewes, M. R. Andrews, N. J. van Druten, D. S. Durfree, D. M. Kurn, and W. Ketterle, *Phys. Rev. Lett.* 75, 3969 (1995).

[3] B. DeMarco and D. S. Jin, *Science* 285, 1703 (1999).

[4] I. Bloch, J. Dalibard, and S. Nascimbene, *Nature Phys.* 8, 267 (2012).

[5] G. Pupillo, A. Micheli, H. P. Büchler, and P. Zoller, (2008), arXiv:0805.1896v1 [cond-mat.other].

[6] B. Yan, S. A. Moses, B. Gadway, J. P. Covey, K. R. A. Hazzard, A. M. Rey, D. S. Jin, and J. Ye, *Nature* 501, 521 (2013).

[7] D. S. Jin and J. Ye, *Physics Today* 64, 27 (2011).

[8] L. D. Carr, D. DeMille, R. V. Krems, and J. Ye, *New J. Phys.* 11, 055049 (2009).

[9] C. Chin, R. Grimm, P. S. Julienne, and E. Tiesinga, *Rev. Mod. Phys.* 82, 1225 (2010).

[10] J. F. S. Brachmann, *Towards ^6Li - ^4OK ground state molecules*, PhD thesis, Ludwig Maximilian University of Munich, 2012.

[11] S. Inouye, M. R. Andrews, J. Stenger, H.-J. Miesner, D. M. Stamper-Kurn, and W. Ketterle, *Phys. Rev. Lett.* 97, 120402 (2006).

[12] K. K. Ni, S. Ospelkaus, M. H. G. de Miranda, A. Pe'er, B. Neyenhuis, J. J. Zirbel, S. Kotochigova, P. S. Julienne, J. Ye, and D. S. Jin, *Science* 322, 231 (2008).

[13] M. Aymar and O. Dulieu, *J. Atmos. Sci.* 122, 204302 (2005).

[14] D. E. Pritchard, *Phys. Rev. Lett.* 51, 1336 (1983).

[15] A. Ashkin, J. M. Dziedzic, J. E. Bjorkholm, and S. Chu, *Opt. Lett.* 11, 288 (1986).

[16] M. Grenier, O. Mandel, T. Esslinger, T. W. Hansch, and I. Bloch, *Nature* 415, 39 (2002).

[17] I. Bloch, *Nature Phys.* 1, 23 (2005).

[18] A. L. Gaunt, T. F. Schmidutz, I. Gotlibovych, R. P. Smith, and Z. Hadzibabic, *Phys. Rev. Lett.* 110, 200406 (2013).

[19] J. F. S. Brachmann, Inducing Vortices in a Bose-Einstein Condensate using light beams with orbital angular momentum, diploma thesis, Harvard University, 2007.

[20] D. Grewell and A. Benatar, *Opt. Eng.* 46, 118001 (2007).

[21] G. Grynberg, A. Aspect, and C. Fabre, *Introduction to Quantum Optics: From the Semiclassical Approach to Quantized Light*, Cambridge University Press, 2010.

[22] R. Grimm, M. Weidemuller, and Y. B. Ovchinnikov, *Adv. At. Mol. Opt. Phys.* 42, 95 (2000).

[23] S. Kotochigova and D. DeMille, *Phys. Rev. A* 82, 063421 (2010).

[24] P. S. Julienne, T. M. Hanna, and Z. Idziaszek, *Phys. Chem. Chem. Phys* 13, 19114 (2011).

[25] Z. Idziaszek and P. S. Julienne, *Phys. Rev. Lett.* 104, 113202 (2010).

[26] M. H. G. de Miranda, A. Chotia, B. Neyenhuis, D. Wang, G. Quéméner, S. Ospelkaus, J. L. Bohn, J. Ye, and D. S. Jin, *Nature Phys.* 7, 502 (2011).

[27] K. K. Ni, S. Ospelkaus, D. Wang, G. Quéméner, B. Neyenhuis, M. H. G. de Miranda, J. L. Bohn, J. Ye, and D. S. Jin, *Nature* 464, 1324 (2010).

[28] J. A. Neff, R. A. Athale, and S. H. Lee, *Proc. IEEE* 78, 826 (1990).

[29] XY Series Liquid Crystal SLM Data Sheet, Boulder Nonlinear Systems Inc., http://bnonlinear.com/wp-content/themes/Avada-Child-Theme/pdf/XYSeriesDS0909.pdf.

[30] Deformable Mirrors, Boston Micromachines Corp., http://www.bostonmicromachines.com/plus-kilo.htm.

[31] J. F. S. Brachmann, W. S. Bakr, J. Gillen, A. Peng, and M. Greiner, *Opt. Express* 19, 12984 (2011).

[32] J. W. Goodman, *Introduction to Fourier Optics*, McGraw-Hill Companies, Inc., second edition, 1996.

[33] M. Pasienski and B. DeMarco, *Opt. Express* 16, 2176 (2008).

[34] PLUTO Phase Only Spatial Light Modulator (Reflective), Holoeye Corp., http://holoeye.com/spatial-light-modulators/slm-pluto-phase-only.

[35] J. Liang, R. N. Kohn, Jr., M. F. Becker, and D. J. Heinzen, *Appl. Opt.* 48, 1955 (2009).

[36] Y. Li, *Opt Commun* 206, 225 (2002).

[37] A. L. Gaunt and Z. Hadzibabic, *Sci. Rep.* 2 (2012).

[38] Texas Instrument, *DLP 0.3 WVGA Series 220 DMD*, revised october 2012 edition.

[39] B. E. A. Saleh and M. C. Teich, *Fundamental of Photonics*, John Wiley and Sons, first edition, 1991.

[40] E. Hecht, *Optics*, Addison Wesley, fourth edition, 2002.

[41] R. W. Floyd and L. Steinberg, *J. Soc. Inf. Disp.* 17, 75 (1976).

[42] C. Dorrer and J. D. Zuegel, *J. Opt. Soc. Am. B.* 24, 1268 (2007).

[43] J. P. Campbell and L. G. DeShazer, *J. Opt. Soc. Am.* 59, 1427 (1969).

[44] J. Liang, R. N. Kohn, Jr., M. F. Becker, and D. J. Heinzen, *Appl. Opt.* 49, 1323 (2010).

[45] J. Liang, R. N. Kohn, Jr., M. F. Becker, and D. J. Heinzen, *J. Micro/Nanolith. MEMS MOEMS* 11, 023002 (2012).

[46] Coherent Inc. Mephisto MOPA, http://www.coherent.com/products/?2067/Mephisto-MOPA.

[47] Coherent Inc., *Mephisto-MOPA-Data-Sheet*.

[48] Thorlabs - S322C - Thermal Power Sensor, Surface Absorber, 0.25 - 11 Âţm, 200 W, Fan Cooled, http://www.thorlabs.hk/thorproduct.cfm?partnumber=S322C.

[49] EOT Inc. - Free Space 1045-1080nm High Power Rotators and Isolators, http://www.eotech.com/product/94/10451080nm/HighPower/.

[50] Coherent Inc. - BeamMaster USB Knife-Edge Based Beam Profilers, https://www.coherent.com/products/?271/BeamMaster-USB-Knife-Edge-Based-Beam-Profilers.

[51] Coherent Inc., *Beam Master PC - User Manual*, october 2011 edition.

[52] Texas Instument - DLP Lightcrafter, http://www.digikey.com/product-highlights/us/en/texas-instruments-dlp-technologies/688.

[53] A. E. Siegmann, *Lasers*, University Science Books, 1986.

[54] CVI Melles Griot Technical Guide - Chapter 2: Gaussian Beam Optics, http://www.physast.uga.edu/files/phys3330$_f$ $ertig/Gaussian - Beam - Optics.pdf$.